Algorithm Theoretical Baseline Document for Sentinel-5 Precursor Methane Retrieval

Otto Hasekamp, Alba Lorente, Haili Hu, Andre Butz, Joost

aan de Brugh, Jochen Landgraf

TROPOMI

sentinel-5p

Document approval record

	digital signature
prepared:	
checked:	Michael Buchwitz and Thomas Krings Institute of Environmental Physics (IUP) University Bremen, Germany
approved PM:	
approved PI:	

Document change record

issue	date	item	comments
0.00.01	2012-09-25	all	Darft ATBD
0.00.02	2012-11-08		Comments internal review addressed. Note on the dependence of computational performance on compiler included. For GNU compiler significantly more processors are needed (60-90) than earlier estimated for the Intel compiler (page 22).
0.00.02	2012-11-23	doc number	Changed to report (RP) with new doc number
0.05	2013-06-04	all	Several additions from draft to version 1: More extended algorithm description, extended sensitivity study, section on validation.
0.05	2013-06-20	contents + doc number	Addressed comments internal review, changed to new document numbering
0.09	2013-11-27	all	addressed reviewer comments
0.10.00	2014-04-11	all	Removed instrument section. Introduced cirrus filter based on SWIR band. Slightly modified test ensemble to represent more realistic AOT (more demanding than previous ensemble).
0.11.00	2014-07-23	all	added fluorescence, deconvolution of solar spectrum, updated input/output tables, checked fraction of clear pixels with RAL VIIRS processor
0.13.00	2015-08-31	table 5-3 and 6-1	Update for limited release to S5p Validation Team; Made consistent with actual product
0.14.00	2015-12-11	section 9	Improved quality of Fig 9-17
1.00	2016-02-05	all	V1.0 release; Adressed comments from internal review (all minor)
1.10	2019-02-01	Sec. 5.6	description of bias correction added
	2019-02-01	Sec. 6.3	Tab. 5 updated
	2019-02-01	Sec. 6.4	SZA data filter updated
	2019-02-01	Sec. 6.5	TBC specified
	2019-02-01	Sec. 9	added

Contents

List of Tables

List of Figures

1   Introduction

1.1   Identification

This document describes the algorithm for the retrieval of the column average dry air mixing ratio of methane, $X\mathrm{CH_4}$, from Sentinel-5 (S5) measurements in the Near Infra Red (NIR) and Short Wave Infra Red (SWIR) spectral range. The algorithm name is RemoTeC-S5 and it is one of the deliverables of the ESA project 'Sentinel-5 P level 2 processor development' [AD1].

1.2   Purpose and objectives

The purpose of the document is to describe the theoretical baseline of the algorithm that will be used to for the operational processing to retrieve the column average dry air mixing ratio of methane $X\mathrm{CH_4}$, from Sentinel-5 Precursor (S5-P) measurements, the input and ancillary data that is needed, and the output that will be generated. In addition, information about expected calculation times and the expected accuracy are provided.

1.3   Document overview

Chapter 4 describes the main characteristics of the TROPOMI instrument, which was launched in October 2017. Chapter 4 gives a brief introduction to satellite $X\mathrm{CH_4}$ retrieval. Chapter 5 provides the description of the baseline retrieval algorithm. In Chapter 6 the feasibility is discussed including the efficiency of the calculations. Chapter 7 gives a detailed error analysis, Chapter 8 discusses the validation possibilities and needs, and Chapter 9 gives some examples of TROPOMI $X\mathrm{CH_4}$ data. Finally, Chapter 10 concludes the document.

2 Applicable and reference documents

2.1 Applicable documents

[AD1] Sentinel-5P Level 2 Processor Development – Statement of Work.
source: ESA; **ref:** S5P-SWESA-GS-053; **date:** 2012.

[AD2] GMES Sentinels 4 and 5 mission requirements document.
source: ESA; **ref:** EOP-SMA/1507/JL-dr; **date:** 2011.

2.2 Standard documents

[SD1] Space Engineering – Software.
source: ESA; **ref:** ECSS-Q-ST-80C; **date:** 2009.

[SD2] Space Product Assurance – Software Product Assurance.
source: ESA; **ref:** ECSS-E-ST-40C; **date:** 2009.

[SD3] TROPOMI Instrument and Performance Overview.
source: KNMI; **ref:** S5P-KNMI-L2-0010-RP; **issue:** 0.10.0; **date:** 2014.

[SD4] Requirements for the Geophysical Validation of Sentinel-5 Precursor Products, draft version.
source: ESA; **ref:** S5P-RS-ESA-SY-164; **date:** 2014.

2.3 Reference documents

[RD1] Terms, definitions and abbreviations for TROPOMI L01b data processor.
source: KNMI; **ref:** S5P-KNMI-L01B-0004-LI; **date:** 2011.

[RD2] Terms and symbols in the TROPOMI algorithm team.
source: KNMI; **ref:** SN-TROPOMI-KNMI-049; **date:** 2012.

[RD3] S. Solomon, D. Qin, M. Manning *et al.* (editors) *IPCC, Climate Change 2007: The Physical Science Basis. Contribution of Working Group I to the Fourth Assessment Report of the Intergovernmental Panel on Climate Change* (Cambridge University Press, Cambridge, United Kingdom and New York, NY, USA, 2007).

[RD4] H. Bovensmann, J. P. Burrows, M. Buchwitz *et al.*; SCIAMACHY: Mission Objectives and Measurement Modes. *Journal of Atmospheric Sciences*; **56** (1999), 127.

[RD5] T. Yokota, H. Oguma, I. Morino *et al.*; Test measurements by a BBM of the nadir-looking SWIR FTS aboard GOSAT to monitor CO_2 column density from space. *In Passive Optical Remote Sensing of the Atmosphere and Clouds IV* (edited by S. C. Tsay, T. Yokota and M.-H. Ahn); volume 5652 of *Proceedings of the SPIE*; (pp. 182–188) (2004); doi:10.1117/12.578497.

[RD6] A. Kuze, H. Suto, M. Nakajima *et al.*; Thermal and near infrared sensor for carbon observation Fourier-transform spectrometer on the Greenhouse Gases Observing Satellite for greenhouse gases monitoring. *Appl. Opt.*; **48** (2009), 6716; doi:10.1364/AO.48.006716.

[RD7] J. F. Meirink, H. J. Eskes and A. P. H. Goede; Sensitivity analysis of methane emissions derived from SCIAMACHY observations through inverse modelling. *Atmos. Chem. Phys.*; **6** (2006), 1275.

[RD8] P. Bergamaschi, C. Frankenberg, J. F. Meirink *et al.*; Satellite chartography of atmospheric methane from SCIAMACHY on board ENVISAT: 2. Evaluation based on inverse model simulations. *J. Geophys. Res.*; **112** (2007), D02304; doi:10.1029/2006JD007268.

[RD9] A. Butz, O. P. Hasekamp, C. Frankenberg *et al.*; CH_4 retrievals from space-based solar backscatter measurements: Performance evaluation against simulated aerosol and cirrus loaded scenes. *J. Geophys. Res.*; **115** (2010), D24302; doi:10.1029/2010JD014514.

[RD10] I. Aben, O. Hasekamp and W. Hartmann; Uncertainties in the space-based measurements of CO_2 columns due to scattering in the Earth's atmosphere. *J. Quant. Spectrosc. Radiat. Transfer*; **104** (2007), 450; doi:10.1016/j.jqsrt.2006.09.013.

[RD11] A.M.S. Gloudemans, H. Schrijver, O.P. Hasekamp *et al.*; Error analysis for CO and CH_4 total column retrieval from SCIAMACHY 2.3μm spectra. *Atmos. Chem. Phys.*; **8** (2008), 3999.

[RD12] C Frankenberg, U. Platt and T. Wagner; Retrieval of CO from SCIAMACHY onboard ENVISAT: detection of strongly polluted areas and seasonal patterns in global CO abundances. *Atmos. Chem. Phys.*; **4** (2005), 8425.

[RD13] C. Frankenberg, P. Bergamaschi, A. Butz *et al.*; Tropical methane emissions: A revised view from SCIAMACHY onboard ENVISAT. *Geophys. Res. Lett.*; **35** (2008), 15811; doi:10.1029/2008GL034300.

[RD14] O. Schneising, M. Buchwitz, M. Reuter *et al.*; Long-term analysis of carbon dioxide and methane column-averaged mole fractions retrieved from SCIAMACHY. *Atmos. Chem. Phys.*; **11** (2011), 2863; doi:10.5194/acp-11-2863-2011.

[RD15] R. Parker, H. Boesch, A. Cogan *et al.*; Methane observations from the Greenhouse Gases Observing SATellite: Comparison to ground-based TCCON data and model calculations. *Geophys. Res. Lett.*; **38** (2011), L15807; doi:10.1029/2011GL047871.

[RD16] D. Schepers, S. Guerlet, A. Butz *et al.*; Methane retrievals from Greenhouse Gases Observing Satellite (GOSAT) shortwave infrared measurements: Performance comparison of proxy and physics retrieval algorithms. *J. Geophys. Res.*; **117** (2012), D10307; doi:10.1029/2012JD017549.

[RD17] H. BöSch, G. C. Toon, B. Sen *et al.*; Space-based near-infrared CO_2 measurements: Testing the Orbiting Carbon Observatory retrieval algorithm and validation concept using SCIAMACHY observations over Park Falls, Wisconsin. *J. Geophys. Res.*; **111** (2006), D23302; doi:10.1029/2006JD007080.

[RD18] B. J. Connor, H. Boesch, G. Toon *et al.*; Orbiting Carbon Observatory: Inverse method and prospective error analysis. *J. Geophys. Res.*; **113** (2008), D05305; doi:10.1029/2006JD008336.

[RD19] S. Oshchepkov, A. Bril and T. Yokota; PPDF-based method to account for atmospheric light scattering in observations of carbon dioxide from space. *J. Geophys. Res.*; **113** (2008), D23210; doi:10.1029/2008JD010061.

[RD20] A. Butz, O. P. Hasekamp, C. Frankenberg *et al.*; Retrievals of atmospheric CO_2 from simulated space-borne measurements of backscattered near-infrared sunlight: accounting for aerosol effects. *Appl. Opt.*; **48** (2009), 3322; doi:10.1364/AO.48.003322.

[RD21] A. Bril, S. Oshchepkov and T. Yokota; Retrieval of atmospheric methane from high spectral resolution satellite measurements: a correction for cirrus cloud effects. *Appl. Opt.*; **48** (2009), 2139; doi:10.1364/AO.48.002139.

[RD22] M. Reuter, M. Buchwitz, O. Schneising *et al.*; A method for improved SCIAMACHY CO_2 retrieval in the presence of optically thin clouds. *Atmos. Meas. Tech.*; **3** (2010), 209.

[RD23] A. Butz, S. Guerlet, O. Hasekamp *et al.*; Toward accurate CO_2 and CH_4 observations from GOSAT. *Geophys. Res. Lett.*; **38** (2011), doi:10.1029/2011GL047888.

[RD24] H. Boesch, D. Baker, B. Connor *et al.*; Global Characterization of CO2 Column Retrievals from Shortwave-Infrared Satellite Observations of the Orbiting Carbon Observatory-2 Mission. *Remote Sens. Envirom.*; **3** (2011), 270; doi:10.3390/rs3020270.

[RD25] Y. Yoshida, Y. Ota, N. Eguchi *et al.*; Retrieval algorithm for CO_2 and CH_4 column abundances from short-wavelength infrared spectral observations by the Greenhouse gases observing satellite. *Atmos. Meas. Tech.*; **4** (2011), 717; doi:10.5194/amt-4-717-2011.

[RD26] C. W. O'Dell, B. Connor, H. Bösch *et al.*; The ACOS CO_2 retrieval algorithm - Part 1: Description and validation against synthetic observations. *Atmos. Meas. Tech.*; **5** (2012), 99; doi:10.5194/amt-5-99-2012.

[RD27] O. P. Hasekamp and A. Butz; Efficient calculation of intensity and polarization spectra in vertically inhomogeneous scattering and absorbing atmospheres. *J. Geophys. Res.*; **113** (2008), D20309; doi:10.1029/2008JD010379.

[RD28] S. Guerlet, A. Butz, D. Schepers *et al.*; Impact of aerosol and thin cirrus on retrieving and validating XCO$_2$ from GOSAT shortwave infrared measurements. *J. Geophys. Res.*; **118** (2013), 4887; doi:10.1002/jgrd.50332.

[RD29] S. Guerlet, S. Basu, A. Butz *et al.*; Reduced carbon uptake during the 2010 Northern Hemisphere summer from GOSAT. *Geophys. Res. Lett.*; **40** (2013), 2378; doi:10.1002/grl.50402.

[RD30] J.P. Veefkind, I. Aben, K. McMullan *et al.*; TROPOMI on the ESA Sentinel-5 Precursor: A GMES mission for global observations of the atmospheric composition for climate, air quality and ozone layer applications. *Remote Sens. Envirom.*; **120** (2012), 70; doi:doi:10.1016/j.rse.2011.09.027.

[RD31] R. van Deelen, O. P. Hasekamp and J. Landgraf; Accurate modeling of spectral fine-structure in Earth radiance spectra measured with the Global Ozone Monitoring Experiment. *Appl. Opt.*; **46** (2007), 243; doi:10.1364/AO.46.000243.

[RD32] D. Wunch, G. C. Toon, P. O. Wennberg *et al.*; Calibration of the Total Carbon Column Observing Network using aircraft profile data. *Atmospheric Measurement Techniques*; (2010), 1351; doi:10.5194/amt-3-1351-2010.

[RD33] A. Jenouvrier, L. Daumont, L. Régalia-Jarlot *et al.*; Fourier transform measurements of water vapor line parameters in the 4200 6600 cm^{-1} region. *J. Quant. Spectrosc. Radiat. Transfer*; **105** (2007), 326; doi:10.1016/j.jqsrt.2006.11.007.

[RD34] L.S. Rothman, I.E. Gordon, A. Barbe *et al.*; The HITRAN 2008 molecular spectroscopic database. *J. Quant. Spectrosc. Radiat. Transfer*; **110** (2009), 533.

[RD35] R. A. Scheepmaker, C. Frankenberg, A. Galli *et al.*; Improved water vapour spectroscopy in the 4174–4300 cm^{-1} region and its impact on SCIAMACHY HDO/H$_2$O measurements. *Atmos. Meas. Tech.*; **6** (2013) (4), 879; doi:10.5194/amt-6-879-2013. URL `http://www.atmos-meas-tech.net/6/879/2013/`.

[RD36] H. Tran, C. Boulet and J.-M. Hartmann; Line mixing and collision-induced absorption by oxygen in the A band: Laboratory measurements, model, and tools for atmospheric spectra computations. *J. Geophys. Res.*; **111** (2006), D15210; doi:10.1029/2005JD006869.

[RD37] A. Bucholtz; Rayleigh-Scattering calculations for the terrestrial atmosphere. *Appl. Opt.*; **35** (1995), 2765.

[RD38] J. E. Hansen and L. D. Travis; Light scattering in planetary atmospheres. *Space Science Reviews*; **16** (1974), 527; doi:10.1007/BF00168069.

[RD39] M. I. Mishchenko, I. V. Geogdzhayev, B. Cairns *et al.*; Aerosol retrievals over the ocean by use of channels 1 and 2 AVHRR data: sensitivity analysis and preliminary results. *Appl. Opt.*; **38** (1999), 7325; doi:10.1364/AO.38.007325.

[RD40] P. Stier, J. Feichter, S. Kinne *et al.*; The aerosol-climate model ECHAM5-HAM. *Atmos. Chem. Phys.*; **5** (2005), 1125.

[RD41] O. Dubovik, A. Sinyuk, T. Lapyonok *et al.*; Application of spheroid models to account for aerosol particle nonsphericity in remote sensing of desert dust. *J. Geophys. Res.*; **111** (2006), D11208; doi:10.1029/2005JD006619.

[RD42] J. F. de Haan, P. B. Bosma and J. W. Hovenier; The adding method for multiple scattering calculations of polarized light. *Astron. and Astrophys.*; **183** (1987), 371.

[RD43] J. Landgraf, O.P. Hasekamp, M. Box *et al.*; A Linearized Radiative Transfer Model Using the Analytical Perturbation Approach. *J. Geophys. Res.*; **106** (2001), 27291.

[RD44] O. P. Hasekamp and J. Landgraf; Linearization of vector radiative transfer with respect to aerosol properties and its use in satellite remote sensing. *J. Geophys. Res.*; **110** (2005), D04203; doi:10.1029/2004JD005260.

[RD45] B. van Diedenhoven, O. P. Hasekamp and J. Landgraf; Efficient vector radiative transfer calculations in vertically inhomogeneous cloudy atmospheres. *Appl. Opt.*; **45** (2006), 5993; doi:10.1364/AO.45.005993.

[RD46] M. Duan, Q. Min and J. Li; A fast radiative transfer model for simulating high-resolution absorption bands. *J. Geophys. Res.*; **110** (2005) (D15); doi:10.1029/2004JD005590. D15201; URL `http://dx.doi.org/10.1029/2004JD005590`.

[RD47] C. Frankenberg, C. O'Dell, L. Guanter *et al.*; Remote sensing of near-infrared chlorophyll fluorescence from space in scattering atmospheres: implications for its retrieval and interferences with atmospheric CO_2 retrievals. *Atmos. Meas. Tech.*; **5** (2012), 2081; doi:10.5194/amt-5-2081-2012.

[RD48] P.L. Phillips; A technique for the numerical solution of certain integral equations of the first kind. *J. Ass. Comput. Mat.*; **9** (1962), 84.

[RD49] A.N. Tikhonov; On the solution of incorrectly stated problems and a method of regularization. *Dokl. Acad. Nauk SSSR*; **151** (1963), 501.

[RD50] P. C. Hansen; *Rank-deficient and discrete ill-posed problems* (SIAM, Philadephia, 1998).

[RD51] C. D. Rodgers and B. J. Connor; Intercomparison of remote sounding instruments. *Journal of Geophysical Research (Atmospheres)*; **108** (2003), 4116; doi:10.1029/2002JD002299.

[RD52] C.D. Rodgers; *Inverse Methods for Atmospheres: Theory and Practice*; volume 2 (World Scientific, 2000).

[RD53] S5P-NPP Cloud Processor ATBD, issue 0.13.0.
source: RAL; **ref:** S5P-NPPC-RAL-ATBD-0001; **date:** 2015.

[RD54] Algorithm Theoretical Baseline Document for Sentinel-5 Precursor: Carbon Monoxide Total Column Retrieval.
source: SRON; **ref:** SRON-S5P-LEV2-RP-002; **date:** 2016.

[RD55] B. van Diedenhoven, O. P. Hasekamp and I. Aben; Surface pressure retrieval from SCIAMACHY measurements in the O_2 A Band: validation of the measurements and sensitivity on aerosols. *Atmos. Chem. Phys.*; **5** (2005), 2109.

[RD56] ATBD for S5P inter channel co-registration.
source: SRON; **ref:** SRON-S5P-LEV2-TN-018; **date:** 2014.

[RD57] M. Inoue, I. Morino, O. Uchino *et al.*; Bias corrections of GOSAT SWIR XCO_2 and XCH_4 with TCCON data and their evaluation using aircraft measurement data. *Atmospheric Measurement Techniques*; **9** (2016), 3491; doi:10.5194/amt-9-3491-2016.

[RD58] L. Wu, O. Hasekamp, H. Hu *et al.*; Carbon dioxide retrieval from OCO-2 satellite observations using the RemoTeC algorithm and validation with TCCON measurements. *Atmospheric Measurement Techniques*; **11** (2018), 3111; doi:10.5194/amt-11-3111-2018.

[RD59] ESA Climate Change Initiative (CCI): Product User Guide (PUG) for the RemoTeC XCH4 PROXY GOSAT Data Product v2.3.8 for the Essential Climate Variable (ECV) Greenhouse Gases (GHG).
source: SRON Netherlands Insitute for Space Research; **ref:** Version 4.1; **date:** 2016.

[RD60] M. Hess, R. B. A. Koelemeijer and P. Stammes; Scattering matrices of imperfect hexagonal ice crystals. *Journal of Quantitative Spectroscopy and Radiative Transfer*; **60** (1998), 301 ; doi:DOI: 10.1016/S0022-4073(98)00007-7.

[RD61] A. Galli, A. Butz, R. A. Scheepmaker *et al.*; CH_4, CO, and H_2O spectroscopy for the Sentinel-5 Precursor mission: an assessment with the Total Carbon Column Observing Network measurements. *Atmos. Meas. Tech.*; **5** (2012), 1387; doi:10.5194/amt-5-1387-2012.

[RD62] A. Butz, A Galli, O.P. Hasekamp *et al.*; ROPOMI aboard Sentinel-5 Precursor: Prospective performance of CH4 retrievals for aerosol and cirrus loaded atmospheres. *Remote Sens. Envirom.*; **120** (2012), 267.

[RD63] GMES Sentinel-5 Precursor – S5p System Requirement Document.
source: ESA; **ref:** S5p-RS-ESA-SY-0002; **date:** 2011.

[RD64] D Wunch, G. C Toon, J.-F. L Blavier *et al.*; The Total Carbon Column Observing Network. *Philos. T. R. Soc. A.*; **369** (2011) (1943), 2087; doi:10.1098/rsta.2010.0240.

[RD65] M. Reuter, H. Bösch, H. Bovensmann *et al.*; A joint effort to deliver satellite retrieved atmospheric CO_2 concentrations for surface flux inversions: the ensemble median algorithm EMMA. *Atmos. Chem. Phys.*; **13** (2013), 1771; doi:10.5194/acp-13-1771-2013.

[RD66] C. Petri, T. Warneke, N. Jones *et al.*; Remote sensing of CO_2 and CH_4 using solar absorption spectrometry with a low resolution spectrometer. *Atmos. Meas. Tech.*; **5** (2012), 1627; doi:10.5194/amt-5-1627-2012.

[RD67] M. Gisi, F. Hase, S. Dohe *et al.*; XCO_2-measurements with a tabletop FTS using solar absorption spectroscopy. *Atmos. Meas. Tech.*; **5** (2012), 2969; doi:10.5194/amt-5-2969-2012.

[RD68] A. Karion, C. Sweenney, P. Tans *et al.*; AirCore: An Innovative Atmospheric Sampling System. *J. Atm. Ocean Tech.*; **27** (2010), 1839; doi:doi:10.1175/2010JTECHA1448.1.

[RD69] H. Hu, J. Landgraf, R. Demeters *et al.*; Toward Global Mapping of Methane With TROPOMI: First Results and Intersatellite Comparison to GOSAT. *Geophys. Res. Lett.*; **45** (2018), 3682; doi:10.1002/2018GL077259.

[RD70] S5P Mission Performance Centre Methane [L2__CH4___] Readme.
source: ; **ref:** Version 1.02.02, S5P-MPC-SRON-PRF-CH4; **date:** 2019.

[RD71] O.P. Hasekamp and J. Landgraf; A linearized vector radiative transfer model for atmospheric trace gas retrieval. *J. Quant. Spectrosc. Radiat. Transfer*; **75** (2002).

[RD72] M. Hess and M. Wiegner; COP: a data library of optical properties of hexagonal ice crystals. *Appl. Opt.*; **33** (1994) (33), 7740; doi:10.1364/AO.33.007740.

[RD73] A. J. Heymsfield and C. M. R. Platt; A Parameterization of the Particle Size Spectrum of Ice Clouds in Terms of the Ambient Temperature and the Ice Water Content. *J. Atmos. Sci.*; **41** (1984), 846; doi:10.1175/1520-0469(1984)041<0846:APOTPS>2.0.CO;2.

[RD74] D. M. Winker, W. H. Hunt and M. J. McGill; Initial performance assessment of CALIOP. *Geophys. Res. Lett.*; **34** (2007), L19803; doi:10.1029/2007GL030135.

[RD75] H. Schrijver, A. M. S. Gloudemans, C. Frankenberg *et al.*; Water vapour total columns from SCIA-MACHY spectra in the 2.36 μm window. *Atmos. Meas. Tech.*; **2** (2009), 561.

[RD76] C. Popp, P. Wang, D. Brunner *et al.*; MERIS albedo climatology for FRESCO+ O_2 A-band cloud retrieval. *Atmospheric Measurement Techniques*; **4** (2011), 463; doi:10.5194/amt-4-463-2011.

2.4   Electronic references

There are no electronic references

3 Terms, definitions and abbreviated terms

Terms, definitions and abbreviated terms that are used in the development program for the TROPOMI L0 1b data processor are described in [RD1]. Terms, definitions and abbreviated terms that are used in development program for the TROPOMI L2 data processors are described in [RD2]. Terms, definitions and abbreviated terms that are specific for this document can be found below.

3.1 Acronyms and abbreviations

ECMWF	European Centre for Medium-Range Weather Forecasts
ENVISAT	Environmental Monitoring Satellite
GOSAT	Greenhouse gas Observing SATtellite
NASA	National Aeronautics and Space Administration
NOAA	National Oceanic and Atmospheric Administration
NPP	NPOESS Prepatory Project
NIR	Near Infra Red
OCO	Orbiting Carbon Observatory
SCIAMACHY	SCanning Imaging Absorption SpectroMeter for Atmospheric CHartographY
SWIR	Short Wave Infra Red
S5P	Sentinel-5 Precursor
TCCON	Total Carbon Column Observing Network
TROPOMI	Tropospheric Monitoring Instrument
UVN	Ultraviolet, Visible, Near-Infrared
VIIRS	Visible Infrared Imaging Radiometer Suite
XCH4	Column averaged dry air mixing ratio of methane

4 Introduction to methane retrieval algorithm

4.1 Background

Methane (CH_4) is, after carbon dioxide (CO_2), the most important contributor to the anthropogenically enhanced greenhouse effect [RD3]. Monitoring CH_4 abundances in the Earth's atmosphere is the dedicated goal of several current and future satellite missions. Such space borne observations aim at providing CH_4 column concentrations with high sensitivity at the Earth's surface, with good spatiotemporal coverage, and with sufficient accuracy to facilitate inverse modeling of sources and sinks. The Scanning Imaging Absorption Spectrometer for Atmospheric Chartography (SCIAMACHY) on board ENVISAT [RD4], that was operational 2002-2012, and the Greenhouse Gases Observing Satellite (GOSAT) [RD5], [RD6], launched 2009, have the capability to achieve these goals. Their observation strategy relies on measuring spectra of sunlight backscattered by the Earth's surface and atmosphere in the shortwave infrared (SWIR) spectral range. Absorption features of CH_4 allow for retrieval of its atmospheric concentration with high sensitivity to the ground and the lower atmosphere where the major CH_4 sources are located. The benefit of such measurements for estimating source/sink strengths, however, strongly depends on the precision and accuracy achieved. When correlated on the regional or seasonal scale, systematic biases of a few tenths of a percent can jeopardize the usefulness of satellite-measured CH_4 concentrations for source/sink estimates [RD7, RD8, RD9]. Scattering by aerosols and cirrus clouds is the major challenge for retrievals of methane from space-borne observations of backscattered sunlight in the SWIR spectral range. While contamination by optically thick clouds can be filtered out reliably, optically thin scatterers are much harder to detect yet still modify the light path of the observed backscattered sunlight and thus, can lead to underestimation or overestimation of the true methane column if not appropriately accounted for. The net light path effect strongly depends on the amount, the microphysical properties, and the height distribution of the scatterers as well as on the reflectance of the underlying ground surface [RD10, RD11]. Therefore, retrieval strategies rely on inferring the targeted gas concentration either simultaneously with scattering properties of the atmosphere or with a light path proxy. The latter 'proxy' approach has been successfully implemented for methane retrieval from SCIAMACHY measurements around 1600 nm, by using the CO_2 column, also retrieved from SCIAMACHY in the same spectral range, as a lightpath proxy [RD12]. The 'proxy' approach relies on the assumptions that scattering effects cancel in the ratio of the methane column and the CO_2 column and that a prior estimate of the CO_2 column is sufficiently accurate to reliably re-calculate the methane column from the ratio. By definition, the accuracy of the 'proxy' approach is contingent on the uncertainty of CO_2 column used for rescaling and on the cancellation of errors in the CH_4/CO_2 ratio. Further applications of the proxy approach for methane retrieval from SCIAMACHY are described by Frankenberg et al., 2018 [RD13] and Schneising et al., 2011 [RD14]. For GOSAT, the proxy approach has been successfully applied by Parker et al., 2011 [RD15] and Schepers et al., 2012 [RD16].

Alternatively, scattering induced lightpath modification can be taken into account by simultaneously inferring the atmospheric CH_4 concentration and physical scattering properties of the atmosphere. Such 'physics-based' methods have been developed for space-based CO_2 and/or CH_4 measurements from SCIAMACHY, GOSAT, and the Orbiting Carbon Observatory (OCO) (e.g. [RD17, RD18, RD19, RD20, RD21, RD22, RD23, RD24, RD25, RD26]). The physics based methods make use of the Oxygen A-band around 760 nm and absorption bands of the target absorber (CH_4 and/or CO_2) in the SWIR spectral range. The advantage of physics based methods for methane retrieval compared to a proxy method is that they do not depend on accurate prior information on the CO_2 column. On the other hand, the physics based algorithms are more complex and may be limited by the information content of the measurement with respect to aerosol properties and/or forward model errors in the description of aerosols. A detailed comparison between the two methods for GOSAT is provided by Schepers et al., 2012 [RD16].

4.2 The S5P spectral range

The spectral range measured by the S5P instrument [SD3] does not allow for a light-path-proxy approach, and thus the effect of aerosols and cirrus should be accounted for using a physics based method as mentioned above. The spectral ranges to be used are shown in Figure 1. The algorithm retrieves 3 aerosol parameters (amount, size, height) simultaneously with the methane column (and other parameters such as surface albedo) in order to account for light path modification by aerosols. The information on aerosol parameters comes from the parts of the spectrum with strong absorption lines (O_2 in the NIR band, CH_4 and H_2O in the SWIR band) of which the depth and shape is modified by aerosol scattering. The basis of the algorithm is to fit a forward model capable of handling (multiple) scattering by molecules and particles in the atmosphere, with the approximate parameterization of atmospheric scattering properties described above to the S5P NIR and SWIR

measurements. An important aspect of the algorithm is computational speed, since the S5P instrument will provide significantly more measurements than earlier instruments. For this purpose we developed a highly efficient radiative transfer model that avoids time consuming line-by-line calculations using a k-binning approach [RD27].
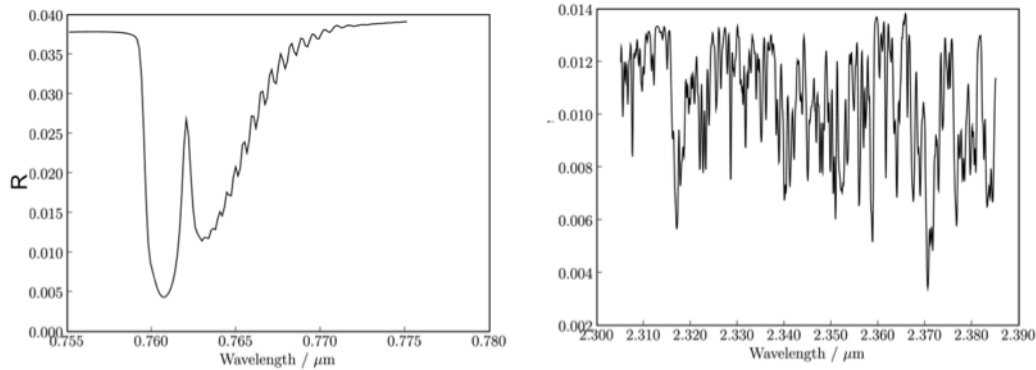
Figure 1: Simulated spectrum at S5P spectral resolution for the O_2 A band (left panel) and the SWIR band (right panel).

4.3   Heritage

The algorithm for retrieval of methane columns from the S5P instrument is based on earlier developments of a CO_2 and CH_4 retrieval algorithm from GOSAT, called RemoTeC [RD20, RD9, RD23, RD16, RD28], making use of measurements at the O_2 A band, and the 1600 nm and 2000 nm CO_2 absorption bands. For CO_2 and CH_4 retrieval from GOSAT the algorithm has been thoroughly tested for simulations where the actual scattering properties are unknown [RD20, RD9], and has been successfully applied to real GOSAT measurements [RD23, RD16, RD28, RD29]. For the operational S5P methane column retrieval algorithm we build further on the RemoTeC algorithm for GOSAT. Here, the algorithm has to be adjusted to the spectral range and spectral resolution of the S5P instrument. We cannot test the algorithm on real measurements for the S5P spectral range (SCIAMACHY measurements do not have sufficient quality in the 2.3 μm range) and therefore we test the S5P algorithm for an ensemble of scenarios with realistic combinations of aerosol properties, cirrus properties, surface albedo, and solar zenith angle, similarly to what was done for GOSAT prior to the GOSAT launch [RD9]. Since the S5P spectral range has no heritage for CH_4 retrieval, it is also important to investigate the quality of the relevant spectroscopic data in this spectral range, which is done using ground based Fourier Transform spectroscopy measurements.

4.4   Requirements

The accuracy requirement for the column integrated dry air-mixing ratio of methane (XCH_4) has originally been formulated as 2% [AD2]. Veefkind et al., 2012 [RD30] formulate this requirement as 2% accuracy and 0.6% precision (defined as the contribution of purely random instrument noise). More recently, the requirement has been reformulated as 1% bias and 1% precision [SD4]. From the 1% bias 0.6% is reserved for instrument related errors and 0.8% for forward model errors. It is also important to keep in mind the performance of the Japanese GOSAT satellite, launched 2009, which sets the current benchmark for methane retrievals from space. Performing GOSAT methane retrievals using the same algorithm as the S5P prototype algorithm [RD23, RD16], for methane we achieve a precision of ~0.8% per individual measurement and a relative accuracy (between regions) of ~0.25%.

Given the large number of measurement provided by the S5P instrument, the requirement on processing speed is very demanding. Taking into account that only cloud-free measurements over land will be processed, which is ~3% of the total daytime data, the requirement on the processing time for a single S5P CH_4 retrieval is in the order of a few seconds assuming a reasonable amount of processing cores.

Table 1: Spectral ranges from the NIR and SWIR band included in the measurement vector

band	used spectral range
NIR	757 774 nm
SWIR	2305-2385 nm

5 Algorithm description

Any retrieval algorithm aims at inferring an atmospheric state vector $\mathbf{x}$ from a measurement vector $\mathbf{y}$. The state vector is linked to the measurement vector through the true forward model $\mathbf{f}(\mathbf{x}, \mathbf{b})$ that depends on the state vector $\mathbf{x}$ and the vector $\mathbf{b}$ containing ancillary parameters that are not retrieved,

$$\mathbf{y} = \mathbf{f}(\mathbf{x}, \mathbf{b}) + \mathbf{e}_y \tag{1}$$

where $\mathbf{e}_y$ represents the measurement noise vector. A retrieval method approximates the true forward model $\mathbf{f}$ by a retrieval forward model $\mathbf{F}$, with a forward model error vector $\mathbf{e}_F$,

$$\mathbf{y} = \mathbf{F}(\mathbf{x}, \mathbf{b}) + \mathbf{e}_y + \mathbf{e}_F . \tag{2}$$

For methane retrieval from the S5P instrument the measurement vector contains the measured radiances in the spectral ranges 757-774 nm of the Near-InfraRed (NIR) channel and 2305-2385 nm in the SWIR channel (see Table 1).

For the retrieval procedure it is needed that the non-linear forward model is linearized so that the retrieval problem can be solved iteratively. For iteration step n the forward model is approximated by

$$\mathbf{F}(\mathbf{x}, \mathbf{b}) \approx \mathbf{F}(\mathbf{x}_n, \mathbf{b}) + \mathbf{K}(\mathbf{x}_n - \mathbf{x}) , \tag{3}$$

where $\mathbf{x}_n$ is the state vector for the n-th iteration step and $\mathbf{K}$ is the Jacobian matrix

$$\mathbf{K} = \frac{\partial \mathbf{F}}{\partial \mathbf{x}} . \tag{4}$$

Below, we will describe the retrieval forward model, state vector, ancillary parameter vector, and the inversion method in more detail.

5.1 Forward model

The retrieval forward model $\mathbf{F}$ simulates the measurement vector $\mathbf{y}$ for a given model atmosphere defined by the state vector $\mathbf{x}$ and the ancillary parameter vector $\mathbf{b}$. The simulated radiance for a given spectral pixel i for S5P is given by

$$I_{\mathrm{conv},i} = \int_{\lambda_{\min}}^{\lambda_{\max}} I(\lambda)\, S_i(\lambda)\, d\lambda \tag{5}$$

where $I(\lambda)$ is the intensity modeled by the radiative transfer code (see below), and $S_i(\lambda)$ is the Instrument Spectral Response Function (ISRF) for spectral pixel i. In the NIR and SWIR channel $I(\lambda)$ contains many fine spectral structures due to molecular absorption, so it has to be calculated line-by-line at fine spectral sampling (at least 0.1 cm^{-1} in the NIR band and 0.02 cm^{-1} in the SWIR). In discretized form we can write the convolution with the ISRF by a matrix equation

$$\mathbf{I}_{\mathrm{conv}} = \mathbf{S}\, \mathbf{I}_{\mathrm{fine}} \tag{6}$$

where $\mathbf{I}_{\mathrm{conv}}$ is a vector containing the intensity measurements for all spectral pixels under consideration, $\mathbf{S}$ is a matrix containing the ISRF for the different spectral pixels, and $\mathbf{I}_{\mathrm{fine}}$ is the modeled intensity spectrum at high spectral resolution. A similar equation can be written for the convolution of the solar spectrum with the ISRF.

In order to model the intensity at high spectral resolution also a high spectral resolution solar spectrum $\mathbf{F}_{0,\text{fine}}$ is needed. We obtain $\mathbf{F}_{0,\text{fine}}$ by performing a deconvolution of the measured solar spectrum $\mathbf{F}_{0,\text{meas}}$:

$$\mathbf{F}_{0,\text{fine}} = \mathbf{S}^T (\mathbf{S}\mathbf{S}^T)^{-1} \mathbf{F}_{0,\text{meas}} \tag{7}$$

The advantage of using a high spectral resolution solar spectrum obtained by deconvolution of the measured solar spectrum is that it is similarly affected by instrument features as the measured intensity spectrum. For further details and overview of the benefits of this method see van Deelen et al., 2007 [RD31].

5.1.1 Model Atmosphere and Optical Properties

For the S5P XCH_4 algorithm described here, the model atmosphere is defined for $NLAY = 36$ homogeneous vertical layers that are equidistant in pressure, the largest pressure level being defined by the surface pressure. The absorbing trace gases of interest are O_2 (in the NIR band) and CH_4, H_2O, and CO in the SWIR band. The layer sub-columns of these gases are for the first iteration step of each retrieval calculated from the input profiles of CH_4, CO (TM5) and H_2O (ECMWF) and the temperature and pressure profiles (ECMWF). They are obtained on the grid of the model atmosphere by linear interpolation. Here, first the surface pressure p_{surf} is obtained by interpolating the input pressure profile as function of height to the surface height (input) for the corresponding ground pixel. Next the pressure values at the layer boundaries are calculated, with the pressure p_k at the lower boundary of layer k (counting from top to bottom) is given by:

$$p_{\text{lev},k} = p_{\text{min}} + \Delta p \cdot k \tag{8}$$
$$\Delta p = (p_{\text{surf}} - p_{\text{min}})/NLAY \tag{9}$$

where $p_{\text{m}in}$ is the pressure value of the upper boundary of the input (ECMWF) atmosphere. The different atmospheric profiles are constructed on this pressure grid. For example, the methane sub-column DV_CH4_k for the layer bounded by pressure levels $p_{\text{lev},k-1}$ and $p_{\text{lev},k}$ is given by:

$$DV\_CH4_k = XCH_{4k}\, DV\_AIR_k \tag{10}$$

where XCH_{4k} is the methane dry air mixing ratio linearly interpolated from the input pressure grid to the pressure at the 'middle' of layer k defined by $(p_k + p_{k+1})/2$. DV_AIR_k is the sub-column of air in layer k, given by

$$DV\_AIR_k = \frac{(p_{\text{lev},k+1} - p_{\text{lev},k})\, R}{M\, g_k \left(1 + \frac{XH_2O_k}{1.60855}\right)} \tag{11}$$

where R is Avogado's number, M is the molecular mass of air, g_k is the gravity constant in altitude layer k, and 1.60855 is the mass of air relative to the mass of water [RD32]. The sub columns of CO and H_2O are calculated in the same manner as for CH_4, and the O_2 sub-column is obtained by multiplying the air sub-column by the O_2 mixing ratio (=0.2095).

For a radiative transfer calculation at a given wavelength the layer absorption optical thickness, scattering optical thickness, and scattering phase function for each model layer are needed. For layer k of the model atmosphere the CH_4 absorption optical thickness at wavelength λ_j is calculated by:

$$\tau_{\text{abs},CH_4}(\lambda_j) = \frac{1}{N} \sum_{i=1}^{N} \sigma(p_i, T_i, \lambda_j)\, DV\_CH4 \tag{12}$$

where N is the number of sub-layers in which the model atmosphere layers are divided (set at $N = 2$) and σ is the absorption cross-section of CH_4 at wavelength λ_j, pressure p_i and temperature T_i at the center of model sub-layer i. The absorption optical thickness for the other trace gases is calculated in the same way. Pre-calculated absorption cross-sections for CH_4, CO, H_2O, and O_2 are stored as lookup-table as a function of pressure, temperature, and wavenumber. These cross-section lookup-tables are calculated from the latest spectroscopic databases [RD33, RD34] assuming Voigt line shapes. For water vapor, an updated spectroscopic line list has been developed by [RD35]. In the NIR spectral range the absorption cross sections of O_2 are calculated according to Tran et al., 2006 [RD36] taking into account line mixing and collision induced absorption. The cross-section for pressure p_i, temperature T_i and wavelength λ_j are obtained by linear interpolation from the tabulated values. The reason that each of the $NLAY$ layers of the model atmosphere is further divided into N sub-layers, is to properly account for the strong dependence of temperature and pressure

of the absorption cross-sections. So, the absorption cross-sections are needed for $NLAY \times N = 36 \times 2 = 72$ vertical layers equidistant in pressure.

The total molecular absorption optical thickness is obtained by summing the contribution of the different trace gases. The Rayleigh scattering optical thickness for layer k and wavelength λ_j is given by

$$\tau_{\mathrm{ray},k} = \sigma_{ray}(\lambda_j)\,DV\_AIR_k \tag{13}$$

where σ_{ray} is the Rayleigh scattering cross section given by [RD37]

$$\sigma_{\mathrm{ray}}(\lambda) = A\,\lambda^{-(4+X)} \tag{14}$$

$$X = B\lambda + \frac{C}{\lambda} - D \tag{15}$$

with $A = 4.02E - 28$, $B = 0.389$, $C = 0.04926$, and $D = 0.3228$. The Rayleigh scattering phase function is given by (e.g. [RD38])

$$P(\Theta) = \frac{3}{4}(1 + \cos^2\Theta)\frac{1-\delta}{1+\delta/2} \tag{16}$$

where δ is the depolarization ratio and Θ is the scattering angle defined by

$$\cos\Theta = -u_0 u_v + \sqrt{(1-u_v)^2}\,\sqrt{(1-u_0)^2}\cos(\phi_0 - \phi_v) \tag{17}$$

where u_0 and u_v are the cosines of the solar and viewing zenith angle, respectively (absolute values) and ϕ_0 and ϕ_v are the solar and viewing azimuth angles.

In addition to trace gases, also aerosols are present in the model atmosphere. In our algorithm, aerosols are described by the following parameters (following [RD20, RD9]):

1. Number of particles in each layer of the model atmosphere. This is provided by the total amount of particles, N_{aer}, and a normalized altitude distribution described by a Gaussian function of center height z_{aer} and width w_0. Hence, in model layer k with central height z_k, the number of particles is given by

$$h(z_k) = N_{aer}\exp\left[-\frac{4\ln(z_k - z_{aer})^2}{4w_o^2}\right] \tag{18}$$

2. A size distribution of $n_{aer}(r)$, described by a power law size function, characterized by power law exponent and upper and lower cut-off (e.g. [RD39]):

$$n(r) = \begin{cases} A & \text{for} \quad r \leq r_1 \\ A\left(\frac{r}{r_1}\right)^{-\alpha} & \text{for} \quad r_1 < r \leq r_2 \\ 0 & \text{for} \quad r > r_2 \end{cases} \tag{19}$$

The cut-offs are $r_1 = 0.1\,\mu\mathrm{m}$, $r_2 = 10\,\mu\mathrm{m}$ and the constant A is determined from normalization of the size distribution. Figure 2 illustrates $n_{aer}(r)$ and compares it to a more realistic multimodal lognormal size distribution [RD40]. Through its parameter α, the aerosol size distribution controls the spectral dependence of aerosol optical properties among the considered retrieval windows.

3. The complex refractive index $m = m_r + i\,m_i$, which is assumed independent of wavelength within a retrieval window.

From the aerosol size distribution, refractive index, and number of particles of each layer the aerosol scattering optical thickness $\tau_{scat,aer}$ and aerosol absorption optical thickness $\tau_{abs,aer}$ are calculated

$$\tau_{\mathrm{scat,aer}}(z_k) = \sigma_{\mathrm{scat,aer}}h(z_k) \tag{20}$$

$$\tau_{\mathrm{abs,aer}}(z_k) = \sigma_{\mathrm{abs,aer}}h(z_k) \tag{21}$$
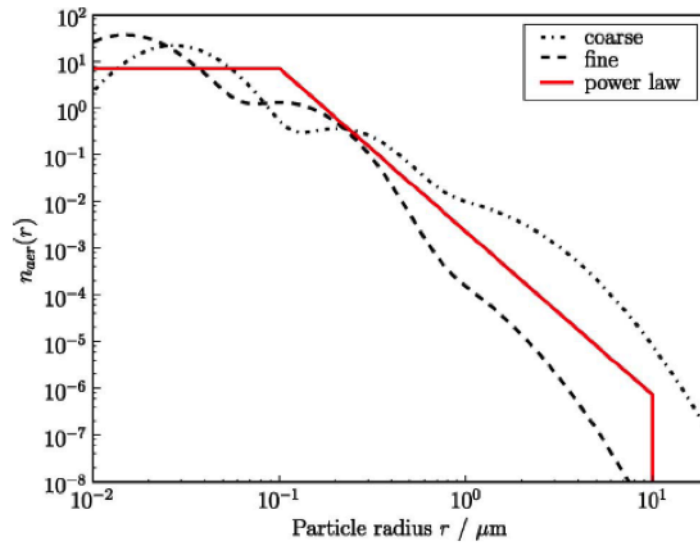
Figure 2: Aerosol size distribution $n_{aer}(r)$ as a function of particle radius r. The retrieval method relies on a power law (red solid) size distribution. Also shown are more realistic multi-modal lognormal size distributions for a fine mode (black dashed) and a coarse mode (black dotted) dominated aerosol type.

where $\sigma_{scat,aer}$ and $\sigma_{abs,aer}$ are the aerosol scattering and absorption cross-section, respectively. They are obtained by:

$$\sigma_{scat,aer} = \sum_{i=1}^{M} K_{scat,i}(m) \, r_i \, n_{aer}(r_i) \, v(r_i) \tag{22}$$

$$K_{scat,i}(m) = \int_{\Delta \ln r_i} \frac{\sigma_{scat}(r,m)}{v(r)} d\ln r \tag{23}$$

where v denotes particle volume and $K_{scat,i}$, representative for particle radius r_i, is pre-calculated for M size bins according to Dubovik et al., 2006 [RD41] and stored in a lookup table as function of aerosol size parameter $x = 2\pi r/\lambda$, real refractive index, and imaginary refractive index. The values for the actual aerosol refractive index are obtained by linear interpolation from the tabulated values. The lookup table contains values for spheres (Mie calculations) as well as for spheroids with a pre-defined axis ratio distribution [RD41], but in our algorithm baseline we only consider spherical particles. Similar expressions hold for the absorption cross-section and the aerosol scattering phase function.

Finally, the total optical properties per layer in the model atmosphere are obtained by combining the contribution of gases and aerosols:

$$\tau_{abs} = \tau_{abs,mol} + \tau_{abs,aer} \tag{24}$$

$$\tau_{sca} = \tau_{scat,mol} + \tau_{scat,aer} \tag{25}$$

$$P(\Theta) = \frac{\tau_{scat,mol}P_{mol}(\Theta) + \tau_{scat,aer}P_{aer}(\Theta)}{\tau_{sca}} \tag{26}$$

For multiple scattering calculations the scattering phase function is needed in the form of expansion coefficients for generalized spherical functions, where expansion coefficient α^l with index l is given by:

$$\alpha^l = \frac{2l+1}{2} \int_{-1}^{1} P_{0,0}^l(\cos\Theta)P(\cos\Theta)d\cos\Theta \tag{27}$$

where $P_{0,0}^l$ is element (1,1) of the Generalized Spherical Function matrix (e.g. [RD42]).

To summarize, the forward model needs the following inputs:

- Surface pressure to define the equidistant pressure grid

- Sub-columns of CH_4, CO, H_2O, O_2, and air for the vertical layers of the model atmosphere.

- Pressure and temperature at the middle of the model sub-layers for absorption cross-sections.

- The aerosol column N_{aer}.

- The aerosol size parameter α (power of the power law size distribution function).

- The central height z_{aer} and width w_0 of the Gaussian aerosol altitude distribution.

- Solar Zenith Angle (SZA).

- Viewing Zenith Angle (VZA).

- Relative Azimuth Angle (RAA).

- The aerosol complex refractive index $m = m_r + i\, m_i$

- A high spectral resolution solar reference spectrum.

- Lookup tables with absorption cross-sections of CH_4, CO, H_2O, and O_2 as function of pressure, temperature, and wavenumber.

- Lookup tables with pre-calculated aerosol properties as function of aerosol size parameter, real refractive index, and imaginary refractive index (cross sections and phase functions integrated over each size parameter bin).

- The surface albedo and its spectral dependence (up to 3 coefficients).

- The fluorescence emission at 755 nm and its first order spectral dependence (see below).

Based on these inputs the optical properties can be calculated for each layer of the model atmosphere.

5.1.2   Modeling the top-of-atmosphere radiances

Based on the optical properties (τ_{abs}, τ_{sca}, $P(\Theta)$) defined for each wavelength and layer of the model atmosphere we can compute the top-of-atmosphere radiance as measured by the S5P instrument. The first step is to separate the radiation field in a singly scattered component I_{ss} and a multiply scattered component I_{ms}, respectively:

$$I = I_{ss} + I_{ms} \tag{28}$$

The computation of I_{ss} for a given wavelength is straightforward:

$$
\begin{aligned}
I_{ss} = F_o \sum_{k=1}^{NLAY} \omega_k P_k(\Theta)\left[1 - e^{-\tau_{tot,k}\left(\frac{1}{u_0}+\frac{1}{u_v}\right)}\right]\frac{u_0}{4\pi(u_0+u_v)}e^{-\sum_{i=1}^{k}\tau_{tot,i}\left(\frac{1}{u_0}+\frac{1}{u_v}\right)} \\
+ e^{-\frac{1}{u_0}\sum_{i=1}^{NLAY}\tau_{tot,i}\left(\frac{1}{u_0}+\frac{1}{u_v}\right)}R_{surf}
\end{aligned}
\tag{29}
$$

where F_0 is the incoming total flux, $\tau_{tot} = \tau_{abs} + \tau_{sca}$, $\omega = \tau_{sca}/\tau_{tot}$, u_0 is the cosine of the solar zenith angle, u_v is the cosine of the viewing zenith angle, and R_{surf} is the surface reflection for the specific solar and viewing geometry under consideration. Besides I_{ss} itself, also the derivatives with respect to $\tau_{sca,k}$, $\tau_{abs,k}$, ω_k and P_k are needed:

$$
\begin{aligned}
\frac{\partial I_{ss}}{\partial \tau_{tot,k}} = F_o \omega_k P_k(\Theta) e^{-\tau_{tot,k}\left(\frac{1}{u_0}+\frac{1}{u_v}\right)}\frac{u_0}{4\pi(u_0+u_v)}e^{-\sum_{i=1}^{k}\tau_{tot,i}\left(\frac{1}{u_0}+\frac{1}{u_v}\right)} \\
- \sum_{k=1}^{K} \omega_k P_k(\Theta)\left[1 - e^{-\tau_{tot,k}\left(\frac{1}{u_0}+\frac{1}{u_v}\right)}\right]\frac{u_0}{4\pi(u_0+u_v)}e^{-\sum_{i=1}^{k}\tau_{tot,i}\left(\frac{1}{u_0}+\frac{1}{u_v}\right)}
\end{aligned}
\tag{30}
$$

$$\frac{\partial I_{\mathrm{ss}}}{\partial P_k} = F_0 \frac{u_0}{4\pi(u_0 + u_v)} e^{-\sum\limits_{i=1}^{k} \tau_{\mathrm{tot},i}\left(\frac{1}{u_0} + \frac{1}{u_v}\right)} \left[1 - e^{-\tau_{\mathrm{tot},k}\left(\frac{1}{u_0} + \frac{1}{u_v}\right)}\right] \omega_k \tag{31}$$

$$\frac{\partial I_{\mathrm{ss}}}{\partial \omega_k} = F_0 \frac{u_0}{4\pi(u_0 + u_v)} e^{-\sum\limits_{i=1}^{k} \tau_{\mathrm{tot},i}\left(\frac{1}{u_0} + \frac{1}{u_v}\right)} \left[1 - e^{-\tau_{\mathrm{tot},k}\left(\frac{1}{u_0} + \frac{1}{u_v}\right)}\right] P_k \tag{32}$$

$$\frac{\partial I_{\mathrm{ss}}}{\partial \tau_{\mathrm{sca},k}} = \frac{1}{\omega_k} \frac{\partial I_{\mathrm{ss}}}{\partial \omega_k} - \frac{\partial I_{\mathrm{ss}}}{\partial \tau_{\mathrm{tot},k}} \tag{33}$$

$$\frac{\partial I_{\mathrm{ss}}}{\partial \tau_{\mathrm{abs},k}} = \frac{\partial I_{\mathrm{ss}}}{\partial \tau_{\mathrm{tot},k}} - \frac{\omega_k}{\tau_{\mathrm{tot},k}} \frac{\partial I_{\mathrm{ss}}}{\partial \omega_k} \tag{34}$$

The computation of the multiply scattered radiation for a given wavelength involves the solution of the plane-parallel radiative transfer equation. We solve this equation using the Gauss-Seidel iterative method. The solution is described in detail by Landgraf et al., 2001 [RD43] and will not be repeated here. The calculation of the derivatives with respect to optical properties per layer k of the model atmosphere is performed using the forward adjoint perturbation theory and is described in detail by Hasekamp and Landgraf, 2005 [RD44].

The radiative transfer calculations yield the derivatives of the radiance with respect to the optical parameters τ_{abs}, τ_{sca}, and P or its expansion coefficients α^l. From these derivatives, the derivatives with respect to a physical parameter x can be calculated in a straightforward manner by the derivative chain rule,

$$\frac{\partial I_{ss}}{\partial x} = \sum_{k=1}^{\mathrm{NLAY}} \left[\frac{\partial I_{\mathrm{ss}}}{\partial \tau_{\mathrm{sca},k}} \frac{\partial \tau_{\mathrm{sca},k}}{\partial x} + \frac{\partial I_{\mathrm{ss}}}{\partial \tau_{\mathrm{abs},k}} \frac{\partial \tau_{\mathrm{abs},k}}{\partial x} + \frac{\partial I_{\mathrm{ss}}}{\partial P_k} \frac{\partial P_k}{\partial x} \right] \tag{35}$$

$$\frac{\partial I_{ms}}{\partial x} = \sum_{k=1}^{\mathrm{NLAY}} \left[\frac{\partial I_{\mathrm{ms}}}{\partial \tau_{\mathrm{sca},k}} \frac{\partial \tau_{\mathrm{sca},k}}{\partial x} + \frac{\partial I_{\mathrm{ms}}}{\partial \tau_{\mathrm{abs},k}} \frac{\partial \tau_{\mathrm{abs},k}}{\partial x} + \sum_{l=0}^{M} \frac{\partial I_{\mathrm{ss}}}{\partial \alpha_k^l} \frac{\partial \alpha_k^l}{\partial x} \right] . \tag{36}$$

In order to avoid time consuming multiple scattering calculations on the high spectral resolution line-by-line grid we aim at reducing the number of spectral calculations, following the approach of Hasekamp and Butz, 2008 [RD27]. For this purpose, we consider the intensity I_{ms} as a function of total absorption optical thickness τ_{abs} and its normalized vertical distribution $\mathbf{n}$ (similar to k-distribution and spectral mapping methods),

$$I_{ms}(\lambda) = I_{ms}(\tau_{\mathrm{abs}}(\lambda), \mathbf{n}(\lambda)) , \tag{37}$$

where we assume that the atmospheric scattering properties and surface reflection properties are constant over the spectral range under consideration. Here, the explicit separation between total absorption optical thickness and its vertical distribution is chosen for later convenience. Element n_k of the vector $\mathbf{n}$ represents the relative contribution of the absorption optical thickness of altitude layer k of the model atmosphere to the total absorption optical thickness of the atmosphere, such that

$$\tau_{\mathrm{abs},k}(\lambda) = n_k(\lambda)\tau_{\mathrm{abs}}(\lambda) , \tag{38}$$

where $\tau_{\mathrm{abs},k}$ is the absorption optical thickness of layer k of the model atmosphere.

For a vertically homogeneous atmosphere, the advantage of the description as function of absorption optical thickness is obvious. Namely, the intensity depends smoothly on absorption optical thickness, which means that only calculations at a limited number of values of τ_{abs} are needed from which the Stokes parameters at other values of τ_{abs} can be obtained by interpolation (see e.g. [RD45]). Finally, the Stokes parameters can be mapped back into wavelength space. To apply this procedure for a non-homogeneous atmosphere, one has to assume that the vertical distribution $\mathbf{n}(z)$ of τ_{abs} can be approximated by a vertical distribution that is independent of wavelength in the spectral interval under consideration. This is the underlying assumption of the correlated k method. For the simulation of moderate- or high resolution spectra in the near- and shortwave infrared spectral ranges, this assumption may cause errors of several percent in reflectance spectra for realistic inhomogeneous terrestrial atmospheres (see e.g. [RD46]).

Clearly, an efficient radiative transfer model is needed that accounts for the vertical distribution of absorption optical thickness at different wavelengths. For this purpose we use the transformation into absorption optical

thickness space, and perform calculations for a limited number N values of $\tau_{\text{abs},k}$ of the absorption optical thickness and corresponding vertical distributions $\mathbf{n}_k$, with $k = 1, \cdots, N$. From the reference calculations $I_{ms}(\tau_{\text{abs},\mathbf{n}_k})$ we want to obtain the multiply scattered intensity vector $I_{ms}(\lambda_j)$ at any wavelength λ_j in the spectral range under consideration with absorption optical thickness $\tau_{\text{abs}}(\lambda_j)$ and its vertical distribution $\mathbf{n}(\lambda_j)$.

The basic principle of our linear-k method is to account for differences between the actual vertical distribution $\mathbf{n}(\lambda_j)$ and the vertical distributions $\mathbf{n}^k$ used in the reference calculations, by employing the linear approximation:

$$I_{ms}(\tau_{\text{abs},k}, \mathbf{n}(\lambda_j)) \approx I_{ms}(\tau_{\text{abs},k}, \mathbf{n}^k) + \frac{\partial I_m s}{\partial \mathbf{n}} \left[\mathbf{n}(\lambda_j) - \mathbf{n}^k \right] , \tag{39}$$

where the derivatives with respect to $\mathbf{n}$ follow from the forward adjoint perturbation theory [RD44]. Applying this equation yields the intensity vector of the multiply scattered radiation at the grid points $\tau_{\text{abs},k}$, corrected for the actual vertical distribution. In order to obtain the intensity I_{ms} at $\tau_{\text{abs}}(\lambda_j)$, we fit a second order polynomial to the logarithm of the (absorption profile corrected) intensities at the grid points, using the grid points closest to $\tau_{\text{abs}}(\lambda_j)$ and the two neighbouring points. In order to correct for variation of scattering properties and surface albedo within the spectral range under consideration, also a linear correction is used.

The grid points are chosen equidistant on a logarithmic scale. For grid point k the total absorption optical thickness is given by:

$$\tau_{\text{grid},k} = e^{\log(\tau_{\text{min}}) + \frac{k-1}{N} \left[\log(\tau_{\text{max}}) - \log(\tau_{\text{min}}) \right]} , \tag{40}$$

where τ_{min} and τ_{max} are respectively the minimum and maximum absorption optical thickness in the spectral window under consideration. If τ_{max} is larger than 15 its value is set to 15, because for larger values of the absorption optical thickness the radiation field is dominated by single scattering (being calculated exactly) and hence interpolation errors are of minor importance. The rationale of choosing a logarithmic scale is to obtain more grid points at small values of absorption optical thickness, where multiple scattering effects are most important. If a certain spectral range is influenced by considerable absorption by two or more species we use 2 grids: one for the target absorber and one for the total of other absorbers. For the radiative transfer calculations in the methane retrieval algorithm we use 10 grid points in the NIR band and $5 \times 4 = 20$ grid points (5 for CH4 and 4 for H2O and CO combined) in the SWIR band. Figure 3 illustrates the accuracy of the linear-k method for the S5P NIR bands. For more information on the linear-k method we refer to [RD27].

5.1.3 Fluorescence

Fluorescence is included in the forward model using the approximation proposed by Frankenberg et al., 2012 [RD47]:

$$I_{\text{TOA}} = I_{\text{TOA}}^{nf} + F_s^{\text{surf}}(\lambda) e^{-\tau(\lambda)/\mu_v} \tag{41}$$

where the fluorescent emission $F_s^{\text{surf}}(\lambda)$ is approximated by

$$F_s^{\text{surf}}(\lambda) = F_{s,755\text{nm}}^{\text{surf}}(1 - s(\lambda - 755)) \tag{42}$$

where the fluorescent emission at 755 nm, $F_{s,755\text{nm}}^{\text{surf}}$, and the wavelength dependence coefficient s are input parameters to the forward model.

5.1.4 Summary of Forward Model

The different steps of the forward model calculation are summarized in Figure 4.

5.2 Inverse algorithm

5.2.1 Definition of state vector and ancillary parameters

The **state vector** $\mathbf{x}$ contains the following elements:

- CH$_4$ sub-columns in 12 vertical layers (layer interfaces coincide with NLAY layers of forward model grid).

- CO total column.
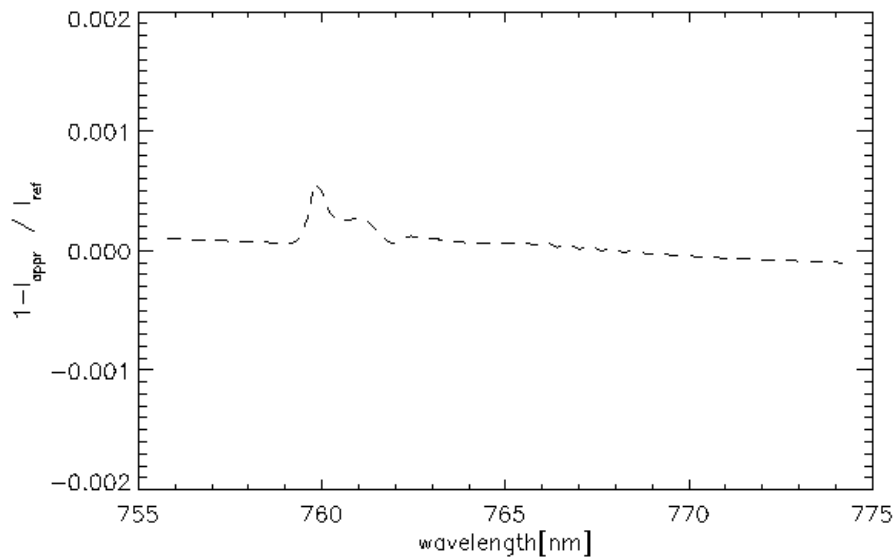
Figure 3: Relative difference between a spectrum calculated using the linear-k method and a spectrum obtained using line-by-line calculations. The spectra have been convolved with a Gaussian spectral response function with a Full Width at Half Maximum (FWHM) of 0.4 nm. For the calculations a boundary layer aerosol was used with an optical thickness of 0.3 at 765 nm. Furthermore, we used a solar zenith angle (SZA) of 50° and a viewing zenith angle of 0°.
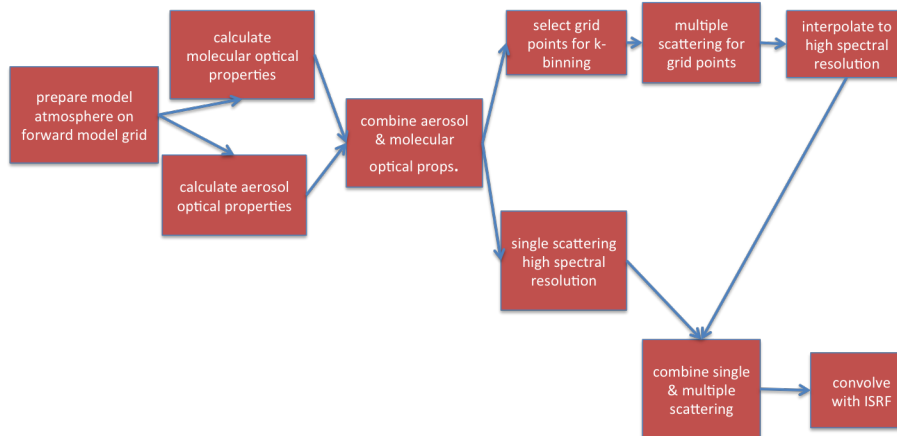
Figure 4: Overview of forward model.

- H_2O total column.

- Aerosol parameter N_{aer} (number column).

- Aerosol parameter α (size parameter).

- Aerosol parameter z_{aer} (central height of Gaussian height distribution).

- Lambertian surface albedo in the NIR band.

- First order spectral dependence of surface albedo in the NIR band.

- Lambertian surface albedo in the SWIR band.

- First order spectral dependence of surface albedo in the SWIR band.

State vector element	A priori value
CH_4 sub-columns	TM5
CO total column	TM5
H_2O total column	ECMWF
Naer	AOT=0.1 at 760 nm
α	fixed at 3.5
z_{aer}	fixed at 5000 m
surface albedo (NIR + SWIR)	no prior value needed (first guess at maximum of measured reflectance)
spectral shifts	no prior needed (first guess = 0)
temperature offset	no prior needed (first guess = 0)
surface pressure	ECMWF + GMTED2010 DEM
fluorescence emission $F_{s,755nm}^{surf}$	from FRESCO
spectral dependence s of fluorescence	fixed at $s = 0$

Table 2: A priori values for the different state vector elements.

- Spectral shift of Earth radiances in the NIR band (higher orders optional).

- Spectral shift of Earth radiances in the SWIR band (higher orders optional).

- offset in the input temperature profile (optional).

- surface pressure (optional).

The **ancillary parameter vector b** contains the following parameters:

- H_2O sub-columns in 36 vertical layers of the forward model grid.

- CO sub-columns in 36 vertical layers of the forward model grid.

- Temperature vertical profile at 72 layers of the cross-section vertical grid.

- Pressure vertical profile at 72 layers of the cross-section vertical grid.

- The aerosol complex refractive index, fixed at $m = 1.4 - 0.01i$ for the NIR and $m = 1.47 - 0.008i$ for the SWIR (no information present in measurement).

- The width w_o of the Gaussian aerosol height distribution, fixed at 2000 m (no information present in measurement).

5.2.2 Inversion Procedure

The inverse method optimizes the state vector $\mathbf{x}$ with respect to the measurements $\mathbf{y}$ after applying the forward model $\mathbf{F}$ to $\mathbf{x}$. The inverse method is based by default on a Phillips-Tikhonov regularization scheme [RD48, RD49, RD44]. Regularization is required because the inverse problem is ill-posed, i.e., the measurements $\mathbf{y}$ typically contain insufficient information to retrieve all state vector elements independently. The inverse algorithm finds $\mathbf{x}$ by minimizing the cost function that is the sum of the least-squares cost function and a side constraint weighted by the regularization parameter γ according to

$$\hat{\mathbf{x}} = \min_x \left\{ \|\mathbf{S}_y^{-\frac{1}{2}}(\mathbf{F}(\mathbf{x}) - \mathbf{y})\|^2 + \gamma\|\mathbf{W}(\mathbf{x} - \mathbf{x}_a)\|^2 \right\} , \tag{43}$$

where $\mathbf{S}_y$ is the diagonal measurement error covariance matrix, which contains the noise estimate. $\mathbf{x}_a$ is an a priori state vector (see Table 2), and $\mathbf{W}$ is a diagonal weighting matrix that renders the side constraint dimensionless and ensures that only the CH_4 parameters and the scattering parameters contribute to its norm: $W_{jj} = 1/x_{a,j}$ for the CH_4 column number densities and the three aerosol parameters, and $W_{jj} = 10^{-7}/x_{a,j}$ for all other state vector elements. The latter are thus retrieved in a least-squares sense. For determining γ, the

L-curve criterion is applied [RD50]. The L-curve is a (double-logarithmic) parametric plot of the least squares norm against the side constraint with γ as parameter. Typically, the L-curve shows a distinct corner for the optimal choice of γ. A γ too small yields a large norm of the state vector, a γ too large yields a large least squares norm.

For the linearized forward model for iteration step n, the equation for the updated state vector $\mathbf{x}_{n+1}$ reduces to

$$\mathbf{x}_{n+1} = \min_x \left\{ \|\mathbf{K}'(\mathbf{x}' - \mathbf{x}'_n) - \mathbf{y}'\|^2 + \gamma \|\mathbf{x}' - \mathbf{x}'_a\|^2 \right\} \tag{44}$$

with the weighted quantities $\mathbf{x}' = \mathbf{W}x$, $\mathbf{y}' = \mathbf{S}_y^{-\frac{1}{2}}(\mathbf{y} - \mathbf{F}(\mathbf{x}_n))$ and $\mathbf{K}' = \mathbf{S}_y^{-\frac{1}{2}}\mathbf{K}\mathbf{W}^{-1}$.

The solution reads

$$\mathbf{x}_{n+1} = \mathbf{G}'\mathbf{y}' + \mathbf{A}'\mathbf{x}'_n + (\mathbf{I} - \mathbf{A}')\mathbf{x}'_{apr} \tag{45}$$

with $\mathbf{A}'$ the averaging kernel matrix and $\mathbf{G}'$ the contribution function matrix given by $\mathbf{A}' = \mathbf{G}'\mathbf{K}'$ and $\mathbf{G}' = (\mathbf{K}'^T\mathbf{K}' + \gamma\mathbf{I})^{-1}\mathbf{K}'^T$. If the retrieval converges after a given number of steps N (typically 7-8), the final state vector $\mathbf{x}_{retr} = \mathbf{x}_N$ is related to the true state vector and to the prior via

$$\mathbf{x}_{ret} = \mathbf{A}\mathbf{x}_{true} + (\mathbf{I} - \mathbf{A})\mathbf{x}_a + \mathbf{G}\mathbf{e}_y + \mathbf{G}\mathbf{e}_f . \tag{46}$$

The covariance matrix $\mathbf{S}_x$ describing the retrieval noise $\mathbf{G}\mathbf{e}_y$ is given by

$$\mathbf{S}_x = \mathbf{G}\mathbf{S}_y\mathbf{G}^T . \tag{47}$$

For the S5P instrument, the target retrieval quantity is the column averaged dry air methane mixing ratio, $X\text{CH}_4$. This quantity is obtained from the methane entries of the retrieved state vector through

$$X\text{CH}_4 = \frac{1}{V_{air,dry}}\mathbf{h}^T\mathbf{x}_{ret} \tag{48}$$

where $\mathbf{h}$ is the total column operator for methane (summing up the partial columns in the state vector) and $V_{air,dry}$ is the dry air column calculated from the surface pressure and water vapor profile, both obtained from a meteorological model (required as input). The retrieval noise $\Delta X\text{CH}_4$ on $X\text{CH}_4$ is given by

$$\Delta X\text{CH}_4 = \frac{\sum\limits_{i,j=1}^{12} S_{x,i,j}}{V_{air,dry}} . \tag{49}$$

This is the error estimate that will be given in the output together with $X\text{CH}_4$.

For validation and application purposes, it is important to realize that the retrieved $X\text{CH}_4$ is in fact a representation of $\mathbf{a}\mathbf{x}_{true}/V_{air,dry}$ where the quantity

$$\mathbf{a} = \mathbf{h}^T\mathbf{A} \tag{50}$$

is referred to as the column averaging kernel [RD51].

5.2.3 Regularization of state vector and iteration strategy

If the true solution is far from the solution of the current iteration $\mathbf{x}_n$ and the forward model $\mathbf{F}$ far from being linear around $(\mathbf{x}_n)$, the linear approximation may fail and yield a solution $\mathbf{x}_{n+1}$ that is further away from the true solution than $\mathbf{x}_n$. To avoid diverging retrievals, we use a Gauss-Newton scheme (see e.g. [RD52]) with reduced step-size by introducing a filter factor that limits the update per iteration step of the state vector. The updated state vector is then given by:

$$\mathbf{x}_{n+1} = \Lambda\mathbf{G}'\mathbf{y}' + \mathbf{A}'\mathbf{x}'_n + (\mathbf{I} - \mathbf{A}')\mathbf{x}'_{apr} \tag{51}$$

with the filter factor Λ given by

$$\Lambda = \frac{1}{1+\xi} \quad \text{with } \xi > 0 . \tag{52}$$

If ξ is large the update of the state vector is small. If $\xi = 0$, the equation for the updated state vector is equivalent to the pure Phillips-Tikhonov equation. The iteration is started with a large ξ, typically on the order of 10. It is then reduced or increased in the following iteration steps according to an empirically found scheme similar to Levenberg-Marquardt strategies [RD52]. We accept solution $\mathbf{x}'_{n+1}$ and decrease ξ by a factor of 2.5 if the least squares norm of iteration $n+1$ is smaller than 1.1 times the least squares norm of iteration n. Otherwise, we discard the solution of iteration $n+1$, increase ξ by a factor of 2.5 and solve again for $\mathbf{x}'_{n+1}$. If ξ is smaller than a threshold value of 0.05, it is set to zero and the iteration is continued without a reduction in step size, assuming that the current state vector is sufficiently close to the true solution to finally converge.

5.2.4   Convergence criteria

The iteration is terminated and the retrieval is considered to have converged to a valid solution $\mathbf{x}_{\mathrm{retr}}$ if the following four conditions are all met:

1. The update of the $X\mathrm{CH_4}$ has become smaller than its theoretical uncertainty.

2. The merit-function has not increased for the current iteration step, and the step-size factor ξ has reached 0.

3. The state vector entries have never reached unrealistic values during the retrieval (negative methane densities for instance).

4. The merit-function divided by the degrees of freedom is smaller than 2.0 (TBC).

5.3   Common aspects with other algorithms

The most important common aspect with the CO algorithm is that non-scattering retrievals performed by the CO algorithm will be input to the $\mathrm{CH_4}$ algorithm for cloud screening purposes (see below). Furthermore, a common aspect with the retrieval algorithm for CO retrieval is the use of a common lookup table for absorption cross sections for $\mathrm{CH_4}$, CO, and $\mathrm{H_2O}$. Another common aspect with the CO algorithm may be the use of a common dataset with prior information on methane (and CO) from an atmospheric transport model. Finally, the here developed highly efficient linear-k binning method for radiative transfer calculations in absorption bands may be useful for aerosol retrievals from the $\mathrm{O_2}$ A band.

5.4   Cloud Filtering

As mentioned above, S5P methane retrievals will only be performed for cloud free ground pixels. Here, the baseline is to use the VIIRS cloud mask re-gridded to the S5P spatial pixels for the NIR and SWIR band (work performed by RAL under ESA contract [RD53]). VIIRS provides 5 different 'confidence' levels for cloudiness ranging from 'confidently clear' to 'confidently cloudy'. The RAL VIIRS product will provide a cloud mask for the S5P pixel itself, referred to as Inner Field Of View (IFOV), and for areas larger than the IFOV by a certain factor, referred to as the Outer Field Of Views (OFOVS). The exact conditions for which a ground pixel is considered sufficiently cloud free to perform a methane retrieval will be evaluated based on real measurements.

For GOSAT, where cloud information is provided by the Cloud and Aerosol Imager (CAI), we found that an appropriate criterion is that 99% of an area equal 4 times that of a ground pixel should be confidently clear. We will also use the VIIRS cirrus reflectance to detect scenes with high cirrus loading which are challenging for the retrieval algorithm. These scenes can be filtered a posteriori. Furthermore, we will filter out scenes for which the difference in cirrus reflectance between the SWIR spatial pixel and the SWIR OFOV exceeds a certain threshold, as for these scenes the co-registration correction algorithm will have limitations. In addition to VIIRS data we use a cloud filter based on S5P measurements itself. This cloud filter is also used as a backup approach in case VIIRS data are not available. For this purpose we use $\mathrm{CH_4}$ and $\mathrm{H_2O}$ columns retrieved from weak and strong absorption bands in the SWIR channel under the assumption of a non-scattering atmosphere. For the $\mathrm{CH_4}$ bands, we choose 2310-2315 nm (weak) and 2363-2373 $\mathrm{n_m}$eter (strong). The difference in columns retrieved from the weak and strong bands increases by increasing cloud optical thickness and/or cloud fraction. So, we filter out scenes for which this difference exceeds a certain threshold. In section Error analysis we will determine appropriate values for these thresholds. The non-scattering retrieval results for the weak and strong $\mathrm{CH_4}$ and $\mathrm{H_2O}$ absorption bands is expected as input for the $\mathrm{CH_4}$ algorithm. They will be produced by a pre-processing step of the S5P CO retrieval algorithm SICOR (see CO ATBD [RD54]). A similar

cloud screening method was developed by the ACOS/OCO-2 team for cloud screening for GOSAT and OCO-2 CO_2 retrievals.

In addition we will use the FRESCO (L2) apparent surface pressure retrieved under the assumption of no scattering by aerosols and clouds. The FRESCO algorithm will be provided by KNMI and will run in the L1-2 processor. We compare the retrieved "apparent" surface pressure with the "true" surface pressure provided by ECMWF. The difference between the values is a measure for modification of the light path due to aerosols and clouds. If the difference exceeds a certain threshold the scene is flagged cloudy. The most important limitation of this cloud filter is that for some values of the surface albedo light path effects in the O_2 A band cancel out [RD55] while clouds are present. Another limitation is due to the ground pixel size of the S5P measurements, because it is required that a larger area than just the ground pixel under consideration is cloud free. Using a cloud filter from S5P itself, this means that also the full adjacent ground pixels should be cloud free. When using VIIRS, with its 1km pixel size, one is much more flexible in defining the area that is required to be cloud free. Due to the limitations in cloud flagging from S5P itself, it is strongly preferred to use VIIRS for cloud and cirrus filtering. Doing cloud filtering using S5P itself should only be considered as a backup approach, but will be fully implemented in the operational processor.

To summarize, the following checks for cloudiness and/or homogeneity are performed within **the baseline approach using VIIRS**:

- Fraction of 'confidently clear' VIIRS pixels within S5P SWIR ground pixel > threshold T_1

- Fraction of 'confidently clear' VIIRS pixels within S5P SWIR Outer Field Of View > threshold T_2.

- Fraction of 'confidently clear' VIIRS pixels within S5P NIR ground pixel > threshold T_3.

- Fraction of 'confidently clear' VIIRS pixels within S5P NIR Outer Field Of View > threshold T_4.

- Average VIIRS cirrus reflectance within SWIR ground pixel < threshold T_5.

- Average VIIRS cirrus reflectance within NIR ground pixel < threshold T_6.

- The difference in VIIRS average cirrus reflectance between the SWIR ground pixel and the SWIR OFOV < threshold T_7.

The additional cloud screening, and fallback approach in case VIIRS data are not available consists of the following checks:

- The difference between the water column $[H_2O]_{weak}$ retrieved from the weak water band and the water column $[H_2O]_{strong}$ retrieved from the strong water band should be < threshold BT_1.

- The difference between $[CH_4]_{weak}$ and $[CH_4]_{strong}$ < threshold BT_2.

- The standard deviation of $[H_2O_{weak} / [H_2O]_{strong}$ within the SWIR pixel and the 8 neighboring pixels < Threshold BT_3.

- The standard deviation of $[CH_4]_{weak} / [CH_4]_{strong}$ within the SWIR pixel and the 8 neighboring pixels < Threshold BT_4.

- The difference between the FRESCO apparent pressure and the ECMWF surface pressure < threshold BT_5.

- The standard deviation of the FRESCO apparent surface pressure in the NIR pixel and the 8 surrounding pixels < threshold BT_6.

The values for the threshold will be determined in the commissioning phase and further optimized during the first year of operation (for re-processing purposes).

5.5 SWIR-NIR Co-Registration

Due to the fact that the measurements in the NIR and SWIR spectral bands are performed by different instrument modules with different characteristics, the measurements in the two different bands are not performed at the same spatial grids. The SWIR pixel size will be approximately 7×7 km^2, while the NIR pixel size will be 3.5×7 km^2 (i.e. factor 2 smaller in the across track direction). The **initial baseline** to deal with spatial co-registration is the most simple and robust one, namely to select the 2 NIR spatial pixels that have largest overlap with the SWIR 7×7 km^2 spatial pixel. If the scattering properties are different for the SWIR and NIR ground pixel (constructed by 2 sub-pixels) this will lead to errors in the retrieved XCH$_4$. Therefore, we will use the VIIRS cirrus reflectance co-added to the SWIR and NIR ground pixels to identify situations where the cirrus contamination for the NIR and SWIR ground pixels deviate too much (threshold TBD during commissioning phase). The corresponding retrieval results will be flagged as erroneous. In case VIIRS data are not available we will use variability of the FRESCO (LV2) retrieved apparent surface pressure to identify inhomogeneous scenes (looking at the NIR ground pixel and its neighbor pixels).

A more accurate NIR-SWIR co-registration can be obtained making use of an image reconstruction scheme. The corresponding algorithm is described in [RD56]. This algorithm will be applied in an off-line processor and, based on one year of data, the added value of this approach will be evaluated (based on validation with ground data, number of valid retrievals). If the more sophisticated image re-construction algorithm has substantial added value in terms of accuracy or number of valid retrievals, it will be used for further- and re-processing of the data.

5.6 Bias correction

We perform a bias correction of the TROPOMI XCH$_4$ data based on the retrieved surface albedo to further improve the accuracy and the fitness for purpose of the TROPOMI CH$_4$ product. This type of correction is also performed for GOSAT CO$_2$ and CH$_4$ and OCO-2 CO$_2$ retrievals (e.g. [RD28, RD57, RD58]) to correct dependencies of the products on different parameters such as goodness of fit, surface albedo or aerosol parameters.

We compared the CH$_4$ retrieval results with collocated GOSAT proxy measurements [RD59] from 31 May 2018 to 13 September 2018. The agreement between both products is very good, with a mean difference of 3.3 ppb, a standard deviation of 21.6 pbb and Pearson's correlation of 0.8 (Figure 5, left panel). We found that the bias is highly correlated with the retrieved surface albedo, while no correlation was found with other parameters (e.g. SZA, χ^2, aerosol parameters). Figure 5 (right panel) shows the TROPOMI-GOSAT ratio as a function of albedo.
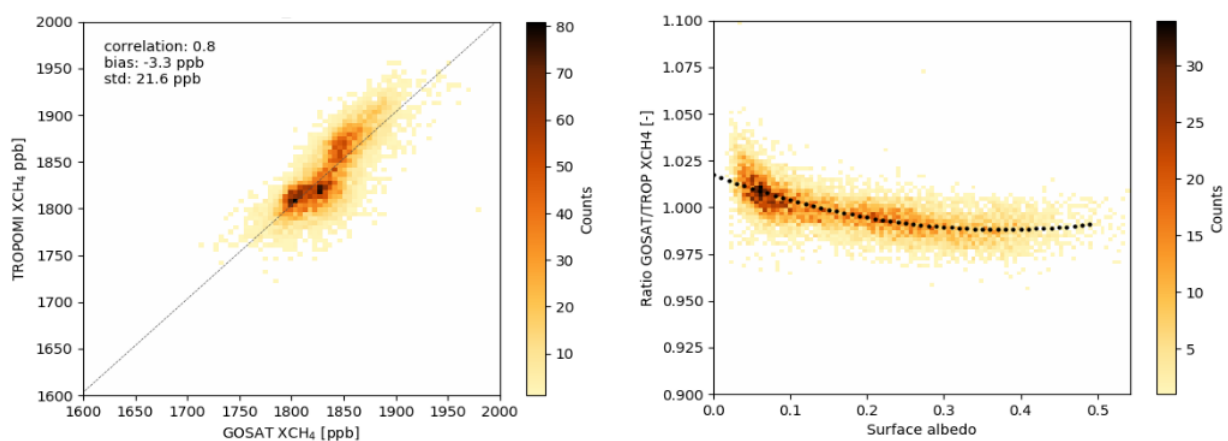
Figure 5: Left panel: correlation plot of TROPOMI and GOSAT CH$_4$ measurements. Right panel: ratio of GOSAT and TROPOMI CH$_4$ as a function of surface albedo. The black dashed line represents the second order polynomial fit from which the correction coefficients in Eq. 54 have been derived.

Based on the correlation of the GOSAT-TROPOMI bias with the surface albedo, we applied a posteriori

bias correction to the S5P-TROPOMI CH$_4$ product. The XCH$_4$ bias corrected product is defined as:

$$\mathrm{XCH}_4^{\mathrm{corr}} = \mathrm{XCH}_4 \cdot (c_1 + c_2 \cdot A + c_3 \cdot A^2) \,, \tag{53}$$

where A is the surface albedo retrieved in the SWIR spectral range and c_1, c_2, c_3 the correction parameters derived from a second order fit to the ratio of TROPOMI and GOSAT CH$_4$ as a function of albedo (doted line in Figure 5, right panel):

$$c_1 = 1.0173, \quad c_2 = -0.1538 \quad \text{and} \quad c_3 = 0.2036 \,. \tag{54}$$

The effect of the bias correction is illustrated in Figure 6, which shows a world map of the differences between the corrected XCH$_4$ and the uncorrected XCH$_4$ for the period 28 November 2018 -16 January 2019. The effect of the bias is an increase of the retrieved CH$_4$ for scenes with relatively low albedo, and a decrease of CH$_4$ for scenes with high albedo (e.g. Sahara desert and Arabic peninsula). Validation results with independent ground-based TCCON measurements shows that the TCCON-TROPOMI bias dependence with albedo is removed in the bias-corrected CH$_4$ product. Furthermore, the agreement between TCCON and CH$_4$ corrected (bias of -4.3 ppb ± 7.4 ppb) improves with respect to the uncorrected CH$_4$ (bias of -12 ppb ± 11.5 ppb).
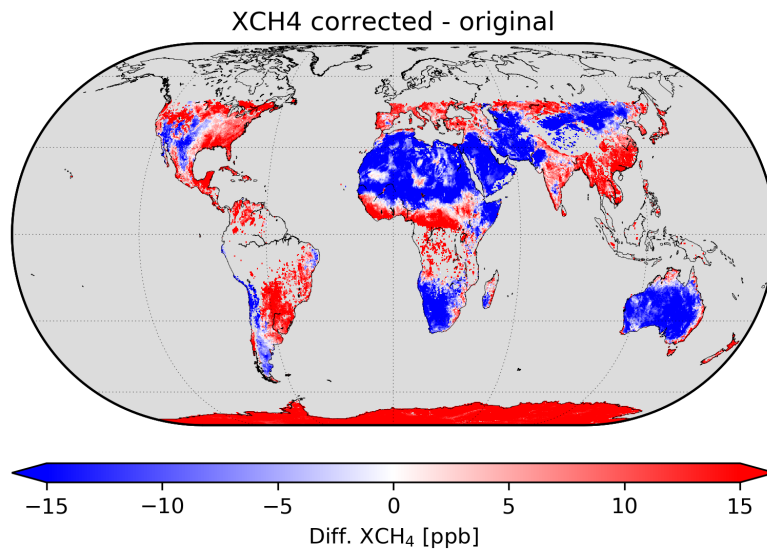
Figure 6: Difference between corrected XCH$_4$ and uncorrected XCH$_4$ averaged in a 0.25° x 0.25° grid for the period 28 November 2018 -16 January 2019.

5.7 Algorithm overview

5.7.1 Required input

Required dynamic input data are listed in Table 3. The methane algorithm expects all dynamic inputs per ground pixel and hence they need to be pre-processed accordingly. The required static input data are listed in Table 4.

Table 3: Dynamic input data for S5P XCH4 algorithm.

Data	Symbol	Units	Source	Pre-Process needs	If not available
S5P level 1b Earth radiance SWIR band	I	mol/s/m^2/nm/sr	S5P level 0-1b product	per ground pixel	no retrieval
S5P level 1b Earth radiance NIR band	I	mol/s/m^2/nm/sr	S5P level 0-1b product	per ground pixel, spatially co-located with SWIR ground pixel	no retrieval
S5P level 1b Solar irradiance SWIR band	$F_{0,\text{meas}}$	mol/s/m^2/nm	S5P level 0-1b product		use previous measurement
S5P level 1b solar irradiance NIR band	$F_{0,\text{meas}}$	mol/s/m^2/nm	S5P level 0-1b product		use previous measurement
latitude	lat	degree	S5P level 0-1b product		no retrieval
longitude	lon	degree	S5P level 0-1b product		no retrieval
solar zenith angle	θ_0	degree	S5P level 0-1b product		no retrieval
viewing zenith angle - SWIR band	θ_v	degree	S5P level 0-1b product		no retrieval
relative azimuth angle –SWIR band	ϕ	degree	S5P level 0-1b product		no retrieval
viewing zenith angle - NIR band	θ_v	degree	S5P level 0-1b product		no retrieval
relative azimuth angle - NIR band	ϕ	degree	S5P level 0-1b product		no retrieval
cloud fraction for S5P SWIR and NIR ground pixel			VIIRS / RAL algorithm	per ground pixel, spatially co-located with SWIR and NIR ground pixel.	use FRESCO apparent pressure and backup cloud screening
cirrus reflectance for S5P SWIR and NIR ground pixel		[-]	VIIRS / RAL algorithm	per ground pixel, spatially co-located with SWIR and NIR ground pixel.	use FRESCO apparent pressure and backup cloud screening
apparent pressure for ground pixel and surrounding		Pa	FRESCO (L2)	find corresponding and neighbouring ground pixel	filter based on retrieved scattering parameters
non scattering retrieval results for weak and strong CH$_4$ and water bands for ground pixel and surroundings	[CH$_4$]$_{\text{weak}}$ [CH$_4$]$_{\text{strong}}$ [H$_2$O]$_{\text{weak}}$ [H$_2$O]$_{\text{strong}}$	mol cm^{-2}	CO algorithm SICOR (L2)	Find corresponding and neighbouring ground pixel	filter based on retrieved scattering parameters

Table 3 – *Continued from previous page*

Data	Symbol	Units	Source	Pre-Process needs	If not available
fluorescence emission at 755 nm	$F^{\mathrm{surf}}_{s,755\mathrm{nm}}$	mol s^{-1} m^{-2} nm^{-1} sr^{-1}	FRESCO algorithm		Assume no fluorescence signal.
atmospheric temperature profile	T	K	ECMWF	interpolated in space and time to SWIR ground pixel / time	no retrieval
atmospheric pressure profile hybrid coefficients	P		ECMWF	calculate pressure profile Interpolated in space and time to SWIR ground pixel / time	no retrieval
vertical profile of specific humidity			ECMWF	interpolated in space and time to SWIR ground pixel / time	use closest in space
surface pressure	P_{surf}	Pa	ECMWF	interpolated in space and time to SWIR measurement	no retrieval
altitude corresponding to ECMWF surface pressure	$z_{\mathrm{surf,ECMWF}}$	m	ECMWF	Interpolated in space and time to SWIR measurement	no retrieval
CH$_4$ a priori vertical profile		mol mol^{-1}	TM5 / SRON	interpolated in space and time to SWIR ground pixel / time	use last available input (in time)
surface wind speed in 2 directions		m/s	ECMWF	interpolated in space and time to SWIR measurement, calculate total windspeed	no retrieval over ocean [1]
CO a priori vertical profile		mol mol^{-1}	TM5 / SRON	interpolated in space and time to SWIR ground pixel / time	use last available input (in time)
mean pixel altitude (NIR and SWIR)		m	GMTED2010	interpolated in space to SWIR ground pixel	no retrieval
standard deviation of altitude within one ground pixel (NIR and SWIR)		m	GMTED2010	Interpolated in space to SWIR ground pixel	no retrieval
land / water mask			GMTED2010 (GTOPO30 not accurate enough)	for SWIR and NIR ground pixel	flag

---

[1] Ocean retrievals are initially performed for validation / verification purposes.

Table 4: Static input data for S5P XCH4 algorithm.

Data	Symbol	Units	Source	Pre-Process needs
absorption cross sections O$_2$	σ_{O_2}	cm^2	[RD36]	calculate cross-sections on fixed wavenumber, pressure, temperature grid (SRON)
absorption cross sections CH$_4$	σ_{CH_4}	cm^2	[RD34]	same as O$_2$
absorption cross sections H$_2$O	σH_2O	cm^2	[RD35] [RD34]	same as O$_2$
model high resolution solar spectrum	F_0	mol/s/ m^2 /nm	TBD	TBD
absorption cross sections CO	σ_{CO}	cm^2	[RD34]	same as O$_2$
LUT with optical aerosol properties			[RD41]	
LUT with cirrus optical properties			[RD60]	
Instrument Spectral Response Function (ISRF) NIR & SWIR	S		Calibration Key Data	
retrieval input settings			SRON	

5.7.2 Algorithm implementation

Figure 7 gives a high level overview of the processing for the CH$_4$ product. The static input (GMTED Digital Elevation MAP, retrieval input settings, cross section lookup tables, and lookup tables with aerosol/cirrus optical properties) needs to be read in only once when the processing starts. Here, the cross section lookup tables will be provided in NetCDF format. The dynamical input consists of the NIR and SWIR level 1b data (e.g. per orbit), the VIIRS cloud data (co-located with the S5P level 1b measurements), the S5P FRESCO level-2 cloud data (apparent pressure), and ECMWF data, TM5 CH$_4$ and CO data (e.g. per day). From the dynamical input data and the GMTED2010 DEM data per ground pixel are being prepared in a pre-processing step. This pre-processing step consists of interpolating the ECMWF data and GMTED2010 DEM data to the coordinates of each S5P ground pixel (assumed to be performed by general KNMI software as this is the same for all S5P products) and co-registration of level 1b data between NIR and SWIR ground pixels. It is assumed that retrievals for individual ground pixels are distributed over different processing threads, where the retrieval per ground pixel is being performed by Fortran90 modules.

Figure 8 shows an overview of the retrieval per ground pixel (see Figure 7), making use of the pre-processed input data for each ground pixel. The first step is to perform the a priori filtering based on cloud data provided by VIIRS. If the ground pixel under consideration contains too much cloud contamination and if the variation in cirrus reflectance between the NIR and SWIR spatial ground pixel is too large (thresholds to be determined in commissioning phase) the retrieval for that ground pixel is not performed. In case VIIRS cloud data is not available homogeneity is being checked by means of the FRESCO apparent pressure for the ground pixel under consideration and its neighbouring pixels. Furthermore, a cloud filtering is being performed based on the retrieved O$_2$ column for a model atmosphere without aerosol and cloud scattering. When this O$_2$ column deviates too much from the value predicted by ECMWF the pixel is considered cloudy.

The next step is to prepare the atmospheric input data to be used in the retrieval, i.e. interpolation to the vertical grid of the retrieval forward model and filling the values of the initial state vector for the retrieval (CH$_4$ profile, CO and H$_2$O column, aerosol parameters, surface albedo). Also, the measurement vector is being
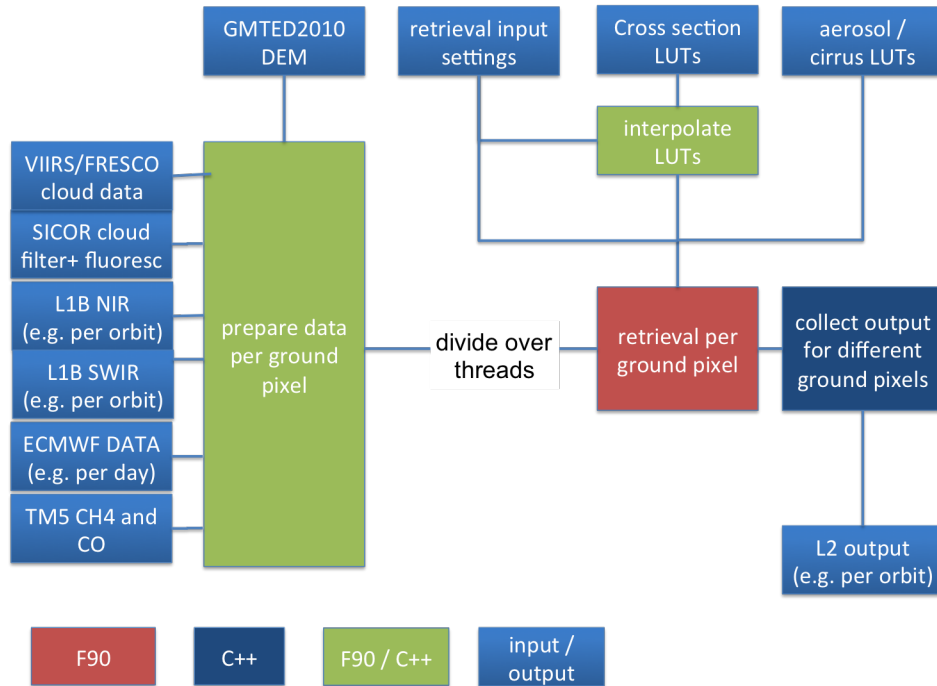
Figure 7: High level overview of $X\mathrm{CH}_4$ processing scheme.
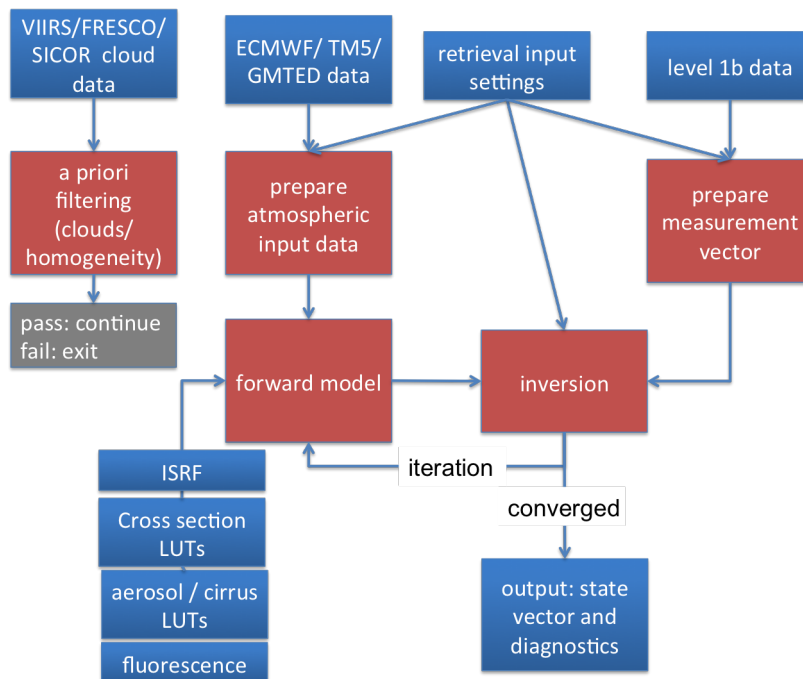
Figure 8: Overview of processing per ground pixel.

prepared from the level 1b input data. (selection of measurements within specified spectral range). Then the iterative scheme starts. A forward model calculation is performed for the first guess state vector and the inversion is performed based on the forward calculation, the measurement vector, and the prior information. This procedure is repeated till convergence has been reached.

6 Feasibility

6.1 Estimated computational effort

The algorithm for the retrieval of methane columns from the S5P instrument as described here has been tested extensively on synthetic measurements under varying atmospheric, surface and viewing conditions. On average, it takes about 7-10 seconds (depending on which retrieval settings are needed in reality, see section Error analysis on a single state-of-the-art PC (64 bit, SPEC_FP rate =237) to perform a methane retrieval for one ground pixel, where the code has been compiled with the GNU Fortran compiler (the Intel compiler leads to an executable that is 2-3 times faster but is not being used in the PDGS). This means, for S5P the processing time will be 7-10 seconds per single pixel if the GNU compiler is the only available compiler. The S5P instruments will provide about 260 measurements per second. However, the number of measurements for which a methane retrieval is performed is significantly less:

- Only measurements at the dayside of the orbit will be considered. This leads to a reduction of 50%.

- Only measurements over land will be considered. This leads to a reduction of 70%.

- Only cloud free measurements (fraction of confidently clear pixels > 99%) will be considered. This leads to a reduction of $\sim 80\%$ (tests with the RAL NPP processor on real VIIRS data show that at a global scale $\sim 22\%$ of the S5P pixels will have a fraction of confidently clear pixels > 99%).

Overall, about 7 measurements per second will be performed that are useful for methane retrieval. Taking the upper estimate of 10 seconds per synthetic retrieval as reference, we estimate roughly 130 processors will be needed to keep track with the S5P (useful) data rate. Note that this number will reduce to ~ 40 if the Intel (ifort) compiler would be used. Obviously, for appropriate re-processing capabilities a certain additional factor is required. The required RAM memory is about 3 Gb.

6.2 Robustness against instrument artifacts

See section 7.

6.3 High level data product description

The output of the $X\mathrm{CH}_4$ algorithm is specified in Table 5.

Table 5: Contents of the output product.

Name/ Data	Symbol	Units	Description	Data type	Dimen-sion
time		s	time of measurements	float	1
latitude, latitude_bounds	lat	degree	SWIR pixel latitude (center & corners)	float	1,4
longitude, longitude_bounds	lon	degree	SWIR pixel longitude (center & corners)	float	1,4
solar_zenith_angle	θ_0	degree	solar zenith angle at pixel center	float	1
viewing_zenith_angle	θ_v	degree	viewing zenith angle at pixel center	float	1
methane_mixing_ratio	$X\mathrm{CH}_4$	ppb	column averaged dry air mixing ratio of CH_4	float	1
methane_mixing_ratio_bias_-corrected	$X\mathrm{CH}_4$	ppb	bias corrected $X\mathrm{CH}_4$	float	1
methane_mixing_ratio_-precision	$\Delta X\mathrm{CH}_4$	ppb	precision of $X\mathrm{CH}_4$	float	1
qa_value			QA value for CH_4	int	1

Table 5 – *Continued from previous page*

Name/ Data	Symbol	Units	description	Data type	dimension
number_of_iterations			number of iterations for the CH_4 retrieval	int	1
column_averaging_kernel	**a**		column averaging kernel [2]	float	12
altitude_levels	z	m	height levels of retrieval grid	float	13
surface_pressure	p_{surf}	hPa	surface pressure	float	1
pressure_interval	dp	Pa	pressure difference between levels in the retrieval	float	1
dry_air_subcolumns	DVAIR	mol m^{-2}	dry air layer sub columns	float	12
methane_profile_apriori		mol m^{-2}	a priori CH_4 profile in layer sub-columns	float	12
carbonmonoxide_total_column	VCO	mol m^{-2}	CO total column (not official product)	float	1
carbonmonoxide_total_column_ precision	ΔVCO	mol m^{-2}	error on VCO	float	1
water_total_column	VH2O	mol m^{-2}	H_2O total column	float	1
water_tota_column_ precision	$\Delta VH2O$	mol m^{-2}	error on VH2O	float	1
aerosol_size	α		aerosol size parameter	float	1
aerosol_size_precision	$\Delta\alpha$		error on aerosol size parameter	float	1
aerosol_number_column	N_{aer}	m^{-2}	aerosol number column	float	1
aerosol_number_column_ precision	ΔN_{aer}	m^{-2}	error on aerosol_amount	float	1
aerosol_mid_altitude	z_{aer}	m	central height of aerosol altitude distribution	float	1
aerosol_mid_altitude_- precision	Δz_{aer}	m	error on aerosol height z_{aer}	float	1
surface_albedo_SWIR	A_{SWIR}		surface albedo in SWIR band	float	1
surface_albedo_SWIR_ precision	ΔA_{SWIR}		precision of SWIR albedo	float	1
surface_albedo_NIR	A_{NIR}		surface albedo in NIR band	float	1
surface_albedo_NIR_precision	ΔA_{NIR}		precision of the NIR albedo	float	1
aerosol_optical_thickness_ SWIR	τ	τ_{aer}	AOT in SWIR band	float	1
aerosol_optical_thickness_ NIR	τ	τ_{aer}	AOT in NIR band	float	1
chi_square	χ^2		chi squared of fit in both bands	float	1
chi_square_swir			chi squared of fit in SWIR band	float	1

Continued on next page

---

[2] works on subcolumns

Table 5 – *Continued from previous page*

Name/ Data	Symbol	Units	description	Data type	dimen-sion
chi_square_nir			chi squared of fit in NIR band	float	1
degrees_of_freedom	DFS		Degrees of Freedom for Signal	float	1
degrees_of_freedom_methane			DFS for CH_4 profile	float	1
degrees_of_freedom_aerosol			DFS for aerosol parameters	float	1
cloud_fraction_VIIRS_NIR_ IFOV			Cloud fraction from VIIRS data in the NIR channel for the instantaneous field of view (band 6)	float	1
cloud_fraction_VIIRS_NIR_ OFOVa			Cloud fraction from VIIRS data in the SWIR channel for the 10% upscaled field of view	float	1
cloud_fraction_VIIRS_NIR_ OFOVb			Cloud fraction from VIIRS data in the SWIR channel for the 50% upscaled field of view	float	1
cloud_fraction_VIIRS_NIR_ OFOVc			Cloud fraction from VIIRS data in the SWIR channel for the 100% upscaled field of view	float	1
cloud_fraction_VIIRS_SWIR_ IFOV			Cloud fraction from VIIRS data in the NIR channel for the instantaneous field of view (band 6)	float	1
cloud_fraction_VIIRS_SWIR_ OFOVa			Cloud fraction from VIIRS data in the SWIR channel for the 10% upscaled field of view	float	1
cloud_fraction_VIIRS_SWIR_ OFOVb			Cloud fraction from VIIRS data in the SWIR channel for the 50% upscaled field of view	float	1
cloud_fraction_VIIRS_SWIR_ OFOVc			Cloud fraction from VIIRS data in the SWIR channel for the 100% upscaled field of view	float	1
reflectance_cirrus_VIIRS_ SWIR			Cirrus reflectance from VIIRS for the SWIR ground pixel	float	1
reflectance_cirrus_VIIRS_NIR			Cirrus reflectance from VIIRS for the NIR ground pixel	float	1
methane_weak_twoband_total_ column	$[CH_4]_{weak}$	mol m^{-2}	SICOR retrieved CH_4 column from weak absorption band	float	1

Table 5 – *Continued from previous page*

Name/ Data	Symbol	Units	description	Data type	dimen-sion
methane_strong_twoband_total_column	$[CH_4]_{strong}$	mol m^{-2}	SICOR retrieved CH$_4$ column from strong absorption band	float	1
water_weak_twoband_total_column	$[H_2O]_{weak}$	mol m^{-2}	SICOR retrieved H$_2$O column from weak absorption band	float	1
water_strong_twoband_total_column	$[H_2O]_{strong}$	mol m^{-2}	SICOR retrieved H$_2$O column from strong absorption band	float	1
methane_ratio_weak_strong_standrad_deviation			Standard deviation of ratio of CH$_4$ columns from weak and strong band for 9 pixels (ground pixel plus 8 neighbours)	float	1
water_ratio_weak_strong_standard_deviation			Standard deviation of ratio of H$_2$O columns from weak and strong band for 9 pixels (ground pixel plus 8 neighbours)	float	1
apparent_scene_pressure		hPa	apparent surface pressure of FRESCO for NIR band	float	1
apparent_scene_pressure_standard_deviation		hPa	standard deviation of PSURF_FRESCO for 9 pixels (center and 8 neighbors)	float	1
surface_altitude		m	surface elevation of S5P SWIR pixel	float	1
surface_altitude_precision		m	standard deviation of surface elevation within SWIR pixel	float	1
fluorescence	$F_{s,755nm}^{surf}$	mol/s/cm^2/nm	retrieved fluorescence signal at 755 nm	float	1
fluorescence_apriori		mol/s/cm^2/nm	apriori fluorescence signal at 755 nm	float	1
wavelength_calibration_-offset_swir		nm	fitted correction to wavelength calibration	float	1
wavelength_calibration_-offset_nir		nm	fitted correction to wavelength calibration	float	1

The output product consists of the retrieved methane column and a row vector referred to as the column averaging kernel **A**. The column averaging kernel describes how the retrieved column relates to the true profile and should be used in validation exercises (when possible) or use of the product in source/sink inverse modeling. The output product also contains altitude levels of the layer interfaces to which the column averaging kernel corresponds. Additional output for Level-2 data products: viewing geometry, precision of retrieved methane, residuals of the fit, quality flags (cloudiness, terrain roughness etc.) and retrieved albedo and aerosol properties. The latter properties are required for a posteriori filtering and for estimation of total retrieval error.

6.4 Data selection approach

First, only select those data that meet the following criteria (a priori filtering in Figure 8): Determine for each measured pixel in the S5P swath if:

- Spectrum intensity above threshold level (prefilters for ocean and snow). For synthetic data, a minimum albedo of 0.02 in the SWIR was found to be necessary to yield acceptable retrieval accuracy.

- Above land.

- Cloud / cirrus coverage and variation: perform cloud checks as described in section 5.4.

- SZA < 70 degree. For larger angles, the plane-parallel treatment of scattering processes introduces too large errors, and the signal-to-noise-ratio is generally insufficient for a retrieval

- Mountainous areas will be excluded. The GOSAT team filter out all pixels with a surface roughness (= standard deviation of altitudes) larger than 75 m (derived from GMTED2010 data). A similar criterion is intended for TROPOMI.

- Instrument zenith angle below 60 degree, i.e. preference is given to those pixels in the swath that are closer to instrument nadir.

Based on retrievals from real S5P measurements the filters will be fine-tuned during the first year of operation.

6.5   Treatment of Corrupted data

A pixel mask (good or bad pixels) is being determined per orbit as part of the in-flight calibration. The methane retrieval for a certain ground pixel starts only if the number of good pixels is larger than a certain threshold (70%). As an additional safety check for corrupted / unphysical data we will quit the iterative retrieval in the first iteration step if the χ^2 difference between the measurement and forward model calculation (based on the first guess parameters) exceeds a certain threshold.

6.6   Timeliness

The methane retrieval will not take place in the near-real-time data stream. All of the necessary auxiliary information either exists already today or will be delivered by the S5P housekeeping data. The only critical issue is the availability of VIIRS information on cloud coverage as soon as possible after a S5P overpass.

Table 6: Performance of the reference retrieval for the ensemble of 9030 synthetic measurements.

	unfiltered	**filtered**
mean CPU time per retrieval	7.6 s	
success rate	95% (converged)	61% (converged and filtered)
RMS forward model error	1.1%	0.45%
RMS retrieval noise (due to instrument noise)	0.77%	0.37%
fraction of retrievals with $|X\mathrm{CH}_4$ error$| < 1\%$	86%	96%

7 Error analysis

First, the performance of the reference retrieval for a global ensemble of synthetic measurements is presented in Sect. 7.1. Thereafter, the impact of model and instrument errors on the retrieved $X\mathrm{CH}_4$ is discussed in Sects.7.2 and 7.3, respectively. It should be noted that the effect of chlorophyll-fluorescence on the measured radiances in the NIR band is not taken into account in this. In analogy with the study by Frankenberg et al., 2012 [RD47], who studied the effect of fluorescence on $X\mathrm{CO}_2$ retrievals from GOSAT and OCO-2, we expect this error to be smaller than the other error sources discussed here. However, the error is not negligible and therefore we plan to implement the capability to model the effect of fluorescence in an update of the S5P methane algorithm.

7.1 Simulation of geophysical test cases

In order to quantify the retrieval error on the $X\mathrm{CH}_4$ induced by the presence of cirrus and aerosol, an ensemble of 9030 simulated measurements has been generated that covers the range of scenes that will be likely encountered by the TROPOMI instrument. The details how these synthetic spectra were created are explained in the Appendix. Here, we present the performance of the algorithm when retrieving them.

The term "retrieval error" in this section describes the forward model error $\mathbf{Ge}_F$ (caused by approximate treatment of aerosols) divided by the true $X\mathrm{CH}_4$. The error due to instrument noise ($\mathbf{Ge}_F$) is subtracted from the retrieved state vector. The retrieval noise is evaluated separately in Sect. 7.3.1.

The world map in Figure 9 shows the forward model error of $X\mathrm{CH}_4$ for the reference retrieval with three aerosol retrieval parameters. The relative error is largest for scenarios with a high aerosol load over bright surfaces (red pixels at the Sahara in summer time), high cirrus load over dark surfaces (e.g. tropical Africa), and/or with a large SZA (Northern Eurasia in January).

From the simulated retrievals we found that the information content of the average spectrum is sufficient to retrieve the three aerosol parameters in our algorithm: The total number of aerosols ($N\mathrm{aer}$), the height of the aerosol layer (h) and the exponent of the power-law size-distribution (α). Here, the information on size comes from the spectral dependence between the NIR and SWIR band, and information on amount and height comes from the large range in absorption optical thickness in both bands. The same selection was found to be optimal for GOSAT data.

The retrieval errors in Figure 9 are in particular large if there is a layer at large altitude with large AOT and with large particles (i.e. small value of α). Therefore, we filtered the converged retrievals a posteriori by rejecting all retrievals for which $f = \mathrm{AOT}_{\mathrm{SWIR}} \times \frac{h}{\alpha} < 110$. (This relation was found empirically.) Additionally, we also requested that the retrieved surface albedo in the SWIR band should be > 0.02.

Figure 10 shows the $X\mathrm{CH}_4$ error as a function of the retrieved SWIR albedo (left panel) and aerosol filter parameter f (right panel). It can be seen that for cases with low SWIR albedo and high f, the error scatter increases. The cut-offs of 0.02 and 110 will have to be fine-tuned for real data, optimizing for accuracy versus data quantity. About 50% of all retrievals converged and passed the a posteriori filters. Figure 11 shows the a posteriori filtered world map.

Figure 12 and Table 6 summarizes the error characteristics of the reference retrieval with three aerosol parameters without 9 and with (Figure 11) the two a posteriori filters for f and SWIR albedo.
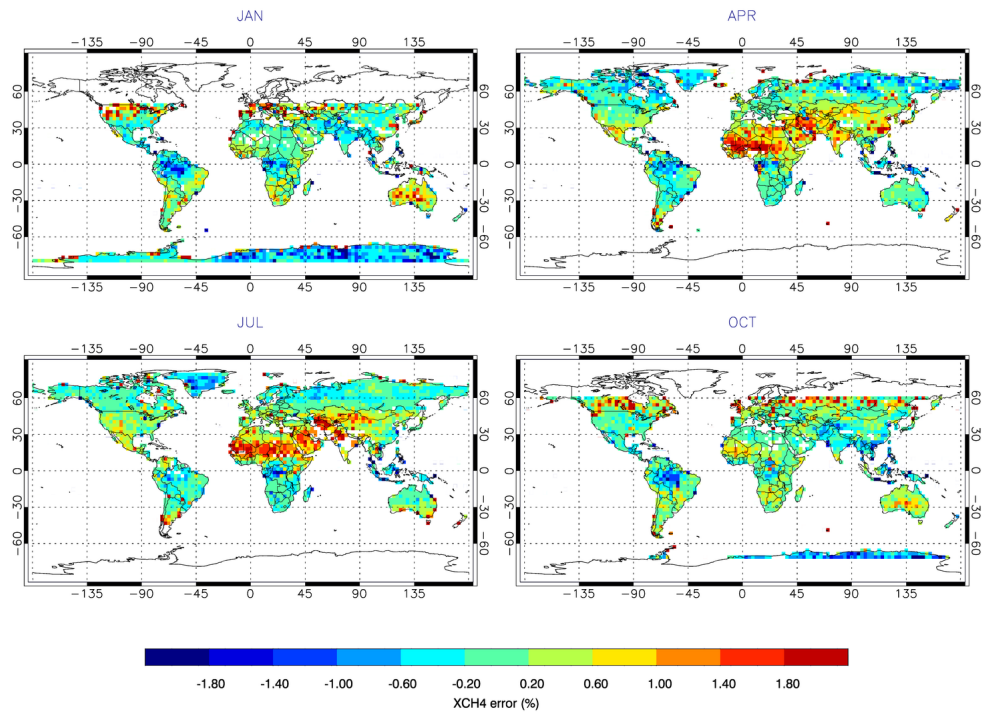
Figure 9: Retrieval forward model error of $X\mathrm{CH}_4$ for the (unfiltered) reference retrieval. White colors indicate retrievals did not converge, or synthetic spectra were not calculated (oceans), or SZA > 70 degree. The $X\mathrm{CH}_4$ error is defined as the difference between the retrieved and the true value and relative values are calculated with respect to the true $X\mathrm{CH}_4$.
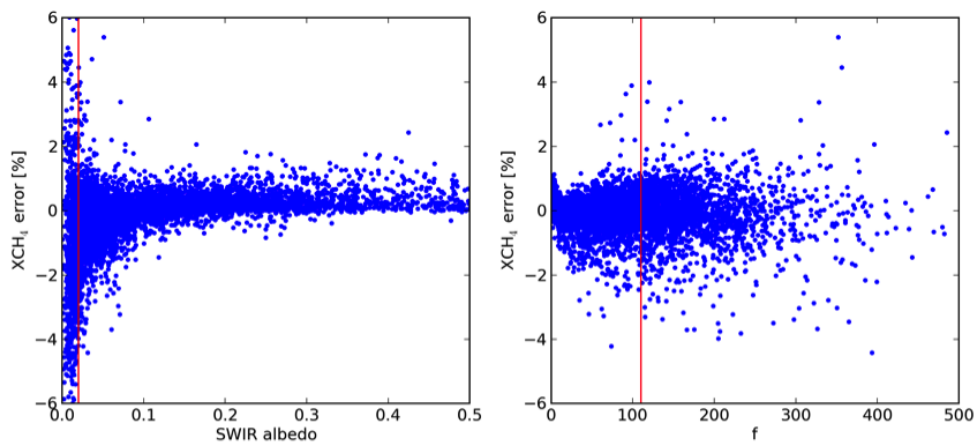
Figure 10: Forward model error of $X\mathrm{CH}_4$ plotted against retrieved SWIR albedo (left panel) and aerosol filter parameter f (right panel). The vertical lines give the cut-offs for the a posteriori filters. Retrievals with SWIR albedo < 0.02 are already filtered out in the right panel.
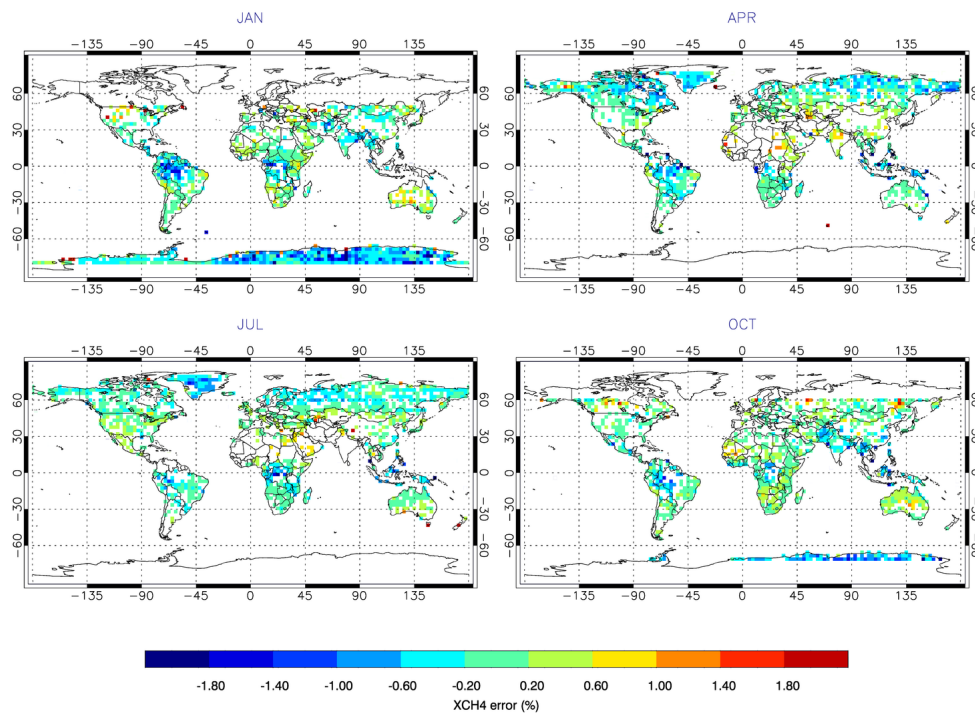
Figure 11: Forward model error of $X\mathrm{CH}_4$ after applying the a posteriori filter: SWIR albedo > 0.02 and aerosol load not too high (f < 110).

7.2 Model errors

7.2.1 Spectroscopic data

Galli et al. 2012 [RD61] investigated if the absorption features of the three relevant molecules CH_4, CO, and $\mathrm{H}_2\mathrm{O}$ in the SWIR range were adequately known by inverting ground-based Fourier transform spectrometers (FTS) measurements obtained by the TCCON group. The TCCON FTS observe direct sun light, therefore all scattering effects can be neglected, and only molecular absorption needs to be included in the retrieval forward model. On the other hand, the TCCON FTS measure a broad spectral range in the NIR and SWIR at a 30 times higher spectral resolution than the TROPOMI SWIR channel. This makes the TCCON spectra ideally suited to test spectroscopic line lists.

Combining the inverse algorithm presented by Butz et al. 2012 [RD62] with a simple forward model without scattering, Galli et al. 2012 [RD61] retrieved CH_4, $\mathrm{H}_2\mathrm{O}$, and CO from various spectral ranges at different spectral resolutions. Most relevant to this document is the comparison between the CH_4 columns retrieved from the TROPOMI range at the TROPOMI resolution and the CH_4 results obtained from the 1.6 μm region at the higher TCCON resolution. The CH_4 columns were reproduced to an accuracy of 0.3% apart from a constant bias of 1%. No strong correlation with $\mathrm{H}_2\mathrm{O}$ abundance was found. We caution, however, that the intrinsic retrieval accuracy of CH_4 from TCCON spectra is a few tenths of a percent. This means only spectroscopic deficiencies could be identified that result in column errors with the same order of magnitude as the intended accuracy for the S5P mission. When surface pressure was retrieved as well, Galli et al., 2012 [RD61] found an incorrect pressure-dependence at the TROPOMI SWIR range, both for CH_4 and for $\mathrm{H}_2\mathrm{O}$. This implies that not only the $\mathrm{H}_2\mathrm{O}$ but also the CH_4 line list (in particular the pressure broadening and pressure shift parameters) is less accurate at the TROPOMI range than around 1.6 μm.
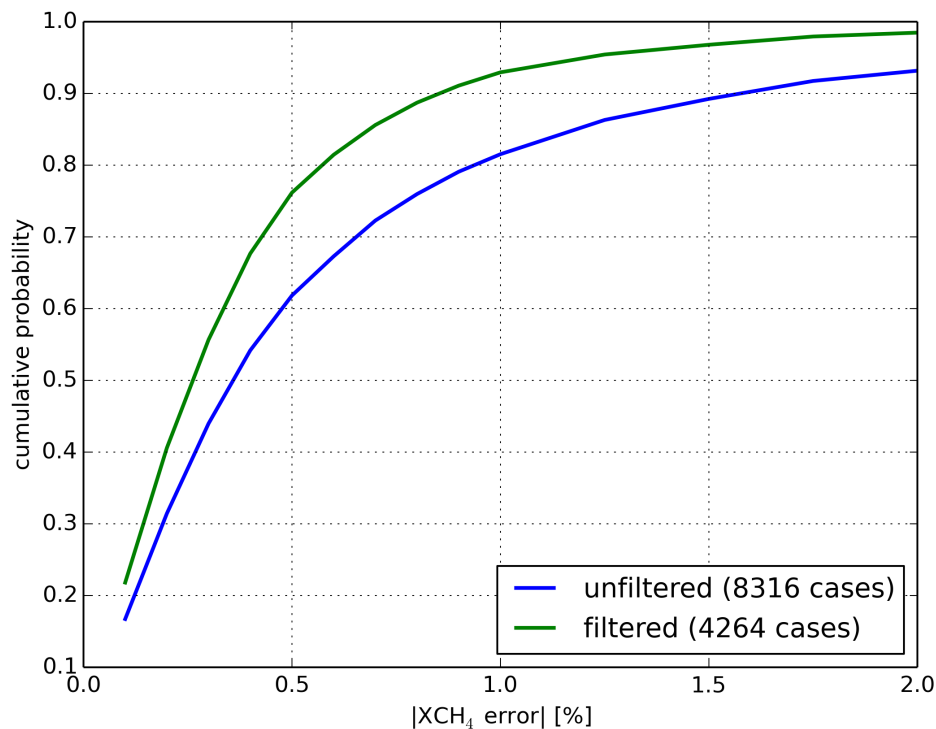
Figure 12: Cumulative probability distribution of the absolute $X\mathrm{CH_4}$ retrieval error for the reference retrieval that includes scattering of aerosols (green: all converging retrievals, blue: a posteriori filters applied to results).
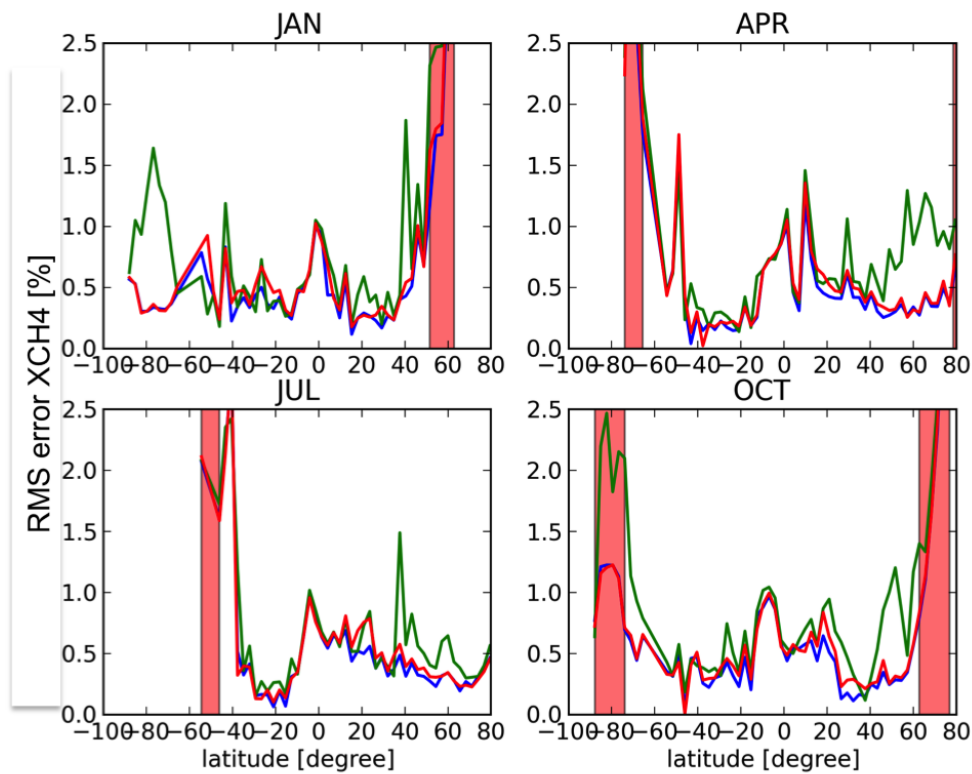
7.2.2 Temperature profile

An erroneous temperature profile affects the retrieval performance through the temperature depencence of the cross-sections. To investigate this, the mean temperature profile per latitude is used in the retrieval forward model instead of the true temperature profile. This is an overestimation of the temperature error expected from ECMWF and should hence be considered as a worst case scenario. The algorithm allows the option to fit a temperature offset and the performance is evaluated with this option switched on and off.

In Figure 13 the error characteristics are compared to the reference retrieval with a posteriori filters. The reduction in successfull cases is mainly due to non-convergence. Fitting a temperature offset can to some extent compensate for an error in the temperature profile. However, testing with real observations is needed to decide how many parameters can and are required to be fitted.

7.2.3 Surface Pressure

An erroneous pressure profile affects the retrieval of $X\mathrm{CH_4}$ in two ways: first of all, through pressure dependence of the cross-sections and, secondly, through the retrieved air column that is used to convert the $\mathrm{CH_4}$ total column to the dry air mixing ratio, $X\mathrm{CH_4}$. The lattter will introduce a retrieval error of the same magnitude as the pressure error. The algorithm allows the option to fit the surface pressure. To investigate the performance of this optional fit, the prior pressure profile is perturbed with a scaling factor up to ± 1%. Figure 14 and Table 7 show the results with and without fitting the surface pressure. In case the pressure is fitted the forward model error is the same as for the reference case. However, it should be noted that fitting the surface pressure from real measurements may be difficult. For example, in our retrievals from GOSAT, with its much higher spectral resolution, retrieval of surface pressure from real measurements is not possible. From the simulations where we do not fit the surface pressure we conclude that for surface pressure errors up to 0.2% (roughly 2 hPa) the effect on the retrieved $X\mathrm{CH_4}$ is < 0.2%. It is expected that the ECMWF pressure together with the GMTED2010 Digital Elevation map allow to achieve this accuracy.

Figure 13: Sensitivity of $X\mathrm{CH}_4$ retrieval to error in temperature profile. Upper panel: Cumulative probability distribution of the absolute $X\mathrm{CH}_4$ retrieval error for the reference retrieval (blue), retrieval of ensemble with mean temperature profile per latitude without (green) and with (red) fitting of temperature offset. Lower panels: RMS error of $X\mathrm{CH}_4$ per latitude bin for same simulation runs as in upper panel. The red areas indicate regions with high SZA that we plan to filter out.

Table 7: Sensitivity of retrieval performance to model errors in methane, water, temperature and pressure profiles. The results for retrievals with a temperature offset and surface pressure fitted are shown in brackets.

	converged	converged and filtered	RMS forward model error (filtered data)	CPU time per retrieval
reference	95%	61%	0.45%	7.6 s
mean CH_4 profile, $\Delta\mathrm{CH}_{4\mathrm{col}}$=2%	95%	61%	0.46%	7.6 s
mean $\mathrm{H}_2\mathrm{O}$ profile, $\Delta\mathrm{H}_2\mathrm{O}_{\mathrm{col}}$=10%	88%	54%	0.48%	9.4 s
mean T profile (T_{offset} fitted)	72% (91%)	40% (57%)	0.77% (0.50%)	11.1 s (7.9 s)
δP=0.5% (P_{surface} fitted)	83% (96%)	51% (61%)	= 0.76% (0.46%)	7.6 s (8.2 s)

7.2.4 Absorber profiles

CH_4 profile

A robust retrieval algorithm should be able to solve the inverse problem regardless of its first guess information. To test this, a normalized mean CH_4 profile per latitude is taken as first guess. We normalize the mean profile such that the prior total column is a factor times the true column. In this way, the effect of an error on the profile can be distinguished from an error on the column. The CH_4 column error is varied up to ±2%. Figure 15
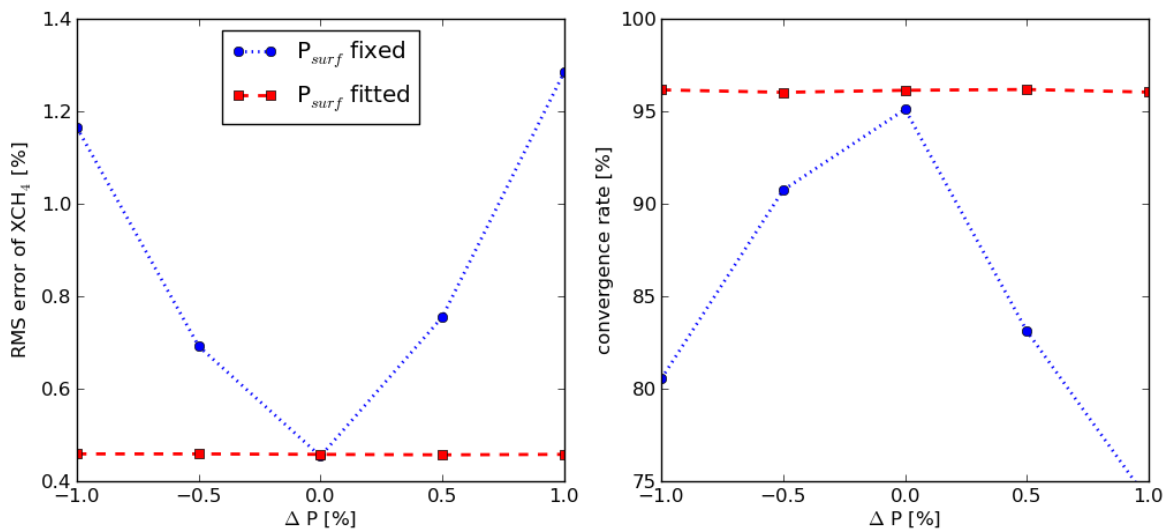
Figure 14: Influence of model error in prior pressure profile on accuracy (left) and stability (right) of retrievals without (blue) and with (red) fitting of the surface pressure.

shows reassuringly that the first guess CH_4 profile has a negligible influence on the retrievals.

H_2O profile

The error on the prior H_2O profile is established in the same way as for CH_4, i.e. by taking a normalized mean profile per latitude. Note that for H_2O, there is an additional (minor) influence on the retrieval of XCH_4 through the dry air column. The H_2O column error is varied up to ±10%. Figure 15 shows that the prior H_2O profile has some influence on the RMS error (+0.03%) and convergence (-7%). It is expected that the ECMWF information on H_2O is more accurate than what we used in our sensitivity study so the errors shown here should be considered as worst case.
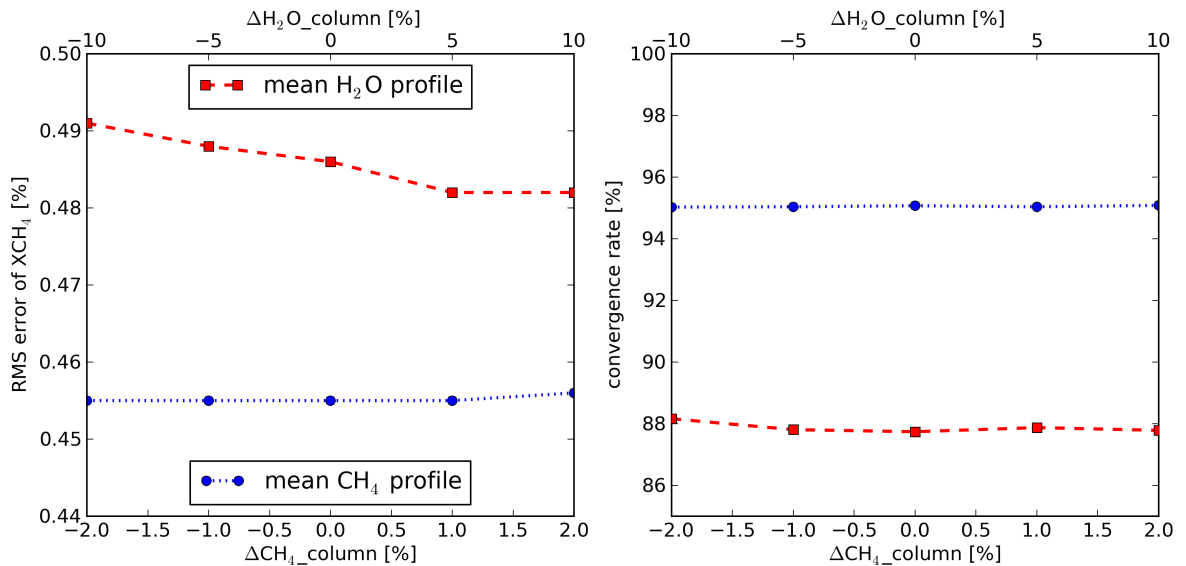
Figure 15: Influence of model errors in prior absorber profiles, CH_4 (blue) and H_2O (red), on retrieval accuracy (left) and stability (right).

7.3 Instrument errors

In this section, the sensitivity of the retrieval performance to relevant instrument and calibration errors is investigated. Where possible, the errors are set by the spectral and radiometric requirements as described in the System Requirement Document (SRD) [RD63].

7.3.1 Signal to noise ratio

The simulated spectra include noise based on the TROPOMI requirements as described in the SRD. For the NIR and the SWIR band signal-to-noise ratios in the continuum of 500 and 100, respectively, have been adopted. The precision is given by the retrieval noise $\sigma_{X\mathrm{CH}_4}$. The wo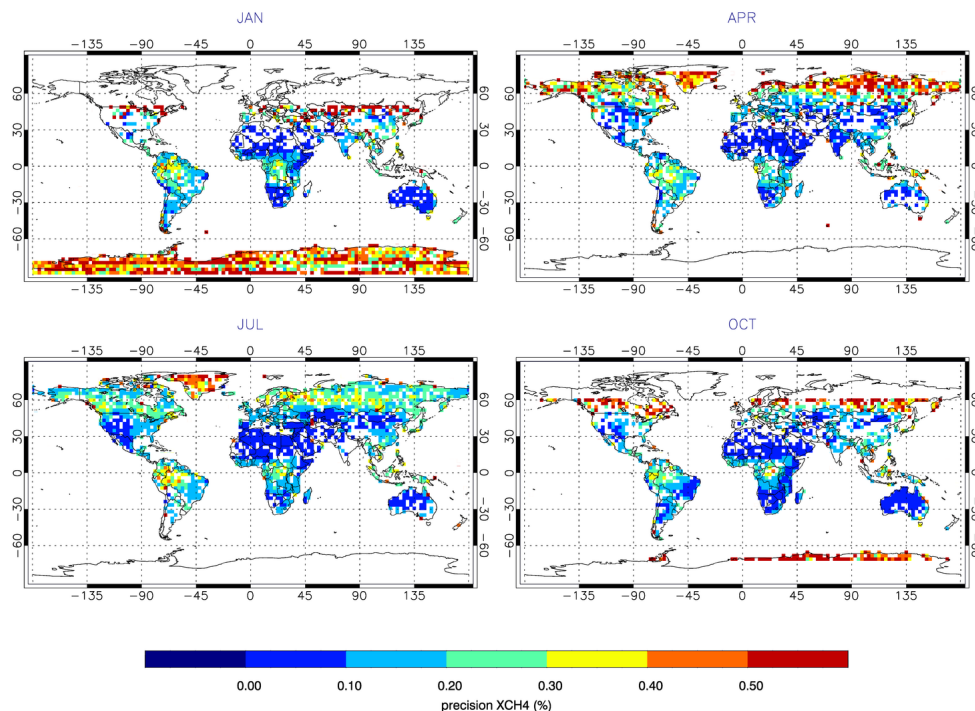rld map in Figure 16 shows the precision relative to the retrieved $X\mathrm{CH}_4$. Typically the precision is much better than the accuracy. The signal to noise ratio becomes only a limiting factor for scenarios with snow-covered ground and large SZA.

Figure 16: Relative precision of $X\mathrm{CH}_4$ due to the instrument noise for the a posteriori filtered dataset.

7.3.2 Instrument spectral response function

For the creation of the synthetic measurement spectra, the underlying line-by-line spectra have been convolved with a Gaussian spectral response function with $\mathrm{FWHM_{NIR}} = 0.5$ nm and $\mathrm{FWHM_{SWIR}} = 0.25$ nm. According to the SRD, the ISRF shall be known within 1% of its maximum (where the ISRF is greater than 1% of its maximum). Approximately, this is achieved by varying the FWHM by 1%. Table 8 and Figure 17 gives the results for simulated retrievals with an assumed error in the FWHM. The retrieval appears to be more sensitive to the accuracy of the ISRF in the SWIR band. From Figure 17 it follows that for some cases (especially latitude bands 20-40 degrees north) the error can be quite significant, increasing the forward model error by up to 0.5% compared to the reference case. It is important to note that the error due to incorrect knowledge of the ISRF is a factor 2 larger than the budget reserved for it in the SRD [AD1]. Therefore we suggest that accuracte calibration of the ISRF should have high priority.
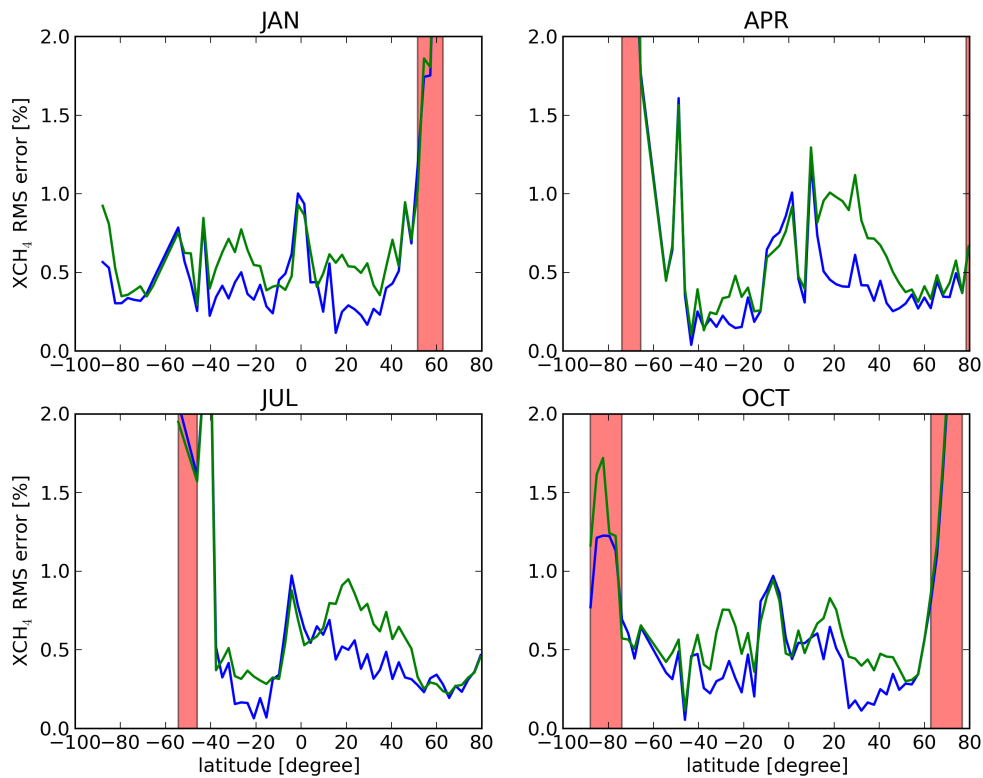
Figure 17: RMS error of XCH_4 for the simulation run with $\Delta FWHM_{NIR}$ = -1% and $\Delta FWHM_{SWIR}$ =+1% (green line), compared to the reference retrieval (blue line). The red areas indicate regions with high SZA that we plan to filter out.

Table 8: Influence of error in ISRF on the retrieval performance. Multiple simulation runs were performed; with FWHM increased and decreased. The results shown are for the run with poorest performance in terms of RMS error.

	converged	converged and filtered	RMS forward model error (filtered data)	CPU time per retrieval
$\Delta FWHM_{NIR}$ = -1% $\Delta FWHM_{SWIR}$ = 0%	95%	61%	0.47%	7.6 s
$\Delta FWHM_{NIR}$ = 0% $\Delta FWHM_{SWIR}$ = +1%	91%	60%	0.57%	7.6 s
$\Delta FWHM_{NIR}$ = -1% $\Delta FWHM_{SWIR}$ = +1%	91%	60%	0.58%	7.6 s

7.3.3   Position of the spectral channels

According to the SRD, the positions of the centre of spectral channels are known within 2 pm. For the ensemble of simulated spectra, a spectral shift of 2 pm has negligible effect on the error characteristics. The spectral stability is 1/20 of the spectral sampling distance, i.e. 10 pm for the NIR band and 5 pm for the SWIR band. Both a spectral shift (wavelength independent) and a spectral squeeze (1st order wavelength dependence) are investigated here, where the maximum wavelength shift is taken to be 10 pm and 5 pm, respectively, for the NIR and SWIR band.

Table 9: Influence of a constant error in position of spectral channels. Multiple simulation runs were performed; with $\Delta\lambda_\text{shift}$ positive and negative. The results shown are for the run with poorest performance. The results for the case a spectral shit is fitted is given in brackets.

	converged	converged and filtered	RMS forward model error (filtered data)	CPU time per retrieval
$\Delta\lambda_\text{shift,NIR} = -10\,\text{pm}$ $\Delta\lambda_\text{shift,SWIR} = 0\,\text{pm}$	78%	42%	0.53%	6.6 s
$\Delta\lambda_\text{shift,NIR} = 0\,\text{pm}$ $\Delta\lambda_\text{shift,SWIR} = +5\,\text{pm}$	95%	60%	0.47%	4.1 s
$\Delta\lambda_\text{shift,NIR} = -10\,\text{pm}$ $\Delta\lambda_\text{shift,SWIR} = +5\,\text{pm}$	77% (95%)	41% (61%)	0.55% (0.45)	5.8 s (7.6 s)

Table 10: Influence of a wavelength dependent error in position of spectral channel. Multiple simulation runs were performed; with $\Delta\lambda_\text{squeeze}$ positive and negative. The results shown are for the run with poorest performance. The results for the case a spectral squeeze is fitted is given in brackets.

	converged	converged and filtered	RMS forward model error (filtered data)	CPU time per retrieval
$\Delta\lambda_\text{squeeze,NIR} = -10\,\text{pm}$ $\Delta\lambda_\text{squeeze,NIR} = 0\,\text{pm}$	95%	60%	0.47%	7.6 s
$\Delta\lambda_\text{squeeze,NIR} = 0\,\text{pm}$ $\Delta\lambda_\text{squeeze,NIR} = -5\,\text{pm}$	95%	60%	0.49%	7.9 s
$\Delta\lambda_\text{squeeze,NIR} = -10\,\text{pm}$ $\Delta\lambda_\text{squeeze,NIR} = -5\,\text{pm}$	94% (95%)	60% (61%)	0.50% (0.46%)	7.7 s (9.4 s)

Spectral shift

The reference retrieval fits a spectral shift. To test this fitting option, the synthetic spectra were shifted with a constant wavelength shift:

$$\lambda'_k = \lambda_k + \Delta\lambda_\text{shift} \tag{55}$$

where λ_k is the real wavelength, λ'_k is the measured wavelength at pixel k. In Table 9 results are given for the case that a spectral shift is not fitted and is fitted (between brackets). When fitted, the performance is as good as for the reference retrieval, i.e. simulations without an error in the spectral position. This indicates that the spectral shift fitting is robust.

Spectral squeeze

Optionally a wavelength dependent shift can be fitted. To test this fitting option, the synthetic wavelength grid was "squeezed":

$$\lambda'_k = \lambda_k + \Delta\lambda_\text{squeeze}\frac{\lambda_k - \lambda_\text{mid}}{\lambda_\text{end} - \lambda_\text{mid}} \tag{56}$$

where λ_end and λ_mid are the wavelengths at the end and middle of the band, respectively.

Table 10 shows the performance of retrievals with this assumed error on the measured wavelength grid. It follows that a spectral squeeze has a small but significant impact on the retrieved $X\text{CH}_4$.

7.3.4 Radiometric offset (additive factor)

The effect of an unknown systematic offset in the Earth radiance is investigated. The offsets in the NIR and SWIR bands are independently varied with $\pm 0.1\%$ of the continuum. The algorithm (technically) allows fitting

an additive constant to the spectrum. This option is tested here. The results in Table 11 and Figures 18 and 19 show that the retrieval algorithm cannot correct for an error in the radfiometric offset, the performance is actually degraded when attempting to fit an offset. Because it is expected that the effect of noise will be larger when fitting an offset, the relative precision is shown in Figure 20. The noise contribution typically increases with 0.2% when fitting a radiometric offset.
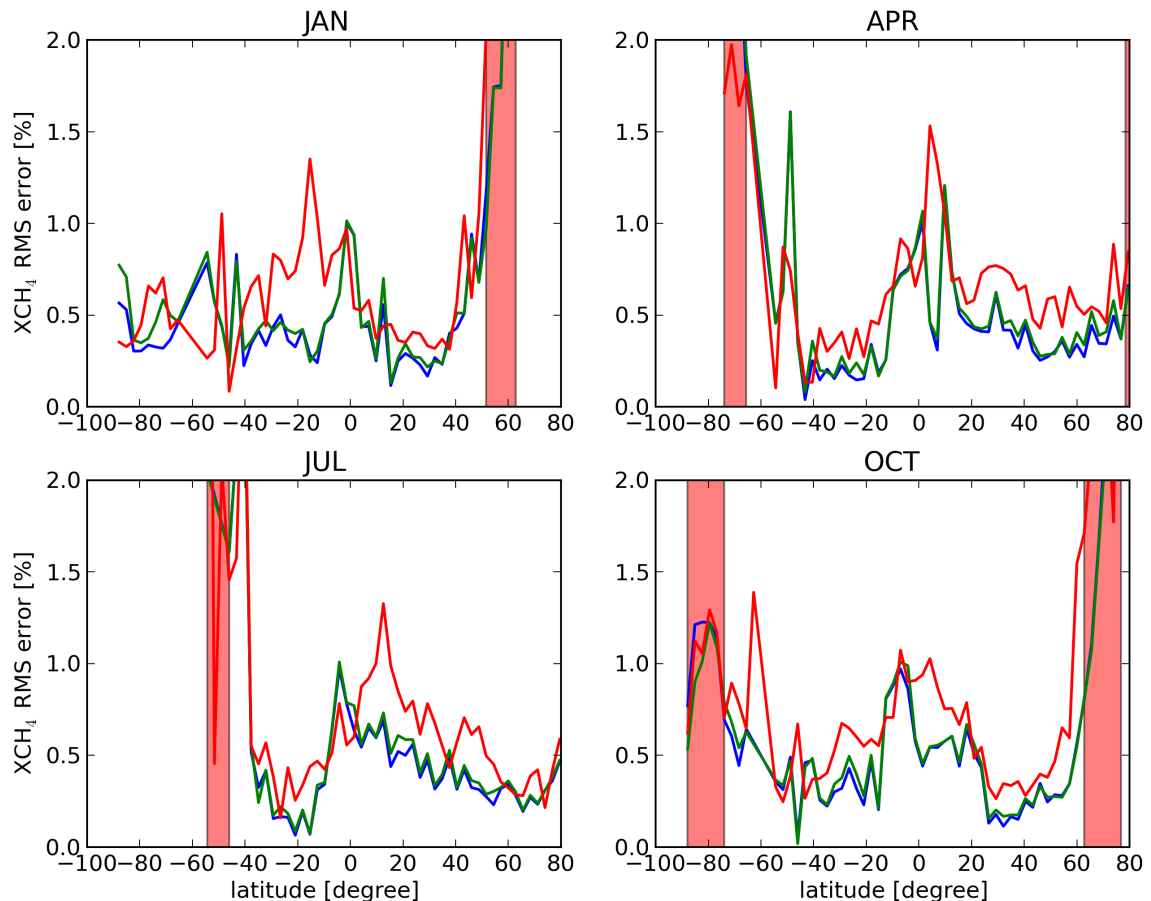
Figure 18: RMS error of XCH_4 retrieval per latitude bin for reference retrieval (blue), offsetted by 0.1% of the continuum but not fitted (green), and offsetted plus fitted (red). The red areas indicate regions with high SZA that we plan to filter out.

7.3.5 Radiometric gain (multiplicative factor)

The absolute radiometric accuracy of the measurement of the Earth spectral radiance shall be better than 2%, see SRD. To investigate the effect of such an error, the synthetic spectra were mutlitplied with a scaling factor A. Table 12 shows that there is negligible effect of an error of 2% in radiometric gain. This error is largely compensated by the retrieved surface albedo.

7.3.6 Combined errors and fitting options

Although the performance of optional fitting parameters have been tested here, one should remain cautious of fitting too many parameters. The information content in the observed spectra will limit the allowed number and choice of fitting parameters. For example, simulated retrievals where both an radiometric offset and a spectral squeeze are fitted only have a convergence rate of less than 30%. Real observations are needed to determine the necessity and possibility of fitting certain parameters.
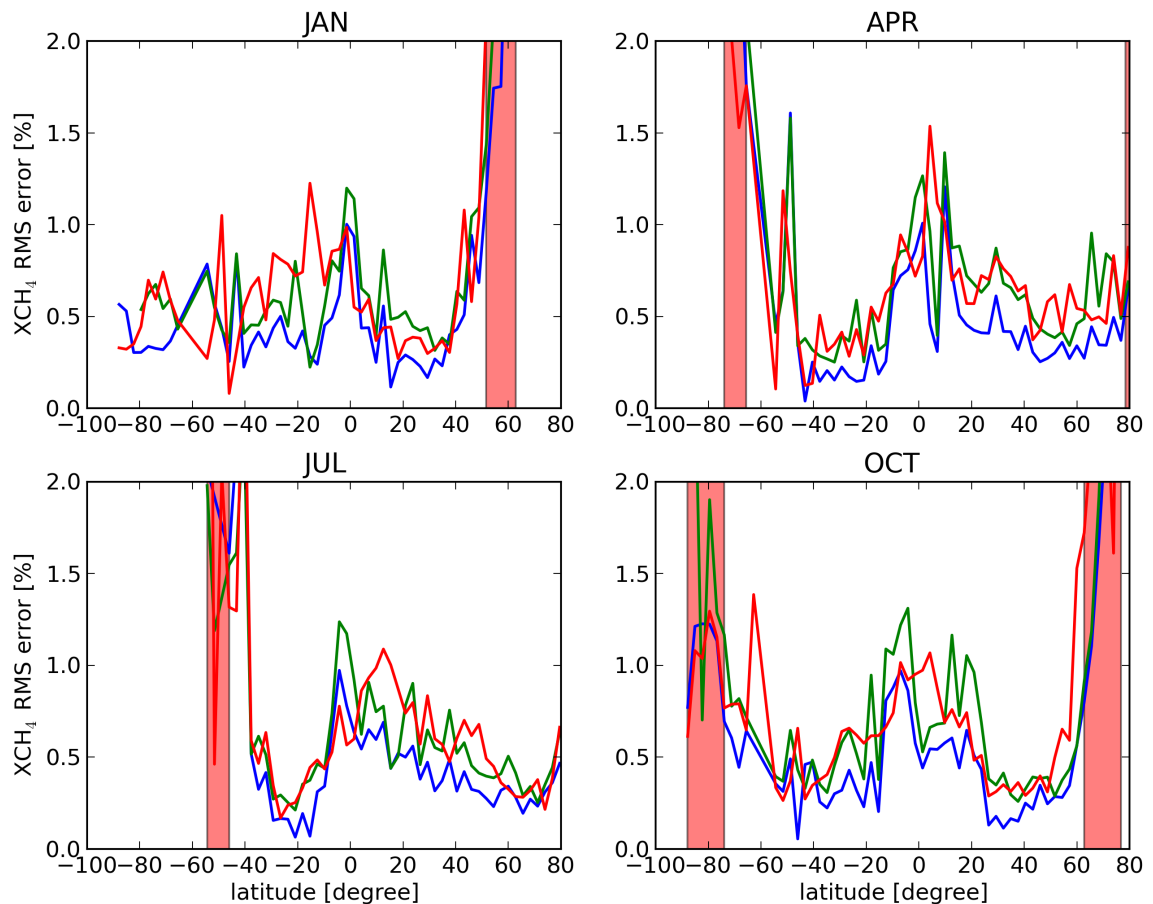
Figure 19: Same as Figure 18 but for an offset of 0.5%.

Table 11: Influence of a radiometric offset. Multiple simulation runs were performed; with positive and negative offset. The results shown are for the run with poorest performance. The results for the case an offset is fitted is given in brackets.

	converged	converged and filtered	RMS forward model error (filtered data)	CPU time per retrieval
$offset_{NIR}$ = 0.1% $offset_{SWIR}$ = 0%	91%	58%	0.47%	7.6 s
$offset_{NIR}$ = 0% $offset_{SWIR}$ = -0.1%	94%	63%	0.47%	7.7 s
$offset_{NIR}$ = 0.1% $offset_{SWIR}$ = -0.1%	90% (82%)	60% (56%)	0.49% (0.65%)	7.7 s (7.7 s)

Table 13 and Figure 21 show the results for the baseline inversion as described in Sec. 1 but with assumed instrument errors in both NIR and SWIR band for the synthetic spectra: 1% error in ISRF, radiometric offset error of 0.1% of the continuum, error in radiometric gain of 2%, spectral shift of 2 pm, spectral squeeze of 2 pm (at the ends of spectral bands). This gives an estimate of the total effect of the instrument errors considered here. The XCH_4 error due to an error in the ISRF appears to be the dominating error.
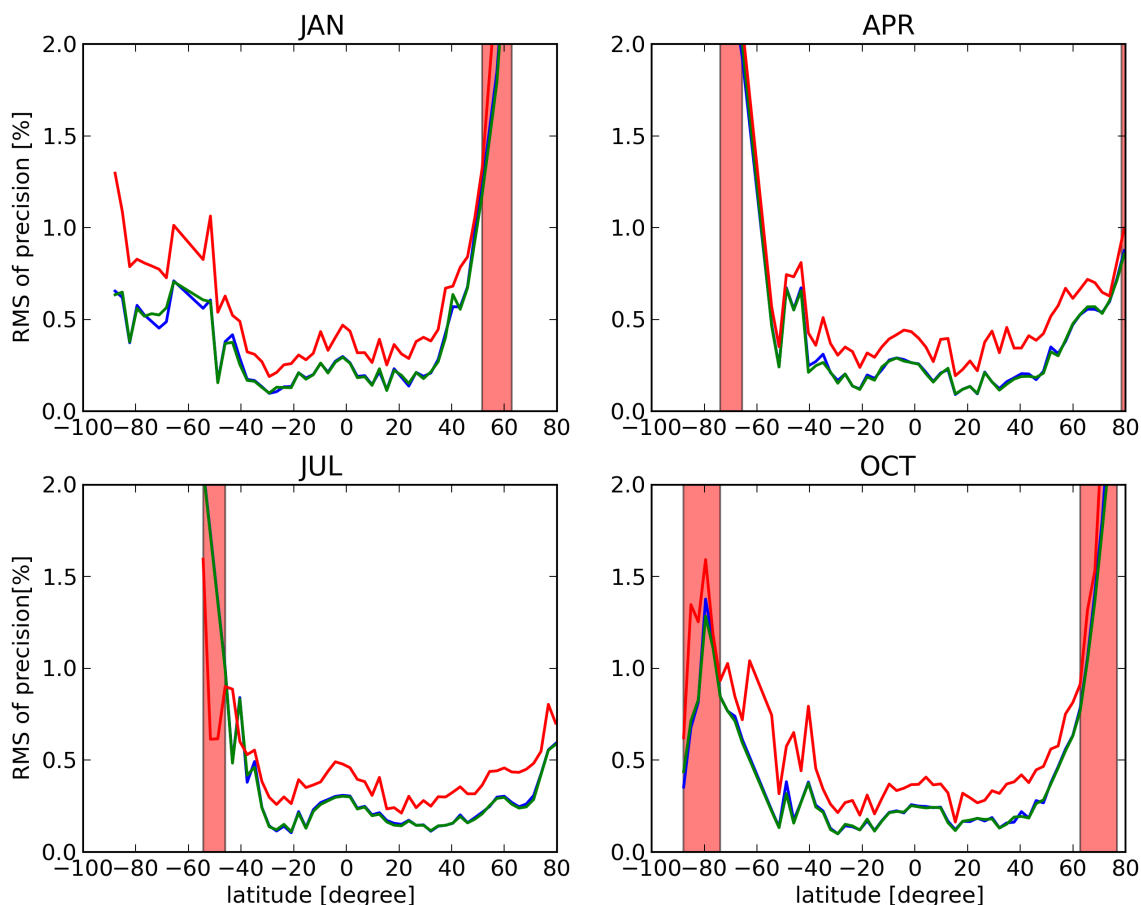
**Figure 20**: RMS of relative precision of $X\mathrm{CH}_4$ retrievals per latitude bin for reference retrieval (blue), offsetted (by 0.1% of the continuum) but not fitted (green), and offsetted plus fitted (red). The red areas indicate regions with high SZA that we plan to filter out.

Table 12: Influence of an error in radiometric gain. Multiple simulation runs were performed; with multiplicative factor smaller and greater than 1. The results shown are for the run with poorest performance.

	converged	converged and filtered	RMS forward model error (filtered data)	CPU time per retrieval
$A_{\mathrm{NIR}} = 1.02$ $A_{\mathrm{SWIR}} = 1.00$	95%	61%	0.46%	7.6 s
$A_{\mathrm{NIR}} = 1.00$ $A_{\mathrm{SWIR}} = 1.02$	95%	60%	0.46%	7.6 s
$A_{\mathrm{NIR}} = 1.02$ $A_{\mathrm{SWIR}} = 1.02$	95%	61%	0.47%	7.6 s

7.4 Filtering for clouds / cirrus

Overall, the S5P methane algorithm works satisfactory. However, the limited number of cases where the error is larger than 1% corresponds mostly to tropical regions which are very important for methane source/sink inversions. These scenes are difficult because of the combination of low surface albedo and high cirrus load. For actual S5P retrievals it may be necessary to more strictly filter for cirrus than has been done in our synthetic

Table 13: Influence of combined instrument errors on retrieval performance. Retrieval settings are the same as for the reference retrieval.

	converged	converged and filtered	RMS error without noise (filtered data)	RMS of retrieval noise (filtered data)	CPU time per retrieval
reference	95%	61%	0.45%	0.37%	7.6 s
instrument errors	83%	56%	0.64%	0.36%	7.8 s
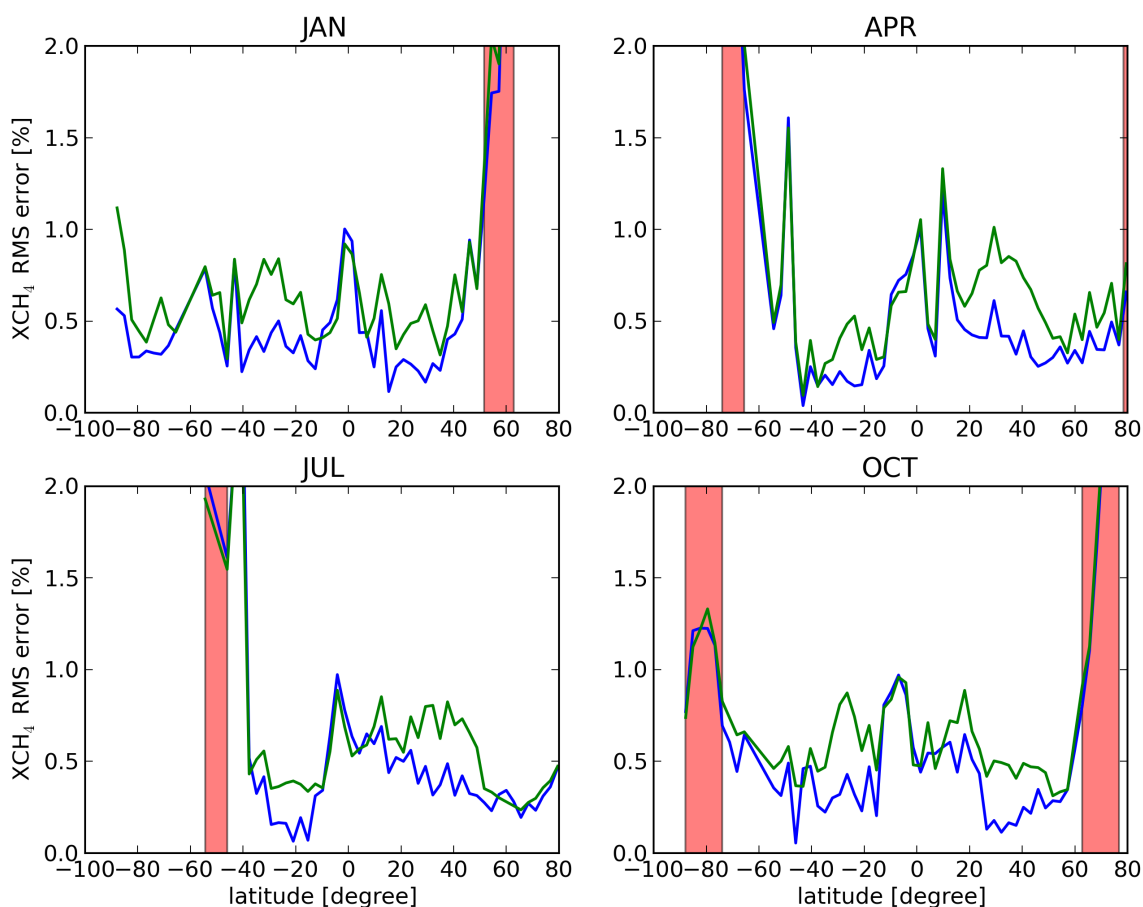
Figure 21: RMS error of XCH_4 when all instrument errors considered here are applied to the synthetic spectra (green line), compared to reference retrieval (blue line). The retrieval settings are the same for both simulation runs. The red areas indicate regions with high SZA that we plan to filter out.

retrievals, where we include cirrus with an optical thickness 0.3. As described in section 5 we will perform an (additional) cirrus filtering based on the difference in H_2O columns $[H_2O]_{weak}$ and $[H_2O]_{strong}$, and CH_4 columns $[CH_4]_{weak}$ and $[CH_4]_{strong}$, retrieved from weak and strong absorption bands, respectively. Here, the weak absorption band is chosen as 2310-2315 nm for both H_2O and CH_4, and the strong absorption bands are 2375-2380 nm for H_2O and 2363-2373 nm for CH_4. We found that a threshold value of 22% for H_2O ((weak-strong)/strong x100) and 6% for CH_4 is appropriate to filter out the cases with large (>1%) underestimation of the methane column caused by cirrus over a dark surface. The resulting methane errors

are shown in Figure 22 (world maps) and Figure 23 (cumulative distribution. From Figure 22 it can be seen that the cases with large underestimation of methane are effectively filtered out. From Figure 23 we see that the filter based on H_2O retrievals works better as stand-alone filter (in addition to aerosol filter) than the filter based on CH_4, but both filters improve considerably on the aerosol filter only. Using all filters together still improves the performance slightly compared to the use of the H_2O filter.
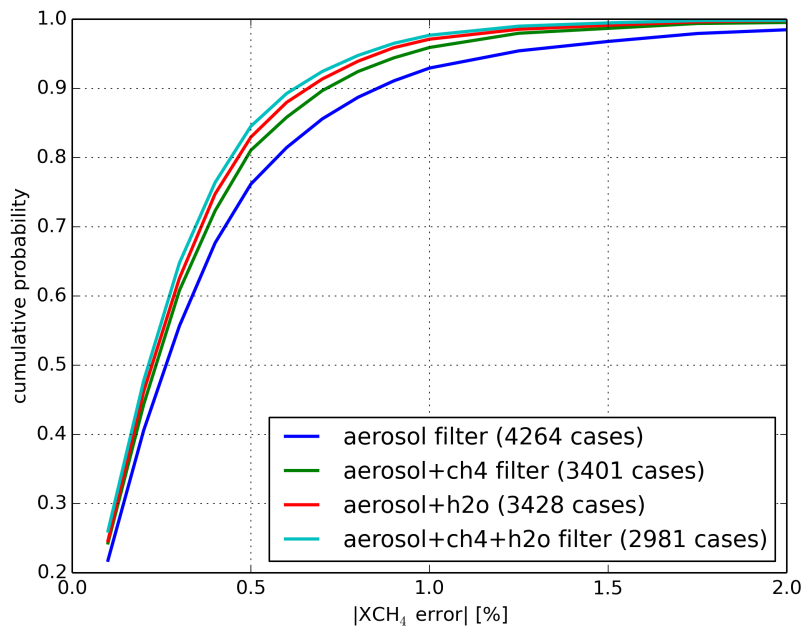
Figure 24 shows the difference in retrieved columns between weak and strong absorption bands for non-scattering atmosphere for CH_4 (solid) and H_2O (dotted) as a function of cloud fraction for a thick (COT=5) water cloud with cloud top at 2 km. It can be seen that, in contrast to cirrus clouds, water clouds cannot be filtered out to the level required as a maximum cloud fraction of 1-2% is allowed to keep the methane error below 0.25%-0.5%. With the thresholds defined above (22% for H_2O and 6% for CH_4) only cloud fractions > 0.15 will be filtered out. For these clouds the aerosol filter (defined in section 7.1) is more suited, and it will filter out cases with cloud fraction > 8% (see Figure 25). However, such cloud fractions still lead to unacceptable errors in the retrieved XCH_4 and hence this emphasizes the need for the VIIRS cloud imager, which is particularly strong in detecting small fractions (within a S5P pixel) of thick water clouds.
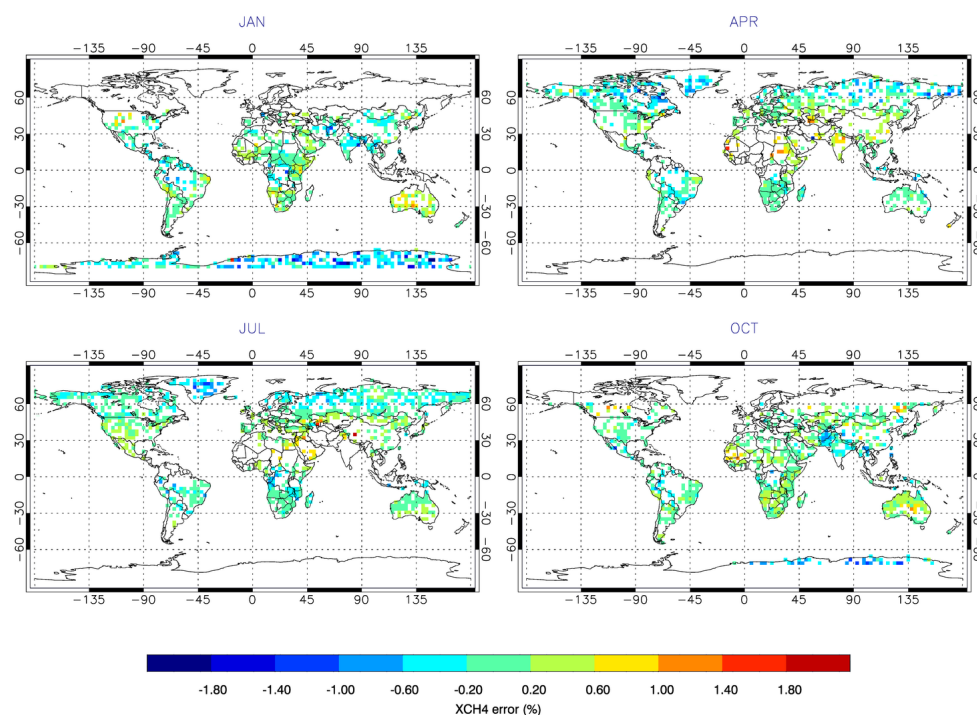
Figure 22: Forward model error of XCH_4 after applying the a posteriori filters and the a priori cloud filter based on non scattering H_2O and CH_4 retrievals.

7.5 Fluorescence

To test our approach for accounting for plant fluorescence we included fluorescence in the synthetic measurements for those scenes of the ensemble, which have a vegetated surface. To create the synthetic measurements we used a more detailed fluorescence model, where the spectral dependence by two co-added Gaussians (see [RD47, Eq. 1]), than the simplified model used in the retrieval. Figure 26 shows the RMS retrieval error on XCH_4 as a function of fluorescence emission for retrievals where fluorescence is not included and for retrievals with fluorescence included. If fluorescence is not included, the RMS retrieval error increases significantly form 0,7% to 0.9% with increasing fluorescence signal. On the other hand, if fluorescence is included in the retrieval (i.e. fitting $F_{s,755nm}^{surf}$ and s in Eq. 42 the RMS error is similar for different values of the fluorescence signal (there is a slight decrease in RMS error, probably as a result of compensating aerosol / fluorescence errors). So, the

Figure 23: Cumulative probability distribution of the absolute XCH$_4$ retrieval error for the reference retrieval that includes scattering of aerosols and cirrus for the baseline filter, baseline and an additional filter based on non scattering CH$_4$ retrievals, baseline and an additional filter based on non-scattering H$_2$O retrievals, and the baseline and both CH$_4$ and H$_2$O filters.
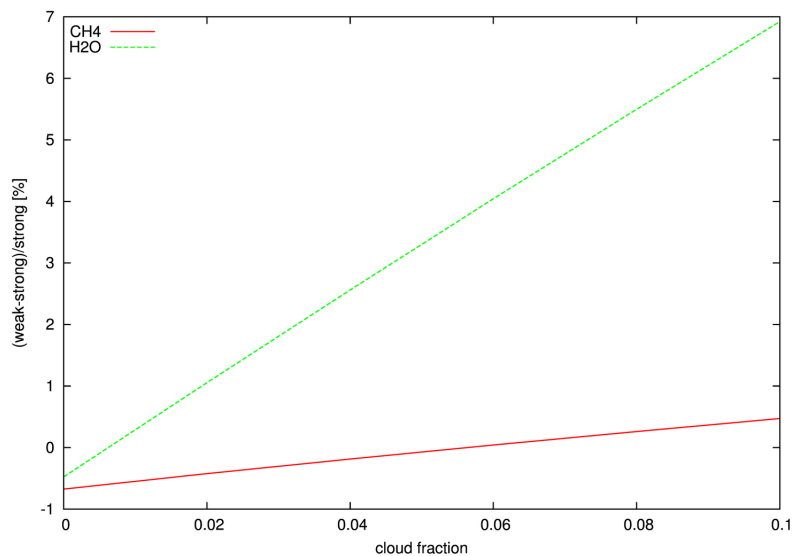
Figure 24: Difference in retrieved columns between weak and strong absorption bands for non-scattering atmosphere for CH$_4$ (solid) and H$_2$O (dotted). For the creation of synthetic measurements a cloud with optical thickness 5 was used with cloud top height = 2 km and cloud geometrical thickness = 1 km.

inclusion of fluorescence in the retrieval making use of Eq. 42 is sufficiently accurate for our purposes.
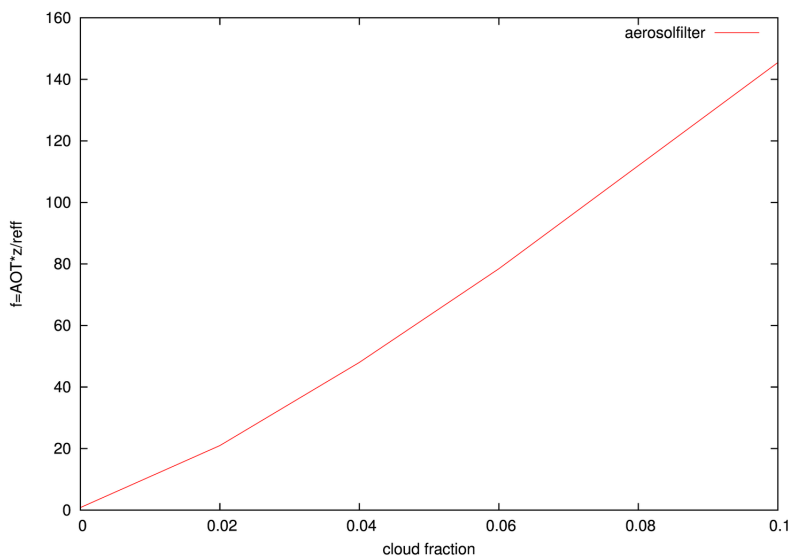
Figure 25: Aerosol filter f value versus cloud fraction. Cases with f>110 will be filtered out, which roughly corresponds to a cloud fraction of 0.08.

Figure 26: RMS $X\mathrm{CH}_4$ error as a function of fluorescence emission for retrievals with and without fluorescence included in the fit.

7.6 Summary and discussion of error analysis

Overall, the developed algorithm does well in correcting and filtering for the effect of aerosols and cirrus clouds on the retrieved $X\mathrm{CH}_4$. After filtering for cirrus contamination for the ensemble of synthetic measurements 85% of the retrievals yield an error on $X\mathrm{CH}_4$ that is less t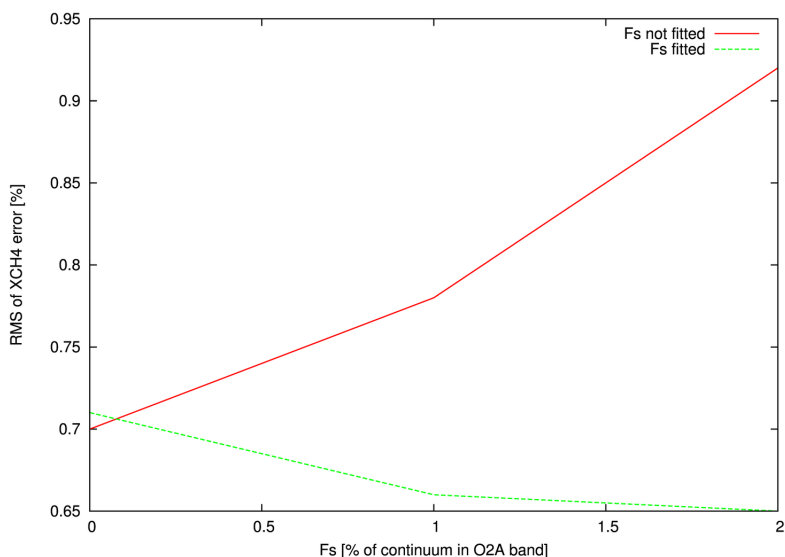han 0.5%. Apart from strict cirrus filtering, we have performed a bias correction of the $X\mathrm{CH}_4$ data (see Sect. 5.6), similar to what we did for GOSAT [RD29]. Such a bias correction further enhances the use of S5P $X\mathrm{CH}_4$ data for inverse modelling and other scientific applications.

Apart from forward model errors induced by aerosols, we also studied model errors due to errors in temperature, pressure, and water vapour profiles. Here, we found that fitting a constant shift in the temperature profile is an effective way to correct for errors in the temperature profile. Furthermore, we found that it is important that the surface pressure should be known within about 2 hPa in order to avoid the need to fit this parameter (which strongly correlates with aerosol).

Concerning instrument errors, we found that the most critical error source is an error in the ISRF in the SWIR band. If the FWHM of the ISRF in the SWIR has an error of 1%, this may cause errors as large as 0.5% on $X\mathrm{CH}_4$, which means that the requirement formulated in the SRD [RD63] is not strict enough. Therefore it is extremely important that the ISRF is well calibrated. Furthermore, it is important that the offset on the measured spectrum is small, as the measurement does not contain sufficient information to correct for such an error in the retrieval algorithm.

8 Validation

8.1 Ground based

8.1.1 The Total Carbon Column Observatory Network (TCCON)

In 2004 the TCCON network was founded in preparation for the validation of the OCO mission, the first dedicated CO_2 satellite mission to be launched. Since then the network has become the standard for validating satellite based column measurements of CO_2 and CH_4 [RD32, RD64]. TCCON is a network of inter-calibrated ground-based Fourier transform spectrometers that measure the absorption in the NIR/SWIR of direct sunlight by trace gas species such as CO_2, CH_4, CO, HDO, etc. These measurements are thus much less influenced by atmospheric scattering by cirrus and aerosols than satellite observations of backscattered/reflected sunlight. Also for S5P retrievals of XCH$_4$ the TCCON network will be the prime source of validation data. TCCON XCH$_4$ measurements have been calibrated and validated against the WMO-standard of in-situ measurements using dedicated aircraft campaigns of XCH$_4$ profiles and their resulting accuracy have been estimated to 0.4% (2σ value) [RD32]. Table 14 shows an overview of the existing and some expected future TCCON stations. An important limitation of the TCCON network for validation of satellite retrievals of greenhouse gas concentrations is the limited albedo range that is covered by the TCCON stations. Figure 27 shows the surface albedo range at 2300 nm for the different TCCON stations. It can be seen that surface albedos > 0.20 are not covered by the TCCON network except for the Caltech and Four Corners stations. However, the latter 2 stations may not be very well suited for validation purposes because of local sources (Caltech) or mountainous area (Four Corners). Globally, over 20% of the land surfaces have an albedo >0.2, up to 0.7. Therefore, there is a strong need for validation (TCCON) stations that cover higher surface albedos [RD65, RD28]. This is very important as these scenes pose a strong challenge for the XCH$_4$ retrieval algorithm because of the large sensitivity to aerosols. Also TCCON stations at the challenging very low albedo conditions are lacking to some degree. An interesting development in this respect is the development of somewhat cheaper spectrometers complementary to the TCCON high spectral resolution FTIRs [RD66, RD67]. Clearly, for these systems to be useful for S5P XCH$_4$ validation their accuracy needs to be high enough. But they offer the potential of deployment in the now poorly sampled areas including high (and low) albedo regions.

Finally, it is important to note that TCCON data is currently guaranteed to be made available within one year after measurement. Only for a few stations earlier delivery is guaranteed. It should be realised, however, that ~one year of data is needed to assess the quality of the satellite data. If the data is only delivered after 1 year, this would mean that we are two years into the mission before any statement can be given about the quality of the data. This is clearly not adequate. Therefore we recommend that for an adequate and timely validation of S5P CH$_4$, TCCON data should be made available on shorter timescales, e.g. ~3 months.

Table 14: Overview of TCCON stations (information from 2013; note that the Four Corners instrument has been moved to Brasil)

station	latitude [degree]	longitude [degree]	height [m]	period	comment
Bialystok	53.23	23.025	180	since 1 Mar. 2009	
Bremen	53.1037	8.84952	30	since 6 Jan. 2005	
Darwin	-12.4245	130.892	30	since 28 Aug. 2005	
Garmisch	47.476	11.063	743	since 16 July 2007	
Karlsruhe	49.1	8.438	111	since 19 Apr. 2010	
Lamont	36.604	-97.486	320	since 6 July 2008	
Lauder	-45.038	169.684	370	since 29 June 2004	
Orléans	47.97	2.113	130	since 29 Aug. 2009	
Park Falls	45.945	-90.273	442	since 26 May 2004	
Sodankylä	67.368	26.633	179	since 6 Feb. 2009	
Tsukuba	36.0513	140.122	31	since 25 Dec. 2008	
Wollongong	-34.406	150.879	30	since 26 June 2008	

Table 14 – *Continued from previous page*

station	latitude [degree]	longit-ude [degree]	height [m]	period	comment
Arrival Heights	-77.83	166.663	250	-	too southerly
Eureka	80.05	-86.42	610	since 24 July 2010	too northerly
Ny Ålesund	78.9232	11.923	20	since 14 Mar. 2005	too northerly
Lzaňa	28.3	-16.5	2370	since 18 May 2007	too high
Zugspitze	47.42	10.98	2960	-	too high
Ascension Island	-7.9165	-14.3325	10	since 22 May 2012	new
Caltech	34.1362	-118.127	230	since July 2012	new
Four Corners	36.7975	-108.48	1643	since Mar. 2011	new, to be moved temporarlly to Manaus
Reunion Island	-20.9014	55.4847	87	since 6 Oct. 2011	new
Saga	33.241	130.288	7	since 1 June 2011	new
Dryden	34.95	-117.83	692	future	from JPL
Manaus	-3.1	-60.02	36	future	from Four Corners
Rikubetsu	43.4567	143.766	380	future	
Indianapolis	39.8614	-86.0036	279	23 Aug. - 9 Dec. 2012	from JPL
Jena	50.91	11.57	211.6	-	moved to Ascension Island
JPL	34.202	-118.175	390	1 July 2007-22 June 2008 8 Dec. 2011-23 July 2012 since 18 Jan. 2013	from Lamount to be moved to Dryden
Yekaterinburg	57.0383	59.545	300	-	no reliable retrieval data yet

8.1.2   In Situ Measurements

In situ measurements of the full vertical CH_4 profile will be extremely useful as they allow the column averaging kernel to be applied and hence the retrieved XCH_4 from S5P can be compared with truly the same quantities. TCCON only delivers the column integrated values and hence do not allow the averaging kernel to be applied, which leads to a remaining uncertainty in the comparison. Vertical profiles can be obtained by aircrafts as is done for calibrating the TCCON network, but they do not sample the full total column. In this respect a very interesting new development is provided by the AirCore initiative [RD68]. The AirCore is an innovative atmospheric sampling system that consists of a long tubing, usually in the shape of a coil, that can sample the surrounding atmosphere and preserve a profile of the trace gas of interest. The narrow diameter and long length are designed to minimize the diffusive mixing occuring inside the tubing between sampling and analysis. The AirCore, invented and patented by Pieter Tans (the head of the Carbon Cycle Group at NOAA/ESRL), can in principle provide measurement precisions equal or even better than the in-situ flask sampling for CO_2 and CH_4 (and also CO). A clear advantage of AirCore over aircraft measurements is the lower cost and the fact that it can in principle sample the profile across the entire column. The most obvious application of AirCore would be as an alternative to the aircraft spirals that are undertaken for the absolute calibration of TCCON to the in-situ standard. Not only does it lower the cost it also allows for measurements higher up in the atmosphere where now climatology has to be used to extrapolate the aircraft measurements and which poses the largest error source to this absolute TCCON calibration particularly for CH_4 [RD32]. Another possible application of AirCore would be to use it in areas where there are no TCCON validation sites.
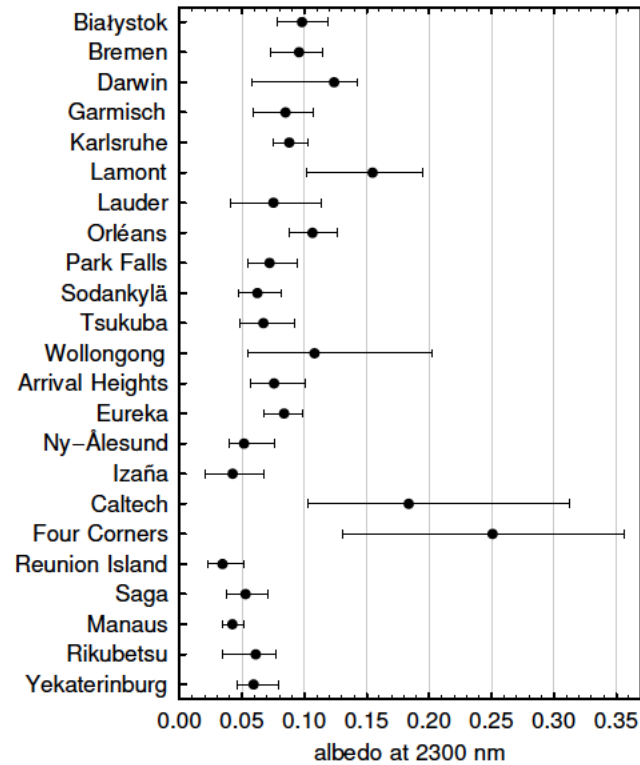
Figure 27: Range of the central 80% of the land albedo values in an area of about $500 \times 500\,\text{km}^2$ around each TCCON station, except Ascension Island, for which no land data is available. A dot indicates the median value. Sea values are excluded, but they may contaminate coastal land.

8.2 Satellite Intercomparison

GOSAT has been launched in 2009 and provides column integrated $X\text{CH}_4$ with sensitivity to the ground making use of the 1.6 µm channel. GOSAT can make use of both the proxy method as well as a Full Physics method such as described here (e.g. [RD16]). The RemoTeC algorithm, on which the S5P algorithm is based, is continuously being applied to the global GOSAT level-1 data set. Therefore, comparisons with GOSAT will be very useful. However, it is not clear if GOSAT is still active in 2016, when the S5P instrument will be launched. The GOSAT-2 instrument is planned for launch in 2018 so may be used for S5P validation/comparison purposes later in the mission. Likely, GOSAT-2 will also have a spectral band around 2300 nm, like S5P, and will hence be even more interesting to validate/compare to S5P.
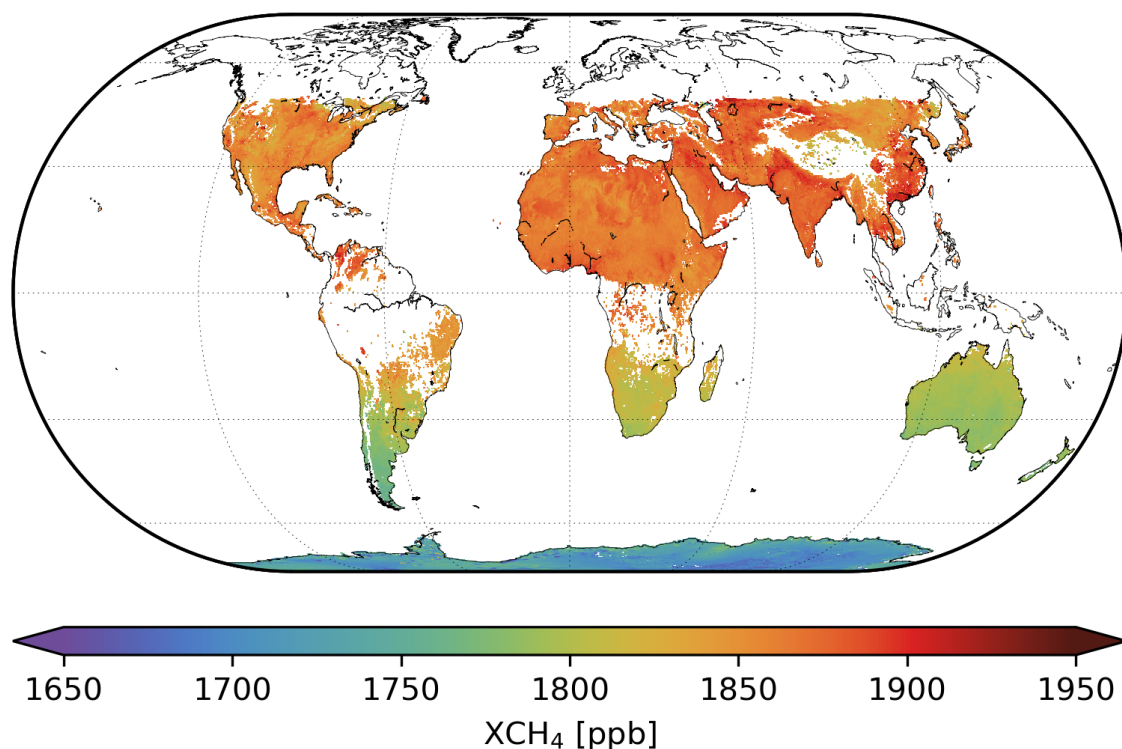
Figure 28: CH4 total column mixing ratio bias corrected of TROPOMI averaged from November 28th 2018 to January 16th 2019

9   Examples of TROPOMI CH$_4$ data

After the successful launch of TROPOMI on October 13th, 2017 as the single payload of ESA's Sentinel-5 Precursor (S-5P) satellite, first calibrated SWIR radiance data were received at November 9th, 2017. The data quality was already sufficient to process the CH$_4$ total column product with remarkable accuracy, as presented in [RD69]. This section shows first examples of the operational TROPOMI CH$_4$ product and summarizes preliminary data validation results.

Figure 28 shows first results of global CH$_4$ observations of TROPOMI averaged from November 28th 2018 to January 16th 2019. For the retrieval, we process only clear-sky observations with a solar zenith angle (SZA) < 70°, a viewing zenith angle (VZA) < 60° and a surface albedo > 0.02. Here only data are used with a quality assurance value (qa_value) > 0.5. The data selection approach is summarized in Section 6.4, and the specifics on the recommendations for data usage and quality assurance are provided in the Methane Product Readme File [RD70].

A preliminary validation has been performed by comparing the TROPOMI CH$_4$ operational data product with independent ground based CH$_4$ measurements from several stations from the TCCON network (see Sect. 8.1). We select TROPOMI measurements from the same day as the TCCON measurements within a radius of 300 km around each station, and we compare the daily average data of CH$_4$. Figure 29 shows an example of a time series of the validation over Pasadena (U.S.) and Orleans (France). By comparing data over 12 different stations, we find an agreement between TROPOMI CH$_4$ and TCCON of -12 ppb, with a station-to-station variability (i.e. standard deviation of the mean bias for all stations) of 11.5 ppb. If the radius is reduced to 50 km, the bias is -13.6 ppb, comparable to the one obtained with the 300 km radius, but the number of co-located measurements is reduced by 60%. The agreement between TROPOMI CH$_4$ corrected for the albedo dependency (see Sect. 5.6) and TCCON (for a collocation radius of 300 km) is of -4.3 ppb, with a station-to-station variability of 7.4 ppb, as shown in Figure 30. The comparison results show that the quality of both the uncorrected and bias-corrected TROPOMI CH$_4$ product is such that they both largely comply with the mission requirements with significantly improved data quality of the bias-corrected product.
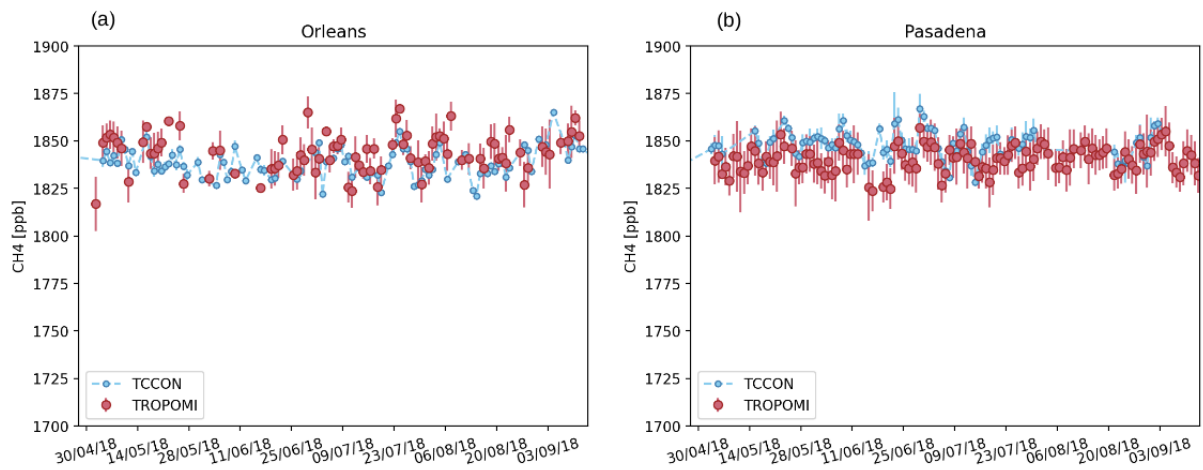
Figure 29: Time series of daily mean XCH$_4$ measured by TROPOMI (red dots) and by TCCON stations (red dots) in (a) Orleans, France (left) and (b) Pasadena, U.S. (right).
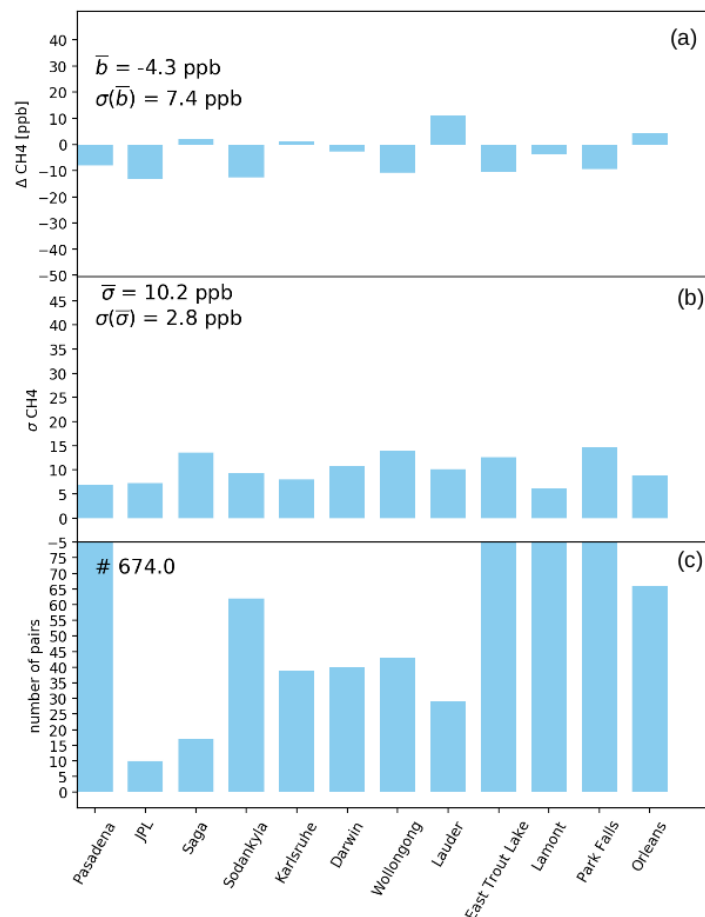
Figure 30: (a) Station mean bias (TROPOMI-TCCON) between co-located daily mean bias-corrected XCH$_4$ from TROPOMI and TCCON with a global bias of -4.3 ppb and a stattion-to-station bias variation of 7.4 ppb , (b) the station standard deviation of the bias with a station-to-station variation of 10.2 ppb and (c) the number of coincident daily mean pairs. Data used for this comparison ranges from May to September 2018.

10 Conclusions

This document describes the algorithm for methane retrieval from the S5P instrument. The heritage of the algorithm lies in earlier algorithm developments for retrieval of CO_2 columns from OCO (launch failed February 2009) and CO_2 and CH_4 from GOSAT (successfully launched January 2009), described by Butz et al. 2009 [RD20]. Tests of the retrieval algorithm have been performed on synthetic GOSAT data [RD9], and real GOSAT data [RD23, RD16].

In order to account for the effect of aerosols and cirrus, the developed algorithm retrieves the methane column simultaneously with the aerosol/cirrus amount (column integrated particle number concentration), a parameter related to the particle size distribution, and a parameter describing the height distribution. Here, the particle size distribution is described by a power-law function [RD39], which only has two free parameters (related to amount and size). The choice of aerosol/cirrus parameters reflects the information content of the measurements as close as possible. The retrieval algorithm uses the level 1b reflectance measurements in the Short Wave Infra-Red (SWIR) band and additionally in the NIR band between 757-774 nm (O_2 A band). Additional fit parameters are the surface albedo and its 1st order spectral dependence in the two bands, and the total columns of carbon-monoxide and water vapor, respectively. In order to obtain a proper characterization of the retrieved methane column, it is important to first retrieve a vertical profile (layer averaged number density in different layers of the model atmosphere) and use this retrieved vertical profile to calculate the vertical column. Here, we choose to provide the vertical column as a product, and not the full profile, because the Degree of Freedom for Signal (DFS) of the retrieved methane profile is about 1. The inversion is performed using Phillips-Tikhonov regularization in combination with a reduced step size Gauss-Newton iteration scheme.

The forward model of the retrieval algorithm uses online radiative transfer calculations, fully including multiple scattering. Here, the radiative transfer model developed Landgraf et al. [RD43], and Hasekamp et al. 2002, 2005 [RD71, RD44] is being used. This model uses the Gauss-Seidel iterative method to solve the radiative transfer equation in a plane-parallel, vertically inhomogeneous atmosphere. To avoid time consuming line-by-line calculations we employ the linear-k method developed by Hasekamp and Butz 2008 [RD27]. Absorption cross sections of the relevant atmospheric trace gases are tabulated in a lookup table as function of pressure and temperature. Optical properties of aerosols are also calculated from lookup tables as described by Dubovik 2006 [RD41]. The linear k-binning method in combination with other speed optimizations allow us to perform the methane retrievals with online RT calculations within ~7-10 seconds for a single retrieval. This makes the algorithm feasible for operational S5P data processing.

To test the developed algorithm we generated an ensemble of simulated measurements that covers the range of scenes that will be likely encountered by the S5P instrument. This includes a realistic and detailed description of aerosol and cirrus properties, in combination with a surface albedo. Aerosol, cirrus and surface properties are taken from model (ECHAM5-HAM) and satellite measurements (MODIS, CALIOP/CALIPSO). Overall, the developed algorithm does well in correcting for the effect of aerosols and cirrus on the retrieved XCH_4. For the ensemble of synthetic measurements 85% of the cases has an XCH_4 error < 0.5%. To achieve this a strict filtering for cirrus clouds is needed which can be performed based on non-scattering retrievals of CH_4 and H_2O from weak and strong absorption bands in the SWIR. These retrievals will be provided by the CO algorithm SICOR [RD54]. It should be noted that the filters based on S5P itself cannot replace the VIIRS cloud mask for water clouds. Apart from a strict filtering, we have performed a bias correction of the XCH_4 data (see Sect. 5.6), similar to what we did for GOSAT [RD28]. Such a bias correction further enhances the use of S5P XCH_4 data for inverse modelling and other scientific applications.

Apart from forward model errors induced by aerosols, we also studied model errors due to errors in temperature, pressure, and water vapour profiles. Here, we found that fitting a constant shift in the temperature profile is an effective way to correct for errors in the temperature profile. Furthermore, we found that it is important that the surface pressure should be known within about 2 hPa in order to avoid the need to fit this parameter (which strongly correlates with aerosol).

Concerning instrument errors, we found that the most critical error source is an error in the ISRF in the SWIR band. If the FWHM of the ISRF in the SWIR has an error of 1%, this may cause errors as large as 0.5% on XCH_4. Furthermore, it is important that the offset on the measured spectrum is small, as the measurement does not contain sufficient information to correct for such an error in the retrieval algorithm.

Based on the analysis of the first CH_4 measurements during the first months of the Sentinel 5 Precursor commissioning phase [RD69] and on the validation of the first months of data from the offline operational data product (Sect. 9), we conclude that the mission provides a reliable high-quality CH_4 data product with daily global coverage. Preliminary validations with ground based TCCON observations indicated a CH_4 data quality that already complaints with the mission requirements.

A   Description of Prototype Software

Documentation on the prototype software can be found at:
`ftp://ftp.sron.nl/pub/pub/RemoTeC/TROPOMI/html/index.html`
`ftp://ftp.sron.nl/pub/pub/RemoTeC/TROPOMI/refman.pdf`.

B Appendix B: Description of test cases

The simulated measurements are spectra of backscattered sunlight including noise based on the TROPOMI requirements as described in the TROPOMI SRD. For the O_2 A band in the TROPOMI NIR channel and the TROPOMI SWIR band signal-to-noise ratios of 500 and 120 in the continuum, respectively, have been adopted. Within the O_2 A band, the noise scales with the square root of the intensity, implying shot noise is the dominant noise contribution. For the TROPOMI SWIR band, a noise floor has been taken into account in addition to shot noise.

The forward model used to calculate the simulated measurements is the same as that in the retrieval method except for the treatment of aerosols and cirrus clouds which is highly simplified in the retrieval forward model in comparison with the true variability of aerosols and cirrus clouds in the atmosphere. For the simulation of measurements, a refined model is used that takes into account seven different aerosol modes, cirrus clouds, and arbitrary height distributions of the scatterers.

The aerosol input parameters for the generation of the ensemble simulations are derived from a run of the ECHAM5-HAM global aerosol model [RD40] for the year 2015 according to the A1B scenario defined by the Intergovernmental Panel on Climate Change. ECHAM5-HAM provides estimates of aerosol particle number concentrations and size distribution parameters for seven modes of a lognormal size distribution in 19 atmospheric layers between the ground and 10 hPa pressure on a $3° \times 3°$ latitude by longitude grid. Each mode is a composite of five aerosol chemical types, i.e. sulfate, black carbon, organic matter, sea salt, and mineral dust. For each mode and considered spectral window, we calculate an average refractive index weighted by the relative mass contribution of the individual aerosol chemical type. Given size distribution and mode wise refractive index, the aerosol scattering and absorption OT and the aerosol scattering phase matrix are computed for the 19 ECHAM5-HAM layers individually and then interpolated to the simulation forward model height grid. The AOT from the ECHAM5-HAM model is scaled to MODIS observations (available at `http://modis-atmos.gsfc.nasa.gov/index.html`) where these are available. Figure 31 shows the distribution of AOT in the synthetic ensemble for the different seasons. Only data over land and with solar zenith angles below 70° are considered.

For cirrus clouds, we use the model developed by Hess et al. 1994 and 1998 [RD72, RD60] to calculate the phase matrix and the scattering and absorption OT of hexagonal ice crystals from a total column number density of cirrus. The ice crystals are assumed to be randomly oriented in space and to exhibit columnar shape. With a being the length of the side of the hexagon and c being the length of the column, cirrus optical properties are computed for eight crystal size pairs (a, c) between (1.4 μm, 3.5 μm) and (110 μm, 1300 μm) essentially following table 1 in Hess et al. 1994 [RD72]. Since model calculations for perfect hexagonal ice crystals exhibit unrealistically pronounced halos of the phase matrix at 22° and 44° scattering angle, we apply a smoothing correction suggested by Hess et al. 1998 [RD60]. Given the database of crystal size pairs (a, c), we aggregate cirrus optical properties according to a power law size distribution in analogy to the study by Heymsfield et al. 1984 [RD73].

The total COT and the height and thickness of the cirrus layer are derived from the CALIOP/CALIPSO monthly mean data of the year 2007 [RD74]. We considered the level 2 cloud product data at 5 km resolution, provided by the ICARE Data and Services Center, `http://www.icare.univ-lille.fr`. Only cases with COT < 0.4 were considered for averaging and for calculation of the synthetic spectra, because scenes with higher OT will be identified as cloudy by the cloud screening algorithm of the VIIRS instrument. Figure 32 shows the global distribution of COT derived from CALIOP/CALIPSO data.

The surface albedo in the TROPOMI SWIR band is based on SCIAMACHY retrievals by Schrijver et al. 2009 [RD75]. Where no SCIAMACHY data are available, the MODIS LAND product is used, after scaling the measured albedo in band 7 (2.105-2.155 μm) by a factor of 0.7. This factor has been derived by estimating the ratio of the 2.3 μm/2.1 μm surface albedo for different vegetation types in the ASTER data base. The global distribution of the surface albedo used in the ensemble is shown in Figure 33. The albedo in the TROPOMI NIR band is taken from MERIS data, publicly available at `www.temis.nl/data/meris.html` [RD76].

The atmospheric conditions (pressure, temperature, humidity) are derived from the ECMWF (European Centre for Medium-Range Weather Forecasts) ERA-Interim analysis provided 6-hourly on a $1.5° \times 1.5°$ latitude $\times$ longitude grid (available at `http://data-portal.ecmwf.int/data/d/interimdaily/`). The amount of CH_4 and CO is taken from the TM4 model [RD7]. Finally, atmospheric input, surface albedo, and cirrus and aerosol optical properties are combined to create a global ensemble representative for January, April, July, and October. One simulated measurement is created for each $3° \times 3°$ gridbox.
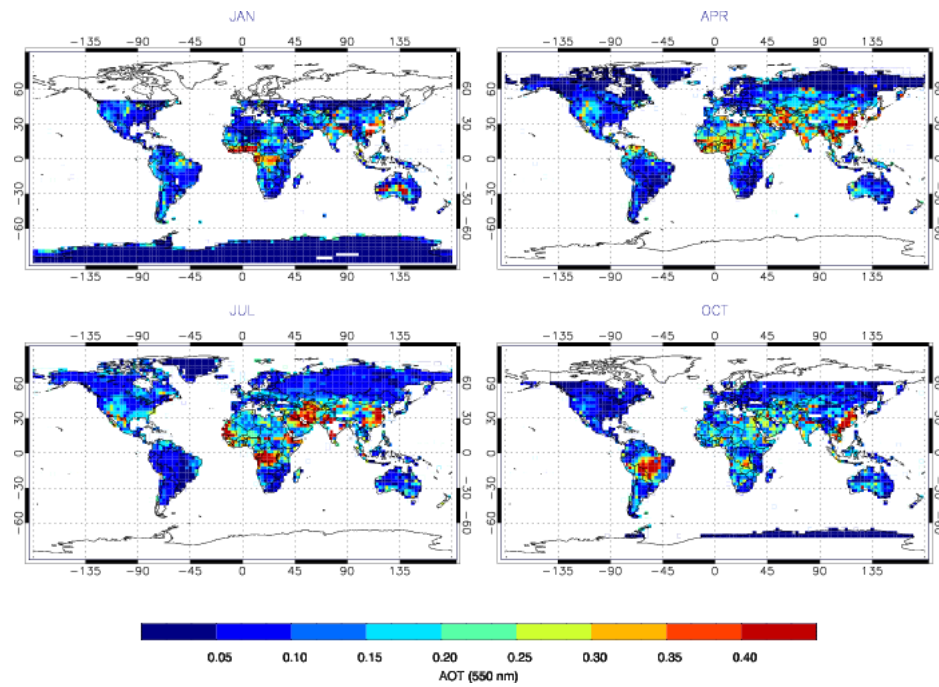
Figure 31: Global distribution of Aerosol Optical Thickness (AOT) adopted for the synthetic ensemble. January (top left), April (top right), July (bottom left), and October (bottom right).
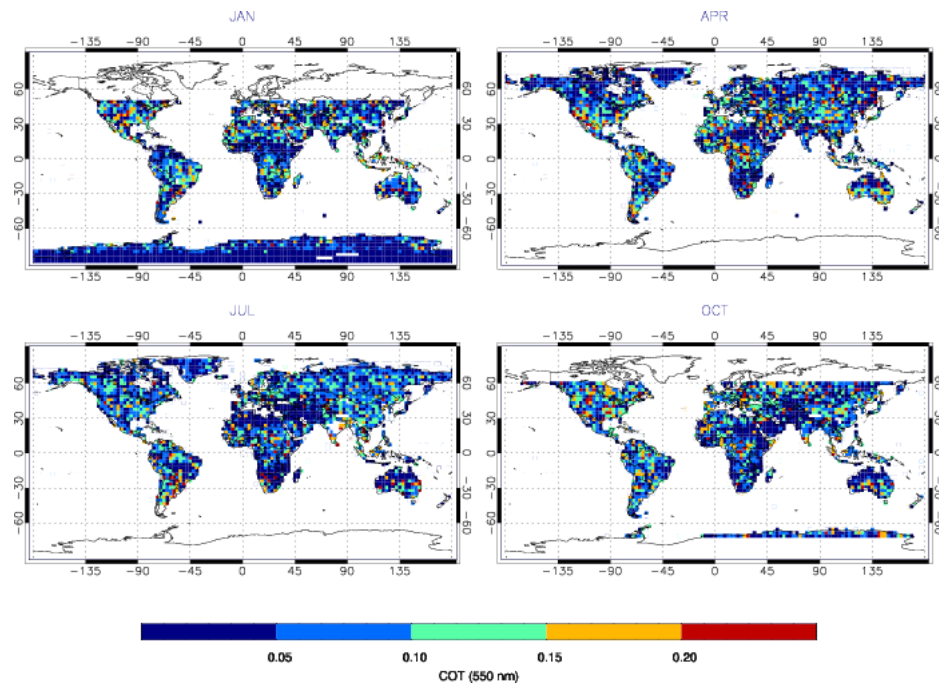
Figure 32: Global distribution of Cirrus Optical Thickness (COT) as used in the ensemble calculations.
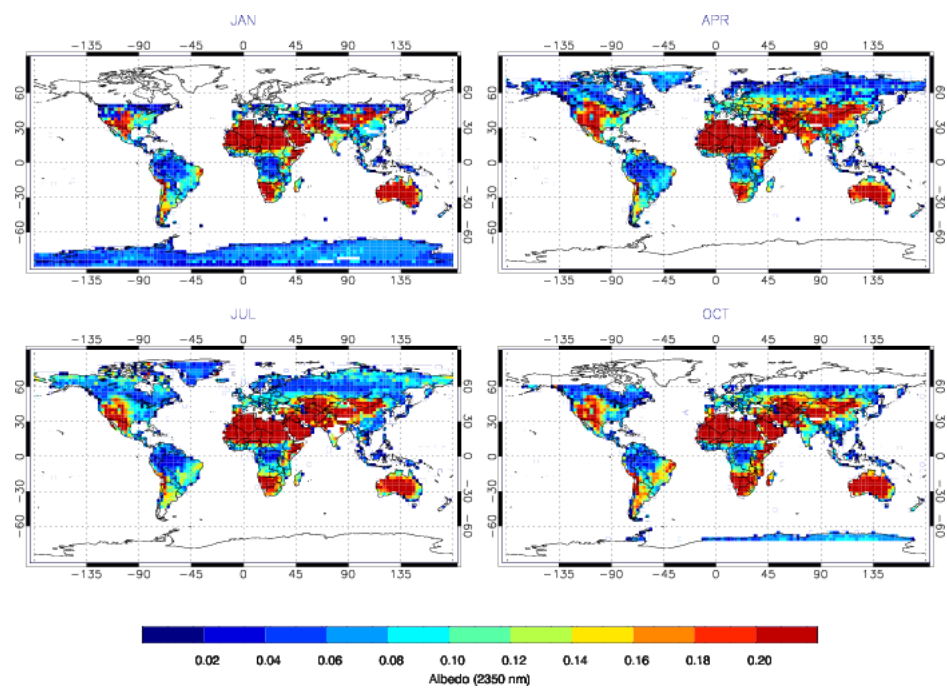
Figure 33: Surface albedo maps in the SWIR range for the synthetic ensemble.